University of Crete
School of Sciences
Department of Physics

Laser development of novel materials and diagnostics for Organic Photovoltaic Applications

PhD Thesis of

Maria I. Sygletou

Heraklion, Crete
July 2016

Table of Contents

The present dissertation has been written under the direction of **Prof. Constantinos Fotakis and Dr. Emmanuel Stratakis** and has been approved by:

1. Constantinos Fotakis, Professor, Physics Department, University of Crete

2. Panagiotis Tzanetakis, Emeritus Professor, Physics Department, University of Crete

3. Georgios Kioseoglou, Associate Professor, Materials Science and Technology Department, University of Crete

4. Georgios Kyriakidis, Professor, Physics Department, University of Crete

5. Dimitrios Papazoglou, Assistant Professor, Materials Science and Technology Department, University of Crete

6. Panagiotis Loukakos, Principal Researcher, IESL/FORTH

7. Emmanuel Kymakis, Associate Professor, Electrical engineering Department, T.E.I. of Crete

Abbreviations and Symbols

AM	Air Mass
BHJ	Bulk heterojunction
HOMO	Highest occupied molecular orbital
ITO	Indium tin oxide
J_{sc}	short circuit current density
LSPR	Localize plasmon resonance
LSPs	Localize surface plasmons
LUMO	Lowest unoccupied molecular orbital
OPVs	Organic Photovoltaics
P3HT	Poly(3-hexylthiophene-2,5-diyl)
PCDTBT	Poly[N-9-hepta-decanyl-2,7-carbazolealt-5,5-(4,7-di-2-thienyl-2,1,3-benzothiadiazole)]
$PC_{71}BM$	Phenyl-C71-butyric acid methyl ester
PCBM	Phenyl-C61-butyric acid methyl ester
PEDOT:PSS	Poly(3,4-ethylenedioxythiophene) : poly(styrenesulfonate)
TEM	Transmission electron microscopy
V_{oc}	Open circuit voltage
FF	Fill Factor
DCB	Dichlorobenzene
EQE	External Quantum Efficiency
PCE	Power Conversion Efficiency
HTL	Hole transporting layer
ETL	Electron transporting layer

Acknowledgements-Ευχαριστίες

Η διεκπεραίωση της παρούσας διατριβής δε θα ήταν εφικτή χωρίς τη συμβολή κάποιων ανθρώπων τους οποίους θα ήθελα να ευχαριστήσω τόσο για την καθοδήγηση όσο και για την υλική και ηθική υποστήριξη που μου παρείχαν.

Αρχικά θα ήθελα να ευχαριστήσω τον υπεύθυνο καθηγητή της εργασίας αυτής, κ. Κωνσταντίνο Φωτάκη, ο οποίος από τα χρόνια που ήμουν προπτυχιακή φοιτήτρια ακόμη μου έδωσε την ευκαιρία να εργαστώ στα εργαστήρια του Ινστιτούτου Ηλεκτρονικής Δομής και Λέιζερ (ΙΗΔΛ), στο Ίδρυμα Τεχνολογίας και Έρευνας (ΙΤΕ).

Στη συνέχεια, θα ήθελα να ευχαριστήσω ιδιαιτέρως τον επιβλέποντα αυτής της εργασίας, Δρ. Εμμανουήλ Στρατάκη για την αμέριστη καθοδήγηση, υπομονή και συμπαράσταση καθόλη τη διάρκεια της διατριβής. Νιώθω πραγματικά τυχερή και ευγνώμων για την άψογη συνεργασία μας.

Να ευχαριστήσω επίσης τους καθηγητές Παναγιώτη Τζανετάκη, Γεώργιο Κυριακίδη, Γεώργιο Κιοσέογλου, Δημήτρη Παπάζογλου και Εμμανουήλ Κυμάκη καθώς και τον ερευνητή Δρ. Παναγιώτη Λουκάκο που δέχτηκαν να είναι μέλη της εξεταστικής μου επιτροπής.

Θα ήθελα επίσης να ευχαριστήσω τον καθηγητή Κωνσταντίνο Πετρίδη για την πολύ καλή συνεργασία στην διεξαγωγή μέρους των πειραμάτων της εργασίας αυτής καθώς και τα μέλη της ομάδας Nanomaterials & Organic Electronics (NANO) του ΤΕΙ Κρήτης για την πολύτιμη βοήθεια στην προετοιμασία των φωτοβολταικών κυψελίδων.

Επιπλέον, θα ήθελα να ευχαριστήσω θερμά τα μέλη της ομάδας Ultrafast Laser Micro- and Nano- processing (ULMNP) του ΙΗΔΛ και ιδιαιτέρως την Κυριακή Σάββα για την άψογη συνεργασία, τις συμβουλές και τη στήριξη σε όλη τη διάρκεια της διδακτορικής διατριβής. Όπως επίσης θα ήθελα να ευχαριστήσω και τον κ. Λάμπρο Παπουτσάκη για τη βοήθεια του στη μελέτη των δειγμάτων με χρήση του Ηλεκτρονικού Μικροσκοπίου Διέλευσης.

Να ευχαριστήσω ακόμα τα άτομα με τα οποία μοιραστήκαμε το ίδιο γραφείο στο ΙΤΕ και μαζί τις αγωνίες, τις ευχάριστες και τις λιγότερο ευχάριστες στιγμές.

Τέλος, θα ήθελα να πω ένα μεγάλο ευχαριστώ στην οικογένεια και τους φίλους μου και ιδιαιτέρως στη μητέρα μου, οι οποίοι όποτε τους χρειάζομαι είναι πάντα δίπλα μου και με στηρίζουν με υπομονή και κατανόηση.

…dedicated to the memory of my father,

Ioannis Sygletos…

Abstract

Over the past decade, the need for low-cost and solution-processed materials, ideal for photovoltaic applications, has experienced particular attention in global scientific research. Organic semiconducting materials exhibit large potential for photovoltaic energy conversion. The major attention for organic photovoltaics (OPVs) originates from the fact that organic compounds are of much lower cost than silicon or any of the PV materials available to date, as well as that can be fabricated using low temperature solution processed techniques. In order to become more competitive, organic photovoltaic technologies must overcome two main problems: low efficiency and short lifetime. Further research effort towards increasing PCE as well as improving device lifetime is required. Working in this direction, we studied the effect of the incorporation of surfactant-free metallic nanoparticles into the active layer of OPV cells, on the efficiency and stability of the device. Such systems have demonstrated to be a very promising strategy to enhance the OPV performances[1,2], due to localized surface plasmon resonance (LSPR)[3,4,5] or multiple LSPR effects[6], light scattering[7] or multiple light scattering effects[8], the synergy of those[9] , the plasmonic effects of metal NPs clusters[10] or the utilization of multiple metal NPs[11], as well as the BHJ blend structure improvement[12]. In this work, the metallic nanoparticles were laser-synthesized with the method of laser ablation of solid in liquid medium.

Moreover, laser techniques were developed for the fabrication of hybrid 2D materials with metallic nanoparticles in solution in order to exploit both the contribution of NPs in the light absorption enhancement and the band gap tunability of the 2D materials in order to achieve higher exciton dissociation and charge collection for their potential application in ternary devices. The NS-NPs assemblies were formed under ambient conditions, via a facile, rapid and solution compatible laser assisted process in the presence of a metallic precursor. The resulting hybrid materials have been incorporated into the photoactive layer as the third component in a ternary OPV device along with polymer/fullerene composites.

The concept of photochemical synthesis in solution was also used for the fabrication of graphene based materials for their application as electron acceptors in OPV devices. Graphene-based nanostructured materials appear to be attractive alternatives in a

range of new energy devices, including organic photovoltaic cells, lithium batteries, fuel cells and supercapacitors. The resulting graphene-based materials have been incorporated into the photoactive layer of OPV devices and have been applied as electron-acceptor materials, replacing the most used fullerene derivative $PC_{71}BM$. Finally, the structures of the laser synthesized materials used, as well as the optimization of the fabricated OPVs have been evaluated by utilizing various spectroscopy and microscopy analyses, alongside with complementary photovoltaic measurements.

Περίληψη

Τα τελευταία χρόνια, η ανάγκη για χαμηλού κόστους υλικά με δυνατότητα επεξεργασίας σε διάλυμα, ιδανικά για φωτοβολταϊκές εφαρμογές, έχει γνωρίσει ιδιαίτερη προσοχή στην παγκόσμια επιστημονική έρευνα. Τα οργανικά ημιαγώγιμα υλικά παρουσιάζουν φωτοβολταικές δυνατότητες. Οι οργανικές ενώσεις έχουν πολύ χαμηλότερο κόστος παραγωγής από ότι το πυρίτιο ή οποιοδήποτε από τα διαθέσιμα μέχρι σήμερα φωτοβολταικά υλικά, ενώ οργανικές φωτοβολταικές διατάξεις μπορούν να κατασκευαστούν χρησιμοποιώντας τεχνικές επεξεργασίας διαλυμάτων σε χαμηλές θερμοκρασίες. Για να γίνουν πιο ανταγωνιστικές οι τεχνολογίες οργανικών φωτοβολταϊκών πρέπει να ξεπεραστούν δύο κύρια προβλήματα : η χαμηλή απόδοση και η μικρή διάρκεια ζωής. Απαιτείται περαιτέρω ερευνητική προσπάθεια για την αύξηση της απόδοσης μετατροπής ισχύος, καθώς και τη βελτίωση της διάρκειας ζωής της συσκευής. Δουλεύοντας σε αυτή την κατεύθυνση, μελετήθηκε η επίδραση της ενσωμάτωσης μεταλλικών νανοσωματιδίων στο ενεργό στρώμα των οργανικών φωτοβολταικών κυψελίδων, στην αποτελεσματικότητα και την σταθερότητα της συσκευής. Τέτοια συστήματα έχουν αποδειχθεί ότι είναι μια πολλά υποσχόμενη στρατηγική για την ενίσχυση της λειτουργίας, λόγω τοπικού συντονισμού επιφανειακών πλασμονίων (LSPR) ή σκέδασης φωτός ή συνέργεια των δύο. Στην εργασία αυτή, πραγματοποιήθηκε σύνθεση μεταλλικών νανοσωματιδίων μέσω φωτοαποδόμησης με λέιζερ στερεού στόχου σε υγρό μέσο. Επιπλέον, τεχνικές λέιζερ αναπτύχθηκαν για την κατασκευή υβριδικών διδιάστατων υλικών με μεταλλικά νανοσωματίδια σε διάλυμα προκειμένου να αξιοποιηθεί τόσο η συμβολή των νανοσωματιδίων στην ενίσχυση απορρόφησης του φωτός όσο και η ύπαρξη ενεργειακού χάσματος των υλικών, προκειμένου να επιτευχθεί ενίσχυση του διαχωρισμού εξιτονίων και συλλογή φορτίου για πιθανή εφαρμογή τους στην τριμερή συσκευές. Τα συστήματα διδιάστατων φύλλων με μεταλλικά νανοσωματίδια σχηματίστηκαν υπό συνθήκες περιβάλλοντος, μέσω μιας εύκολης και ταχείας διαδικασίας λέιζερ σε διάλυμα, υποβοηθούμενης υπό την παρουσία ενός μεταλλικού προδρόμου. Τα προκύπτοντα υβριδικά υλικά έχουν ενσωματωθεί στο ενεργό στρώμα ως το τρίτο συστατικό σε μία τριαδική οργανική φωτοβολταική συσκευή με ένα συζυγές πολυμερές και ένα φουλερένιο.

Η έννοια της φωτοχημικής σύνθεσης σε διάλυμα χρησιμοποιήθηκε επίσης για την κατασκευή νέων υλικών με βάση το γραφένιο για την εφαρμογή τους ως αποδέκτες ηλεκτρονίων σε οργανικές φωτοβολταικές συσκευές. Τα νανοδομημένα υλικά με βάση το γραφένιο φαίνεται να είναι ελκυστικές εναλλακτικές λύσεις σε μια σειρά νέων ενεργειακών συσκευών, συμπεριλαμβανομένων των οργανικών φωτοβολταϊκών κυψελίδων, σε μπαταρίες λιθίου, κυψέλες καυσίμου και υπερπυκνωτές. Τα προκύπτοντα υλικά με βάση το γραφένιο έχουν ενσωματωθεί στο ενεργό στρώμα των συσκευών OPV και έχουν εφαρμοσθεί σαν αποδέκτες ηλεκτρονίων, αντικαθιστώντας το πλέον χρησιμοποιούμενο παράγωγο φουλερενίου $PC_{71}BM$. Τέλος, ο χαρακτηρισμός των υλικών που προέκυψαν μετά την κατεργασία με laser καθώς και η βελτιστοποίηση των φωτοβολταικών διατάξεων που κατασκευάστηκαν, έχουν αξιολογηθεί με τεχνικές φασματοσκοπίας και μικροσκοπίας παράλληλα με φωτοβολταικές μετρήσεις.

Thesis Layout

The main goal of this thesis is the application of laser assisted techniques for the development of novel materials and spectroscopic techniques for their application in Organic Photovoltaic (OPV) devices. In Chapter 1, the motivation for this work and the approaches for the enhancement of both, efficiency and stability of Organic Solar Cells (OSCs), are presented. In Chapter 2, the bulk heterojunction concept, as well as the basic principles of device operation is reported. Moreover, the main drawback of photo-oxidation of polymers that are used in BHJ devices as well as a new approach for more efficient light-harvesting are also presented. In Chapter 3, the two dimensional materials used in this study and their properties are mentioned. Chapter 4 is a synopsis of the background of Laser based techniques for OPV materials synthesis, modification and diagnostics that were applied in the present study. In Chapter 5, enhancement of the stability of bulk heterojunction (BHJ) organic photovoltaic (OPV) devices is reported by the addition of laser synthesized surfactant-free Aluminum (Al) nanoparticles (NPs) into the photoactive layer. The universality of the effect is demonstrated for two different BHJ systems, namely the well-studied Poly(3-hexylthiophene-2,5-diyl) (P3HT):(Phenyl-C61-butyric acid methyl ester (PCBM)) as well as the high efficient poly[N-9'-heptadecanyl-2,7-carbazole-alt-5,5-(4',7'-di-2-thienyl-2',1',3' benzothiadiazole)](PCDTBT):[6,6]-phenyl-C71-butyric-acid-methyl-ester ($PC_{71}BM$). In Chapter 6, a novel top-down and universal optical technique for the effective decoration of two-dimensional (2D) nanosheets (NS), of graphene oxide (GO), boron nitride (BN) and tungsten disulfide (WS_2), with noble metallic nanoparticles (NPs) in solution, is reported. The laser induced anchoring of Au NPs onto NS basal plane and edges resulted in enhanced light harvesting that is potentially useful for energy conversion and storage applications. To demonstrate the potential of the approach for practical applications, the incorporation of WS_2-Au NPs assemblies into the photoactive layer of ternary bulk heterojunction (BHJ) organic photovoltaic (OPV) cells is realized. The power conversion efficiency (PCE) of the binary device consisting of a poly[N-9'-heptadecanyl-2,7-carbazole-alt-5,5-(4',7'-di-2-thienyl-2',1',3'-benzothiadiazole)](PCDTBT):[6,6]-phenyl-C71-butyric-acid-methyl-ester ($PC_{71}BM$) blend as the donor-acceptor pair was 5.6%, while after the employment of WS_2-Au NPs the efficiency enhancement of the ternary

device was approximately 13% reaching a total PCE of 6.3%. In Chapter 7, laser assisted techniques were further used for the photochemical synthesiss of tunable bandgap graphene-based derivatives from graphene oxide (GO) through controlled laser irradiation in liquid phase. The method is facile and fast, yielding these materials within 2 hours and with excellent long-term stability. It makes use of photogenerated solvated electrons that give rise to GO reduction, accompanied by preferential attachment of the desired functional unit, intentionally dispersed into the precursor GO solution. As a proof of concept, Graphene Oxide-Ethylene-DiNitro-Benzoyl (LGO-EDNB) was photochemically synthesized and utilized as the electron acceptor material in organic bulk heterojunction solar cells (OSCs) with the poly[*N*-9The method is facile and fast, yielding these materials within 2 hours and with excellent long-term stability. The utilization of LGO-EDNB with a bandgap of 1.7 eV, and a resultant lowest unoccupied molecular orbital (LUMO) level of 4.1 eV, leads to maximum open-circuit voltage of 1.17 V and to power conversion efficiency (PCE) of 2.41%, which is the highest PCE for graphene-based electron acceptors to date.

Chapter 1: Introduction

Organic semiconducting materials exhibit large potential for photovoltaic energy conversion. The major attention for organic photovoltaics (OPVs) originates from the fact that organic compounds are of much lower cost than silicon or any of the PV materials available to date, as well as that can be fabricated using low temperature solution processed techniques. Recently, notable efficiency improvements were obtained: for instance, using bulk heterojunction (BHJ) OPV devices, power conversion efficiencies (PCE) exceeding 9% were reported[13] for single junction and up to 11% for multijunction tandem solar cells[14]. Nonetheless, further reasearch effort towards increasing PCE as well as improving device lifetime is required in order to fulfil all requirements, efficiency, lifetime and cost for future commercialization.

On the other hand, as OPV efficiencies steadily improve, the investigation of performance degradation consequent to solar irradiation and outdoor operation becomes increasingly important and still remains a major issue to address for OPVs commercialization[15]. Indeed, it has been shown that, the light-induced instability of BHJ OPV cells is directed by complex photodegradation pathways, related to the structural, morphological and interfacial properties of virtually any layer and interface of OPV devices[16,17,18,19]. In this context, complementary physicochemical characterization techniques are required for a complete understanding of the effect of each of the parameters involved and realization of OPV devices exhibiting improved stability.

In this work we report on new approaches, based on laser techniques to enhance both, power conversion efficiency (PCE) and the durability of organic photovoltaic (OPV) devices. Firstly, the effect on the durability of the organic solar cells, by the incorporation of laser synthesized metallic nanoparticles in the BHJ system of the OPV devices, was studied. It has already been reported that the incorporation of metallic nanoparticles inside the different layers of organic photovoltaic devices can enhance their efficiency[1,4,5,20,21]. By performing electrical measurements, enhancement of the lifetime of the devices is also observed by the presence of NPs. In this work two

different BHJ systems were studied, namely P3HT:$PC_{60}BM$ and PCDTBT:$PC_{71}BM$, doped with metallic NPs, while the underlying degradation mechanisms were explored by optical spectroscopy techniques complemented with device degradation electrical measurements.

Subsequently, in an attempt to further exploit the property of the metallic nanoparticles to enhance the efficiency of OPVs, we proceed in laser assisted fabrication of hybrid two-dimensional (2D) nanosheets (NS), of graphene oxide (GO), boron nitride (BN) and tungsten disulfide (WS_2), with noble metallic nanoparticles (NPs), in solution. Transition metal dichalcogenides (TMDCs) with the common structural form MeX_2 (Me = Mo, W, Ti, etc and X = S, Se, Te), and boron nitride (BN) NS exhibit a laminar structure similar to that of graphene and have drawn the attention of research community[22],[23],[24]. One of the most attractive features of TMDCs structured compounds is their transition from indirect band gap semiconductors in their bulk nature, to direct band gap semiconductors when isolated as a monolayer. The tungsten disulfide (WS_2) and molybdenum disulfide (MoS_2) are semiconductors with band gaps ranging from the visible to the near-infrared[25]. While, hexagonal BN is an excellent dielectric[23]. In this context, the possibility of incorporating solution processable 2D materials combined with metal NPs to form NS-NPs assemblies inside the photoactive layer of OPVs can provide a dual enhancement effect. Firstly, the NPs will enhance the light absorption via either plasmonic or scattering effects, and secondly the bandgap tunability of 2D NS could give rise to enhanced exciton dissociation and charge collection through the formation of a ternary OPV configuration[26].

In order to further study the laser synthesis of 2D derivatives in solution, graphene based materials were photochemically fabricated for application as one of the layers of an OPV device. Specifically, the potential of replacement the fullerene materials that are commonly used as electron acceptors in OPVs ($PC_{60}BM$, $PC_{71}BM$) with laser synthesized graphene derivatives, was investigated. The production method of fullerenes is highly expensive and their weak absorption in the visible range induces the need for new low cost production methods of novel materials as electron acceptors. Moreover, graphene based materials exhibit an enormous thermal conductivity[27], thus the incorporation of such materials in the photoactive layer of OSCs could mitigate heat-related degradation

effects due to prolonged solar illumination. More importantly, due to their extremely high aspect ratio, graphene sheets are perfectly fitted to promote migration of electrons along their 2d plane[28]. In this respect, graphene-based materials are anticipated to be utilized for the effective exciton separation and charge transport when blended with conjugated polymers, because of their large surface area for donor/acceptor interfaces and continuous pathway for the electron transfer, as in the case of carbon nanotubes[29,30].

Using an one step laser method, a bandgap tunable electron acceptor system, named as Laser Graphene Oxide-Ethylene-DiNitro-Benzoyl (LGO-EDNB), was successfully synthesized. Laser based synthesis has been particularly attractive since it enables fast processing time, it is scalable and provides materials of high-purity. Besides this, laser parameters can be controlled with an amazingly high degree of precision, therefore this technology could be conveniently integrated into device fabrication process. Of great interest are the laser induced reduction[31,32,33], exfoliation[34], heteroatom doping[35,36], nanocomposite formation[37], patterning[38,39] and in-situ treatment of electronic devices[40].

Chapter 2: Bulk heterojunction solar cells

Polymer-fullerene bulk heterojunction solar cells have shown promise in a field largely dominated by inorganic (e.g. silicon) solar cells. Specifically, fullerene derivatives act as electron acceptors for donor materials like P3HT (poly-3-hexyl thiophene-2,5-diyl), creating a polymer-fullerene based photovoltaic cell. In the first organic solar cell, the active layer was a bilayer of donor and acceptor sandwiched between two electrodes[41] and efficiency lower than 1% was achieved. Following, the bulk heterojunction concept was introduced with enhanced efficiency of about 3%[42]. Due to the development of new low band gap polymers, the power conversion efficiency of such devices has reached values up to 11%[14].

In the bilayer solar cell, the active layer consists of a single donor-acceptor interface available for exciton dissociation. In a bulk-heterojunction structure, the active layer consists of donor and acceptor materials that are mixed together to form a bicontinuous interpenetrating network with large interfacial areas for efficient exciton dissociation. The operation mechanism of BHJ PSCs can be described in four steps: (1) light absorption and generation of excitons; (2) exciton diffusion to the donor– acceptor interface; (3) exciton dissociation at the interface, first creating charge transfer (CT) states or so-called polaron pairs; then CT states fully dissociate into free charge carriers; (4) charge transport and collection. For the optimization of each of these processes, great efforts are devoted to developing materials, new device architectures, and methods.

2.1. Conjugated Polymers

Heeger, MacDiarmid and Shirakawa demonstrated in 1977 that chemical doping of conjugated polymers results in an increase of the latter's electronic conductivity by several orders of magnitude. Conjugated polymers are organic macromolecules which consist at least of one backbone chain of alternating double and single bonds. This alternation is responsible for the semiconducting nature of conjugated polymers. In conjugated polymers carbon atoms are sp^2 hybridized. In the sp^2 hybridization the 2s

orbital is hybridized with two 2p orbitals ($2p_x$, $2p_y$) giving rise to three sp^2 orbitals and one 2p orbital ($2p_z$). Carbon can form two types of bonds: the σ-bond is formed by the overlap of the hybridized orbitals of the adjacent atoms which are oriented along the chain. So there are three coplanar sp^2hybridized orbitals which are at an angle of 120° with each other (Figure 2.1).

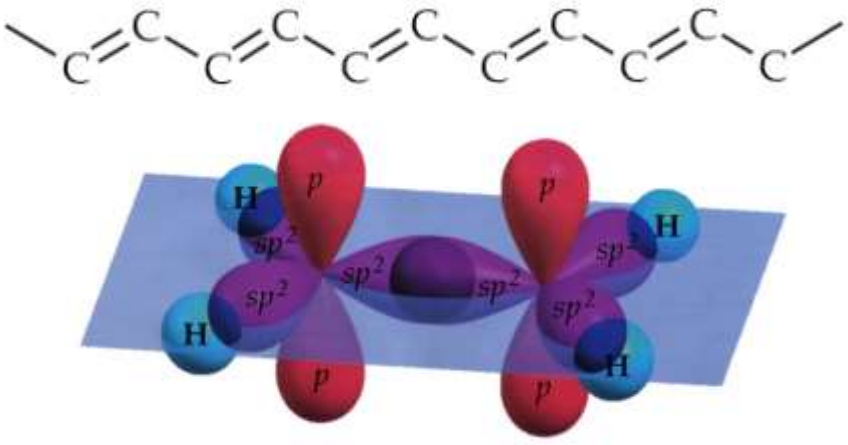

Figure 2.1: Chain of the carbon atoms with the alternating single and double bonds (top). Example of a conjugated molecule (ethylene) (bottom).

Therefore, three σ bonds are formed, two with neighboring carbon atoms and one with a hydrogen atom. The remaining out of plane p_z orbitals, each occupied by one electron, overlap with neighboring p_z orbitals to form bonds which are perpendicular to the chain shown. These electrons are delocalized along the entire polymer backbone, which is the reason for the conducting properties of conjugated polymers.

The overlap of p_z orbitals forms two molecular orbitals, a bonding π-orbital which is the highest occupied molecular orbital (HOMO) and an antibonding π*- orbital which is the lowest unoccupied orbital (LUMO). The π-orbital and π*- orbital are equivalent to the valence band and conduction band of an inorganic semiconductor, respectively. The difference between the HOMO and LUMO is called the band gap of the organic material. When a photon with energy equal to or higher than the energy band gap (Eg) interacts with a conjugated polymer, the electrons can be transferred from π (highest occupied molecular orbital - HOMO) to a $\pi*$ (lowest unoccupied molecular orbital -

LUMO) excited state, this is known as an excitation. This excitation creates a Coulomb bound hole-electron pair, called exciton. The exciton binding energy can be calculated from Coulomb's law,

$$E_b = \frac{e^2}{4\pi\varepsilon_0\varepsilon R}$$

where *e* is the charge of the electron, ε_0 is the permittivity of vacuum, ε is the dielectric constant of the medium, and R is the electron-hole separation distance. The force keeping the electron-hole pair together is inversely proportional to the dielectric constant of the conjugated polymer (ε = 3-4) and this is why it is more difficult to dissociate an exciton in organic than inorganic semiconductors ($\varepsilon_{silicon}$=11).

An exciton can be considered as a Freknel exciton, if the pair is confined to one molecular unit or as a Mott-Wannier exciton if it extends over many molecular units. The intermediate case, where the exciton extends over a few adjacent molecular units, can be called the charge-transfer exciton. Also, the terms "inter-chain" and "intra-chain" exciton are used for polymeric semiconductors to indicate that the constituent charges are located on different or on the same polymer chains respectively. The exciton binding energy of conjugated polymers depends strongly on the structure. For highly crystalline polydiacetylene, the binding energy has been determined to be 0.5 eV, while for amorphous polymers like the polythiophene and PPV, is about 0.4 eV[43,44].

The successful exciton diffusion and dissociation to the donor – acceptor interface will lead to charge transport and current collection. The transport process is mainly by hopping along conjugated chain and inters molecular charge transport between adjacent polymer chains or molecules.

The combination of the optoelectronic properties of inorganic semiconductors and the technological advantages of the polymers make them very attractive to the scientific community. Furthermore, they are characterized by high absorption coefficients, making it possible to use a layer thickness at the nanometer scale. Conjugated polymers are nowadays used in various organic electronic applications, like transistors, photodiodes, light emitting diodes, solar cells, etc.

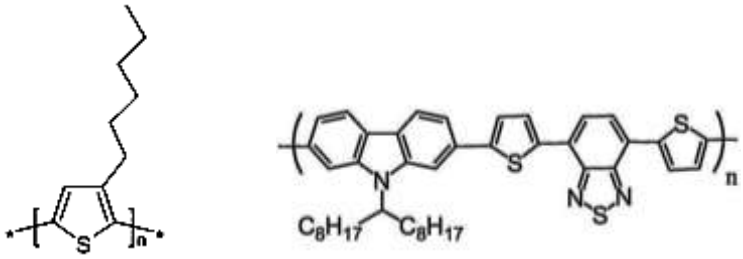

Figure 2.2: Chemical structure of P3HT (left) and PCDTBT (right) conjugated polymers

2.2. Basic principles of device operation

The absorption of photons by the polymer produces electrostatically coupled electron hole pairs called excitons (figure 2.3). They are characterized by very small lifetime (few picoseconds) and that limits their mobility inside the polymer. The exciton moves within the chain causing chain deformation in order to reduce the extra unstable energy, which is altogether called polaron. However, inter-molecular transition of excitons also happens which is termed as hopping process. All of the above limit the exciton diffusion length to a range of 10 nm. The excitons must be dissociated within this range, otherwise recombination of electron-hole pairs occur resulting in charge losses. After exciton generation, the coupled electron-hole pair needs to split into free charges. The dissociation of excitons occurs at the donor acceptor interfaces or junctions. The donor and acceptor materials must be designed such that there is a difference between LUMO levels of the materials, which triggers exciton dissociation. For efficient dissociation, the difference in energy level of LUMO of donor and acceptor should be higher than the exciton binding energy. Typically the difference is around 200-300 meV. After singlet excitons split into separated electrons and holes, they travel through specific materials to get collected at the electrodes. The efficiency of charge transport is determined by the electrical conductivity and impedance of the organic materials.

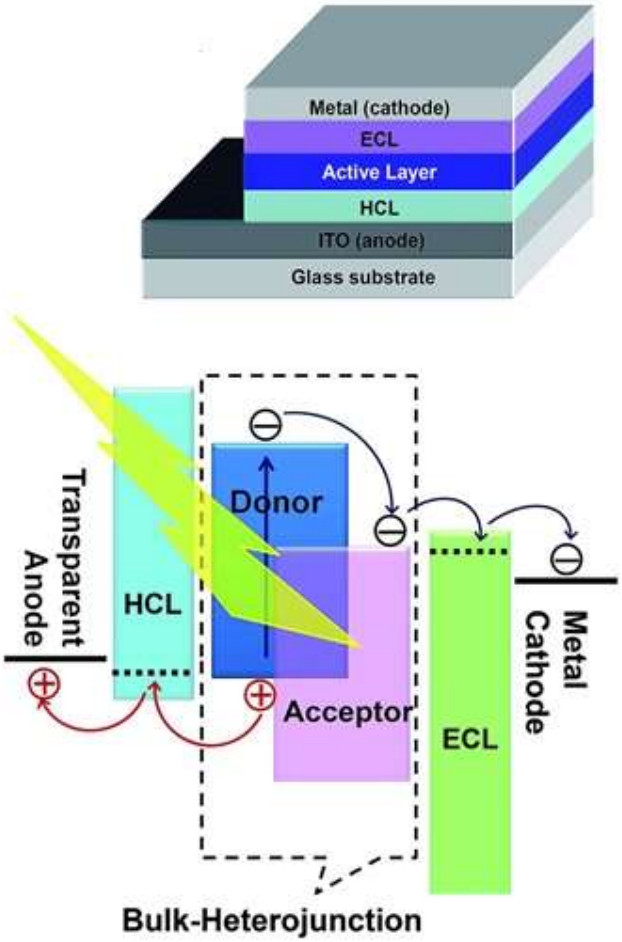

Figure 2.3: Bulk heterojunction architecture

Ternary cascade

Recently, an elegant alternative strategy was realized to extend the spectral sensitivity of wide bandgap polymers into the near IR region, the so-called organic ternary solar cell[45,46]. In a ternary organic solar cell, a third component is simply added to the host system consisting of a wide bandgap polymer blended with fullerene derivative, as it is illustrated in Figure 2.4. The ternary approach could improve the photon harvesting in thickness limited photoactive layers, resulting in higher short circuit current densities (Jsc) and therefore higher PCEs in a simple single-junction. As such, the ternary solar cell concept avoids the demanding challenges of multi-junction solar cells processing for spectrally broad light harvesting. However, it does so at a lower thermodynamic

potential as a tandem cell. The charge transfer and transport in the ternary blend is more than a simple superposition of the charge transfer and transport properties of the individual phases. It is governed by various mechanisms, depending on the third component content, electronic energy levels and bandgap of the three components, location of the third component in the binary photoactive layer as well as final microstructure of the film. The main goal of the addition of the third component in the active layer is the enhancement of light absorption and exciton dissociation.

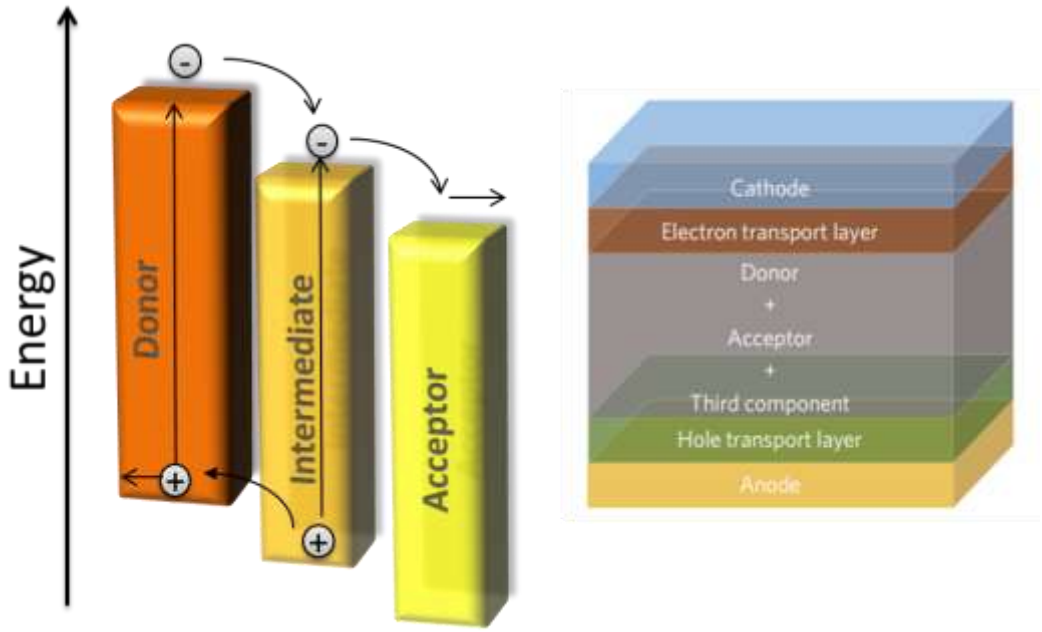

Figure 2.4: Schematic of the energy levels(left) in the photoactive layer in a ternary organic solar cell[46] (right).

2.3. Solar cell performance

For the examination of solar cell efficiency, electrical measurements (IV curve) are performed. The current-voltage characteristic can be described by the equation 1:

$$I = I_s(e^{\frac{q(V-IR_s)}{nkT}} - 1) + \frac{V - IR_s}{R_p} - I_{ph}$$

Equation 1

where I_s is the dark or reverse saturation current, n the ideality factor of the diode, R_s the series resistance, R_p the shunt resistance, and I_{ph} the photocurrent. The primary parameter extracted from the IV curve is the power conversion efficiency (PCE), which describes the general efficiency of the solar cell. PCE is the ratio of generated electricity to incoming light energy. The formula for the PCE is

$$\eta = \frac{J_{sc} V_{oc} FF}{P_{in}}$$

Equation 2

where J_{sc} is the short circuit current density, V_{oc} the open circuit voltage, and FF the fill factor. The open circuit voltage can easily be derived from equation 3,

$$V_{oc} = \frac{E_{gap}}{q} - \frac{kT}{q}\left(\frac{(1-P)\gamma N_c^{\,2}}{PG}\right)$$

Equation 3

where E_{gap} is the difference between HOMO and LUMO levels, P is dissociation probability, G is generation rate of bound electron-hole pairs, γ is recombination constant and N_c is the effective density of states.

The fill factor is the ratio of the actual maximum obtainable power to the product of the open circuit voltage and short circuit current (equation 4).

$$FF = \frac{P_{\max}}{P_{out}} = \frac{J_{\max} V_{\max}}{J_{SC} V_{OC}}$$

Equation 4

The term quantum efficiency (QE) in solar cells refers to incident photon to converted electron (IPCE) ratio. A solar cell's quantum efficiency value indicates the amount of current that the cell will produce when exposed to sunlight. There are two types of

quantum efficiency: External Quantum Efficiency (EQE) and Internal Quantum Efficiency (IQE). EQE is the ratio of the number of charge carriers collected by the solar cell to the number of incident photons. IQE is the ratio of the number of charge carriers collected by the solar cell to the number of absorbed photons by the cell. To measure the IQE, one first measures the EQE of the solar device, then measures its transmission and reflection, and combines these data to infer the IQE.

Examples of the current density-voltage (JV) characteristic of a sample polymer:fullerene solar cell and the incident photon to converted electron (IPCE) ratio graph are reported in figure 2.5.

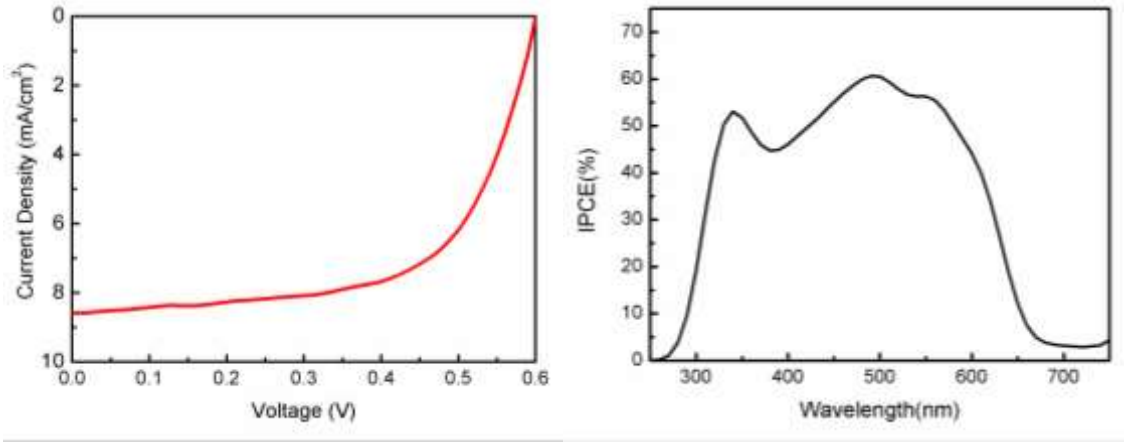

Figure 2.5: J-V characteristic (left) and IPCE graph (right) of a BHJ device (P3HT:PCBM).

2.4. Light Harvesting in organic solar cells-plasmonic and scattering effects

Various methods for the enhancement of light harvesting in organic solar cells have been studied including incorporation of metallic nanoparticles in the active layer. In OSCs, enhancement of the absorbance of a polymer film of a specific limited thickness still remains a challenge. A major hindrance toward the development of OPVs is the fundamental tradeoff between light absorption and collection of photo-generated excitons. Efficient charge transport in BHJ OPVs is achieved provided that continuous pathways for both charge carriers exist. Naturally, the presence of such pathways is less

likely for thicker active layers. In addition, carriers exhibit reduced exciton diffusion lengths in organic semiconductors due to limited hopping transport[47]. As a result, active layer thicknesses in optimized OPV devices are small, typically around 200 nm. Owing to such a low active layer thickness, the best devices that have been developed absorb poorly, despite displaying low charge–carrier recombination. Research in this area has indicated that the compromise between efficient light harvesting and efficient charge collection, determined by the organic layer thickness, can be resolved by 'trapping' incident light in the active layer. One promising plasmon enhanced light-trapping approach is the utilization of plasmonic metallic nanoparticles (NPs) either between interfaces, or inside the buffer or the active layers of OPV devices in order to promote absorption, thereby increasing the optical thickness of OPV materials for light harvesting[48,49]. Noble metallic NPs are known to exhibit a strong absorption band in the UV–Vis region, which lies within the optical absorption band of the conjugated polymers used in the active layer of OPVs. The physical origin of this enhanced absorption is the coherent oscillation of the free electrons, coined as a plasmon wave, which is excited by the incident electromagnetic field. When the electron cloud is displaced relative to the nuclei, a restoring force arises from Coulomb attraction between electrons and nuclei that results in an oscillation of the electron cloud relative to the nuclei framework. For NPs with dimensions well below the wavelength of light in the quasi-static limit, the scattering and absorption crosssections are given by eq.4

$$\sigma_{sc}\frac{1}{6\pi}\left(\frac{2\pi}{\lambda}\right)^4|a|^2, \sigma_{abs}=\frac{2\pi}{\lambda}lm|a|$$

Equation 4[50]

where a = 3V((ep/em) + 1)/((ep/em) + 2) is the polarizability of the particle. Here V is the particle volume, ep is the dielectric function of the particle and em is the dielectric function of the embedding medium. The scattering efficiency Qsc is given by Qsc = ssc/ (ssc + sabs)[50]. We can see that when the light frequency is such that ep=-2em the particle polarizability and the absorption cross section become maximal (resonance) and this condition is termed the localized surface plasmon resonance (LSPR, non-propagating excitations of conduction electrons within a metallic nanostructure). The

LSPR frequency depends on the size and shape of the NP, the NP material and the optical constants of the NP surrounding medium[51]. From the above equations, it is clear that NPs act as local field enhancers or light scattering centers or both, depending on their size[49,8]. Absorption dominates for small NPs with diameters in the range 5–20 nm. In this case NPs behave as subwavelength antennas, due to LSPR excitation (Figure 2.6b). The plasmonic nearfield is coupled to the photoactive layer, increasing its effective absorption cross-section and thus exciton dissociation. On the other hand, relatively larger diameter NPs behave as effective subwavelength scattering elements that couple and trap freely propagating plane waves of the incident light into the photoactive layer [16]. At LSPR, such NPs can have a scattering cross-section much larger than their geometric crosssection. In this case, enhanced absorption takes place by an increase of the optical path length inside the photoactive layer, caused by the light being reemitted in different directions within the device (Figure 2.6a). The incident light scatters in all different directions.

Light scattering is another method of light trapping. It has a direct dependence on particle size. From the strong dependence upon the radius of the particle, it seems like the scattering efficiency will increase with increasing particle size. This is indeed true for particles within a certain order of size. NPs dispersed into the photoactive layer of OPV devices can offer a major enhancement on its optical absorption, either via the formation of scattered waves at the large diameter NPs or due to excitation of LSPR modes at the smaller diameter NPs. As an example, Al NPs (10-70 nm) act as an effective ‘‘optical reflector’’ and multiple reflections will cause solar light to pass multiple times through the BHJ layer[2].

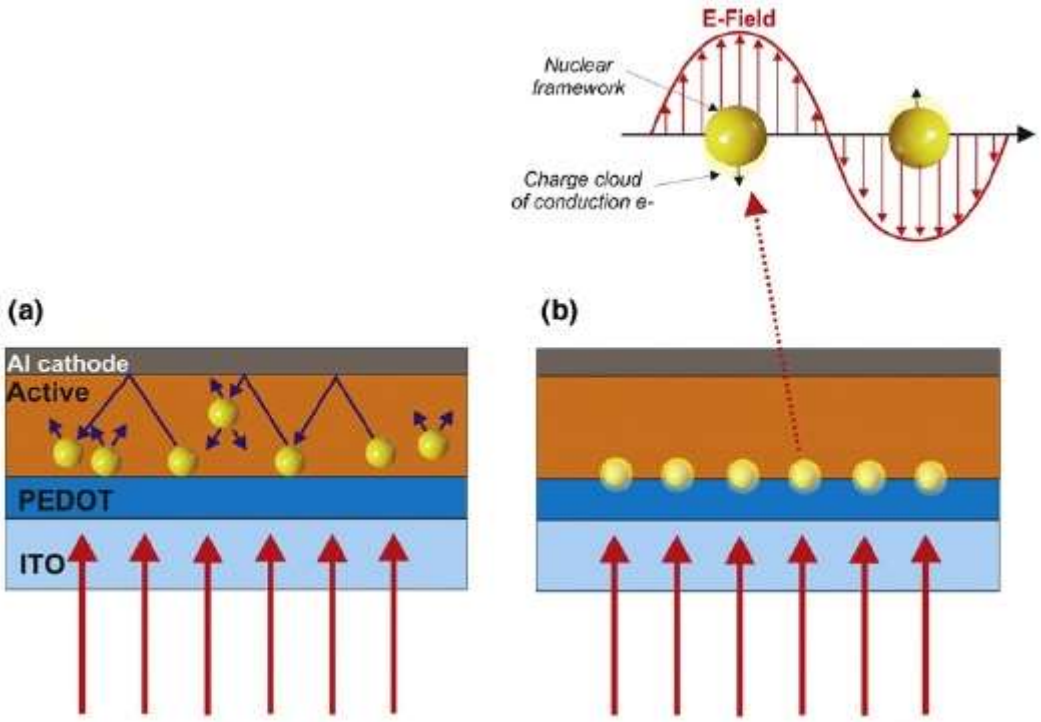

Figure 2.6: (Top) Schematic of the plasmon oscillation of a sphere, showing the displacement of the conduction electrons relative to the nuclei [14]. (Bottom) Different geometries for plasmonic light trapping in OPVs: (a) scattering from large diameter (>30 nm) metal NPs into high angles inside the photoactive layer, causing increased optical path lengths in the device; (b) LSPRs induced by small diameter (5–20 nm) metal particles[2].

2.5. Photo-oxidation of organic solar cells

As it already has been mentioned, a major drawback in OPV devices that needs to be overcome is their poor stability. Conjugated polymers are very sensitive when exposed to ambient air and light and degrade fast. The relative low efficiencies compared to silicon based devices is the main concern, but the issue of stability enhancement is just as important in order to make the OPVs competitive with other technologies. The interest of the scientific community has been focused on the study of the degradation mechanisms in polymer blends and devices in order to improve their stability. Understanding of degradation mechanisms in polymer:fullerene bulk-heterojunctions on the microscopic level aimed at improving their intrinsic stability is crucial for the breakthrough of organic photovoltaics. Different degradation pathways occur at every

layer and interface of OPV devices. The cause of degradation could be morphological changes, indium diffusion, photo oxidation, deterioration of the hole transport layer or the transparent electrode and chemical degradation of metal electrodes[15,16,19,52]. Nevertheless, the stability of OPV is mostly affected by the stability of their active components' ability to i) absorb light, ii) generate charge, and iii) transport free charge carriers[15]. If any of these processes degrades, the performance of the OPV is limited, regardless of the quality of the rest of the device layers. According to literature, the photochemical reaction that is responsible for the degradation of the active layer is related to the formation of singlet oxygen under participation of bound triplet excitons on the polymer chain[53].

Also, previous studies of oxygen-induced defect states in polymer devices show that the optical properties degrade by orders of magnitude upon exposure to air. (2.7 a,b[54]).

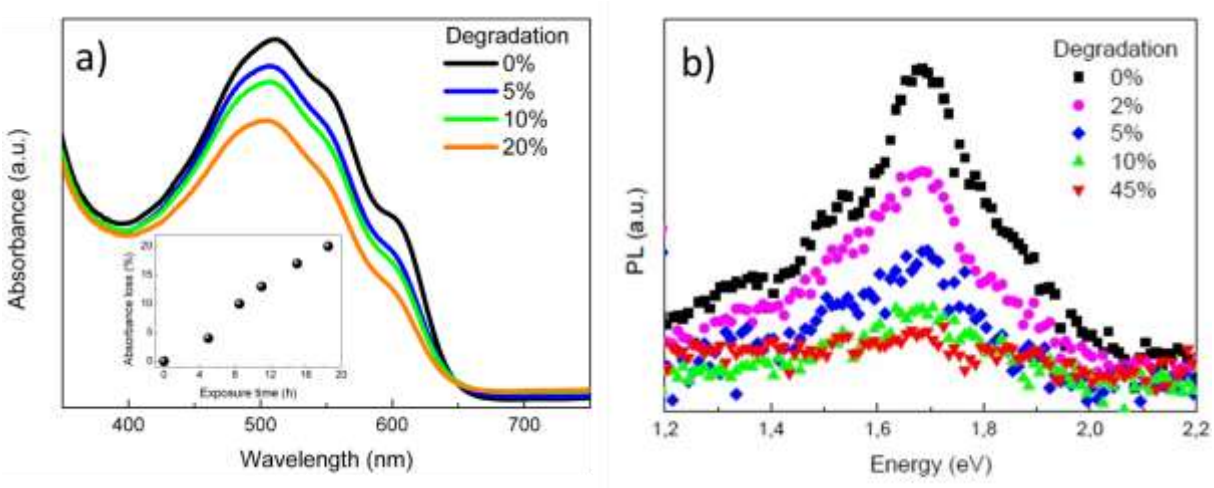

Figure 2.7: a) Absorbance spectra of the P3HT:PCBM blends degraded under light and synthetic air. The relative absorbance loss and the corresponding exposure time are reported in the inset and b) PL spectra of the P3HT:PCBM blends degraded under light in a synthetic air environment[54]

The effect of oxygen on the optical properties of the donor-polymer when the same devices are exposed to air in dark conditions is limited. (Figure 2.8). In this case, the observed degradation of the device is mainly attributed to the degradation of the hole transport layer because of the hydroscopic nature of both polymers of the HTL blend (PEDOT:PSS)[55].

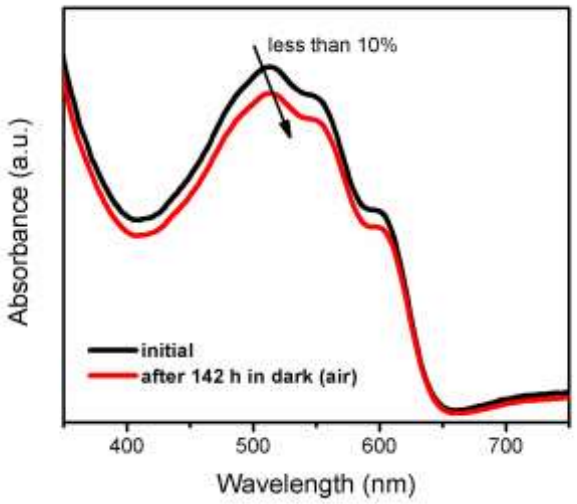

Figure 2.8: Absorbance spectra of P3HT:PCBM blends before and after exposure in air under dark conditions, for 142 hours

.

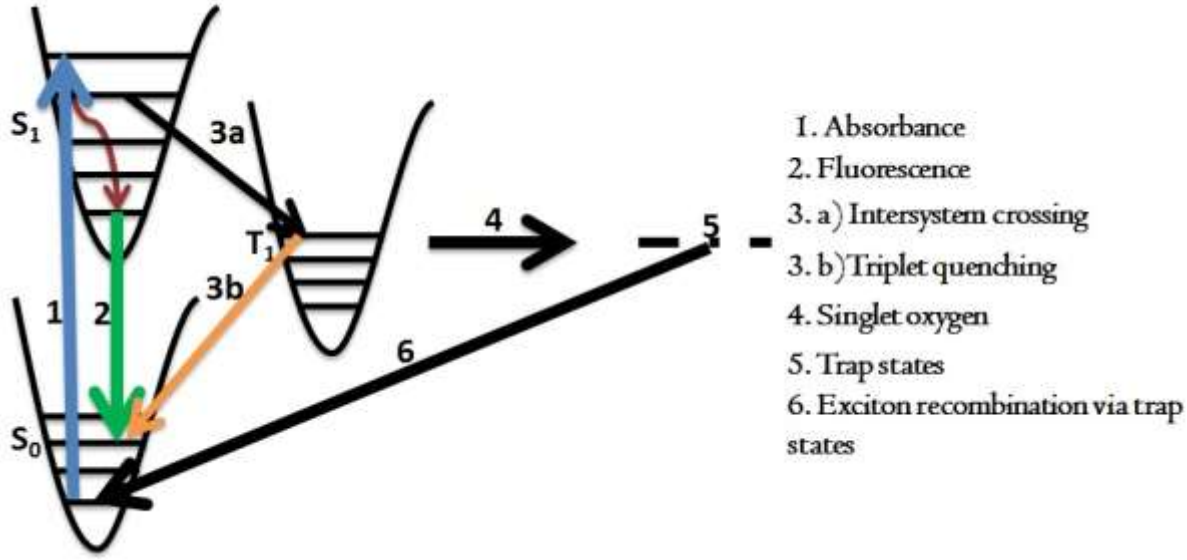

Figure 2.9: photo-oxidation mechanism of conjugated polymers[56]

Fig. 2.9 illustrates the mechanism of photo-oxidation in illuminescent conjugated polymer devices[53,56]. The polymer can be excited by visible light (step 1) yielding a singlet exciton. This exciton can recombine to the ground state by radiative process, called fluorescence (step 2). Another possibility is the relaxation of the singlet via

InterSystem Crossing (ISC) to the energetically favorable triplet state (step 3a). Additional reactions emerge upon introduction of molecular oxygen, which has a triplet ground state configuration ($3O_2$). The polymer triplet excitons can undergo energy transfer (ET) to the triplet oxygen to generate excited singlet oxygen ($1O_2$*) (steps 4,5).

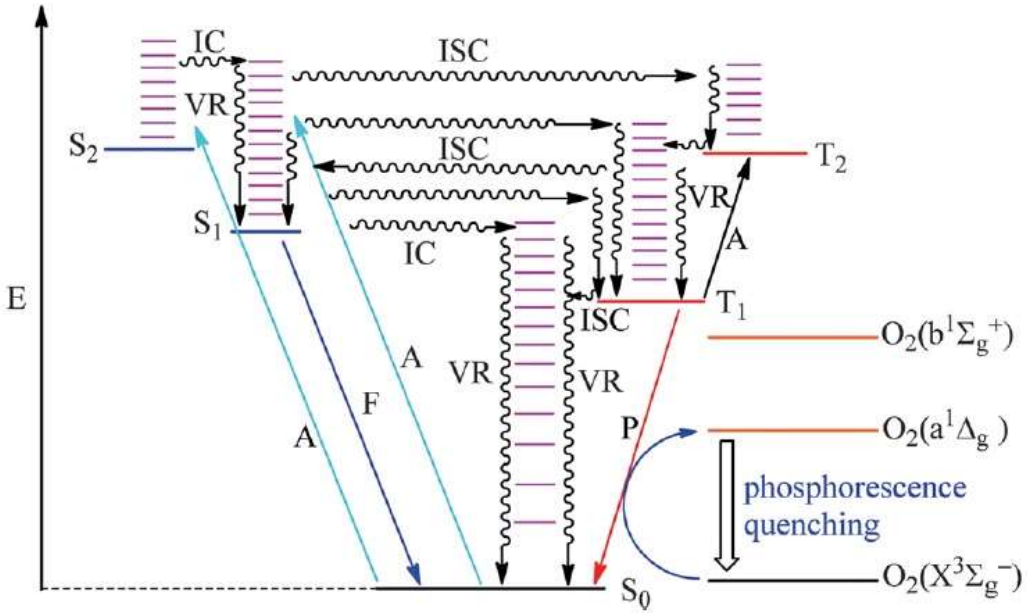

Figure 2.10: Jablonski diagram complimented with the singlet and triplet energy states of O_2: E – energy, A – absorption, F – fluorescence, P – phosphorescence, IC – internal conversion, ISC – intersystem crossing, VR – vibrational relaxation, S – singlet state, T – triplet state.[57]

Unlike many other molecules, the electronic ground state of oxygen, O_2 ($X^3S^-_g$), is a spin triplet. On the other hand, the two lowest-energy excited electronic states of oxygen, $O_2(a^1\Delta_g)$ and $O_2(b^1S^+_g)$, are spin singlets. The $a^1\Delta_g$ state is commonly called "singlet oxygen"[57] (Figure 2.10). Singlet oxygen reacts with the conjugated polymer backbone resulting in formation of photoluminescence quenching defects. For quenching to occur, the emissive molecule and quencher must be in molecular contact so that their electron clouds can interact[58]. This gives an alternative, non- radiative relaxation path of polymer excitons. Since the triplet exciton drives this process, controlling the triplet exciton dynamics will slow the photo-oxidation process.

Chapter 3: Graphene Oxide and Other Two Dimensional (2D) Materials

3.1. Graphene Oxide (GO)

Graphene was recently isolated by repeatedly peeling highly oriented pyrolytic graphite (HOPG) using scotch tape. Graphene is an allotrope of carbon in the form of a two-dimensional, atomic-scale, honey-comb lattice in which one atom forms each vertex (figure 3.1). It is the basic structural element of other allotropes, including graphite, charcoal, carbon nanotubes and fullerenes. It can also be considered as an indefinitely large aromatic molecule, the ultimate case of the family of flat polycyclic aromatic hydrocarbons. Some of the most useful properties of graphene is that it is a zero-band gap semimetal with very high electrical conductivity and thermal conductivity (~ 5000 $Wm^{-1}K^{-1}$), high carriers mobility (200000 $cm^{-2}V^{-1}s^{-1}$) and optical transparency (~ 97,7%).

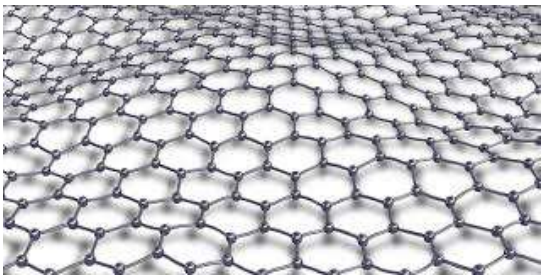

Figure 3.1 : Image of Graphene sheet

On the other hand, graphene oxide is produced by oxidation of graphite oxide. By the oxidation of graphite using strong oxidizing agents, oxygenated functionalities are introduced in the graphite structure (epoxy and hydroxyl groups lie above and below each graphene layer and carboxylic groups exist usually at the edges of the layers) which not only expand the layer separation, but also makes the material hydrophilic (figure 3.2). This property enables the graphite oxide to be exfoliated in water using sonication, ultimately producing single or few layer graphene, known as graphene oxide (GO). The main difference between graphite oxide and graphene oxide is, thus, the

number of layers. While graphite oxide is a multilayer system, in a graphene oxide dispersion a few layers flakes and monolayer flakes can be found.

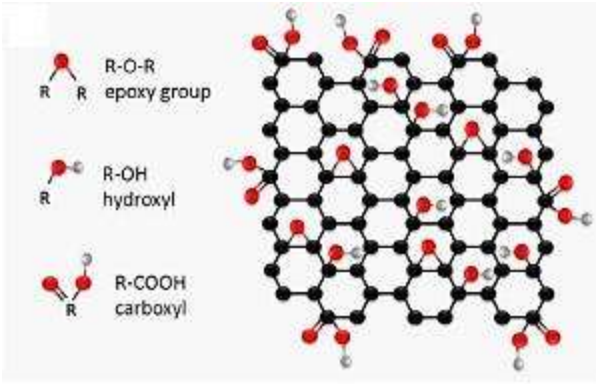

Figure 3.2: Chemical structure of Graphene Oxide

One of the advantages of the graphene oxide is its easy dispersability in water and other organic solvents, as well as in different matrixes, due to the presence of the oxygen functionalities. This remains as a very important property when mixing the material with ceramic or polymer matrixes when trying to improve their electrical and mechanical properties. On the other hand, in terms of electrical conductivity, graphene oxide is often described as an electrical insulator, due to the disruption of its sp^2 bonding networks. In order to overcome the electrical conductivity issue, reduction of the graphene oxide has to be achieved. It has to be taken into account that once most of the oxygen groups are removed, the reduced graphene oxide obtained is more difficult to disperse due to its tendency to create aggregates. Functionalization of graphene oxide can fundamentally change graphene oxide's properties.

Functionalization and dispersion of graphene oxide sheets are of crucial importance for their final applications. GO has been selected very often as the starting material for the formation of graphene derivatives through the covalent attachment of organic groups on its surface; the added groups are linked through the oxygen atoms of GO. Chemical/Photochemical functionalization of graphene oxide enables this material to be processed by solvent-assisted techniques, such as layer-by-layer assembly, spin-coating, and filtration[59].

3.2. Transition metal dichalcogenides: Tungsten Disulfide (WS_2) and Molybdenum Disulfide (MoS_2)

The unique properties of graphene have renewed interest in inorganic, two-dimensional materials with unique electronic and optical attributes. Graphene, while being fundamentally and technologically interesting for a variety of applications, is chemically inert and can only be made active by functionalization with desired molecules, which in turn results in the loss of some of its exotic properties. In contrast, single-layered 2D TMDs exhibit versatile chemistry. This offers opportunities for fundamental and technological research in a variety of fields including catalysis, energy storage, sensing and electronic devices such as field-effect transistors and logic circuits.

Transition metal dichalcogenides (TMDCs) are layered materials with strong in-plane bonding and weak out-of-plane interactions enabling exfoliation into two-dimensional layers of single unit cell thickness. TMDCs such as MoS_2, $MoSe_2$, WS_2 and WSe_2 have sizable bandgaps that change from indirect to direct in single layers, allowing applications such as transistors, photodetectors and electroluminescent devices. TMDCs are a class of materials with the formula MX2, where M is a transition metal element from group IV (Ti, Zr, Hf and so on), group V (for instance V, Nb or Ta) or group VI (Mo, W and so on), and X is a chalcogen (S, Se or Te) (figures 3.3, 3.4).

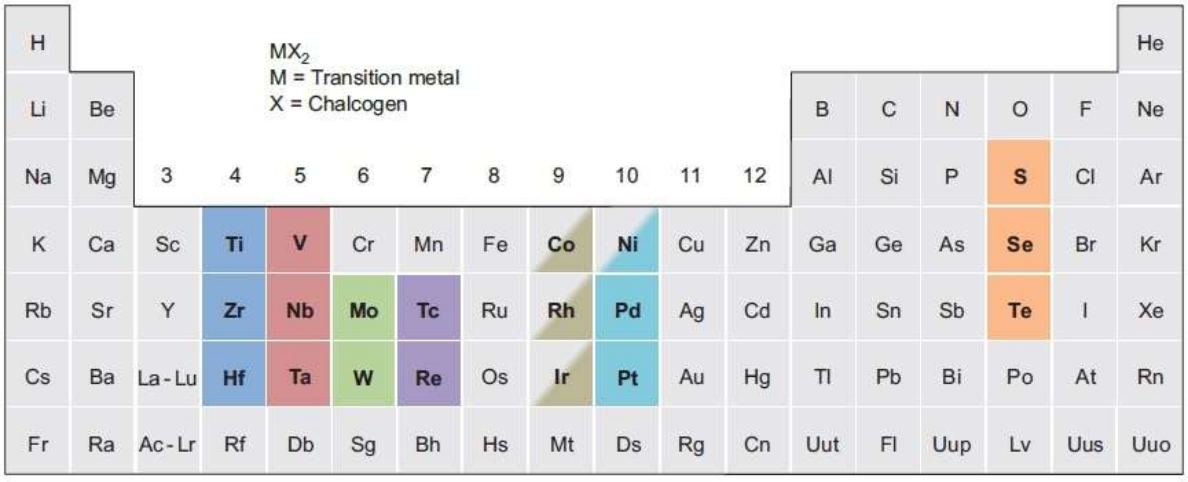

Figure 3.3: The transition metals and the three chalcogen are highlighted in the periodic table. (anafora chhowalla2013)

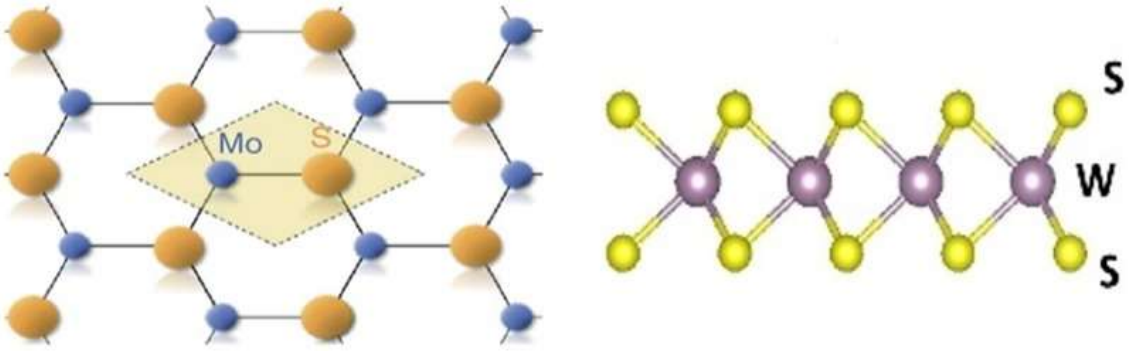

Figure 3.4: Chemical structure of MoS_2 (left) and WS_2 (right)

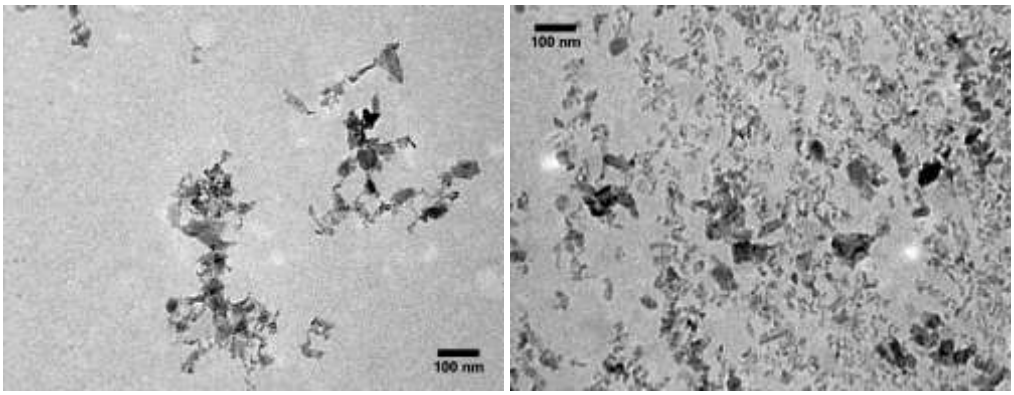

Figure 3.5: TEM images of MoS_2 (left) and WS_2 (right) nanoflakes

The electronic properties of TMDCs range from metallic to semiconducting. The layer-dependent properties of TMDCs have recently attracted a great deal of attention. For example, in several semiconducting TMDCs there is a transition from an indirect band-gap in the bulk to a direct gap in the monolayer: for MoS_2 the bulk indirect bandgap of 1.3 eV increases to a direct bandgap of 1.8 eV in single-layer form (figure 3.6) and for WS_2 the bulk indirect bandgap of 1.4 eV increases to a direct bandgap of 1.9 eV (figure 3.7). TMDs bandgap energy, as well as carrier type (n- or p-type), varies between compounds depending on their composition, structure and dimensionality.

Each layer typically has a thickness of 6~7 Å, which consists of a hexagonally packed layer of metal atoms sandwiched between two layers of chalcogen atoms. The intra-layer M–X bonds are predominantly covalent in nature, whereas the sandwich layers are coupled by weak van der Waals forces thus allowing the crystal to readily cleave along the layer surface. In general, there are many interesting layer-dependent properties in 2D materials, including graphene and TMDCs, which differ greatly from the properties of the bulk materials.

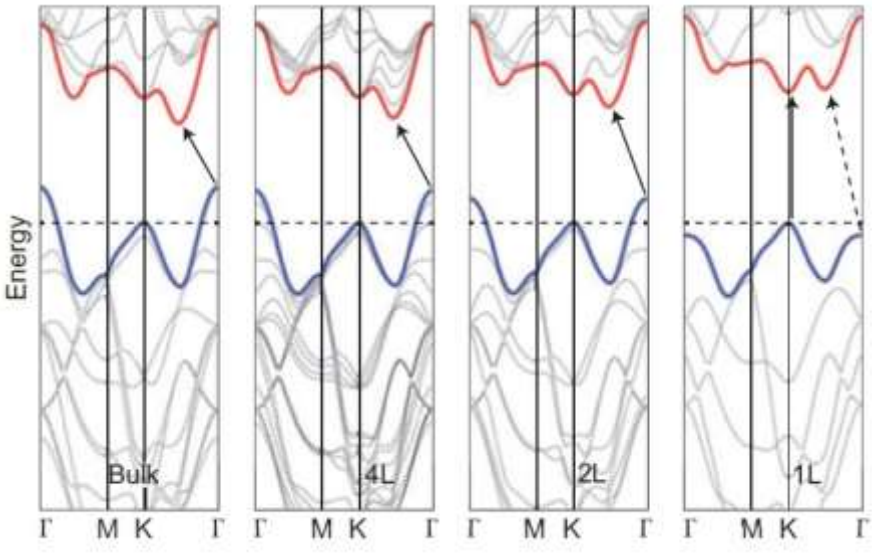

Figure 3.6: Energy versus wavevector *k* in bulk, quadrilayer (4L), bilayer (2L) and monolayer (1L) MoS2 from left to right[60]

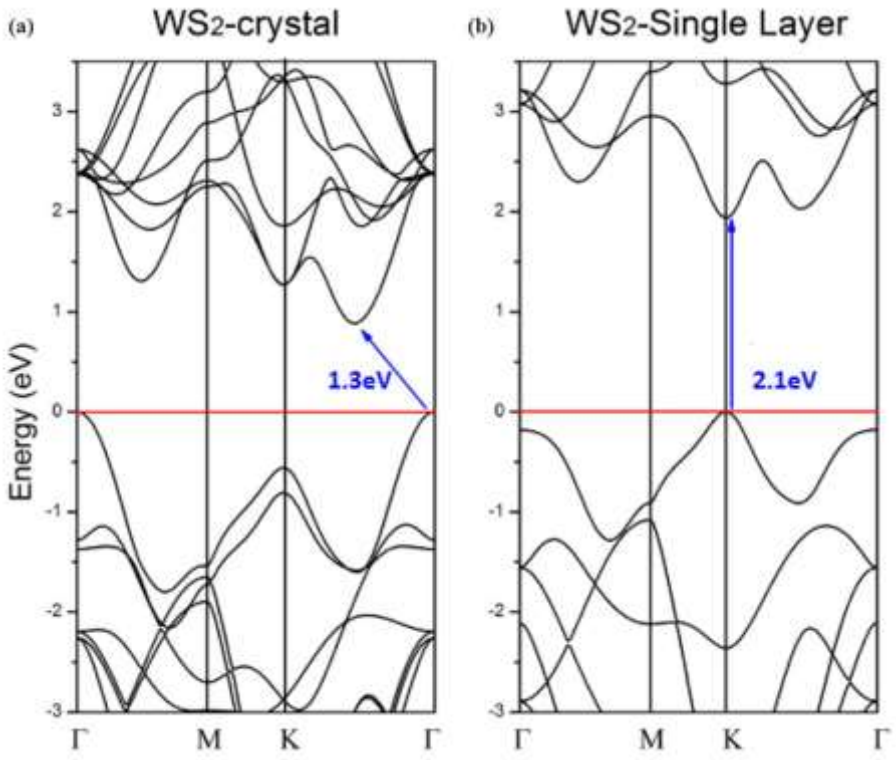

Figure 3.7: Band structure calculated from first-principle density function theory (DFT) for (a) bulk and (b) single-layer *WS*2. The blue arrows indicate the lowest energy transition[61].

3.3. Boron Nitride (BN)

Boron nitride (BN) is the lightest Group III-V compound. It closely resembles elemental carbon structures by sharing the same total number of electrons between the neighboring atoms. Boron nitride has been produced in amorphous (a-BN) and crystalline forms. The comparable isoelectric BN polymorphs are the hexagonal (h- BN) and cubic BN (c-BN), which similarly consist of layered and tetrahedral structures, respectively. Unlike the carbon fullerenes such as C_{60}, however, BN fullerenes feature squares or octagons rather than pentagons in order to avoid thermodynamically unfavorable B-B and N-N bonds.

The most stable crystalline form is the hexagonal one, h-BN (graphitic BN). Hexagonal boron nitride has a layered structure similar to graphite (figure 3.8). Within each layer, boron and nitrogen atoms are bound by strong covalent bonds, whereas the layers are held together by weak van der Waals forces. The interlayer "registry" of these sheets

differs, however, from the pattern seen for graphite, because the atoms are eclipsed, with boron atoms lying over and above nitrogen atoms. This registry reflects the polarity of the B-N bonds.

High-purity h-BN crystals show promising semiconductor characteristics due to a direct band gap of 5.97 eV. Similar to aluminum nitride (AlN) and gallium nitride (GaN), h-BN may have attractive potential as a wide–band gap material. The layered structure of h-BN makes the material mechanically weak, but it has greater chemical and thermal stability than GaN and AlN. The interesting optical properties of h-BN, such as its huge exciton-binding energy, are due to its anisotropic structure, whereas a single crystal's basal plane in h-BN is not easily broken because of its strong in-plane bonds.

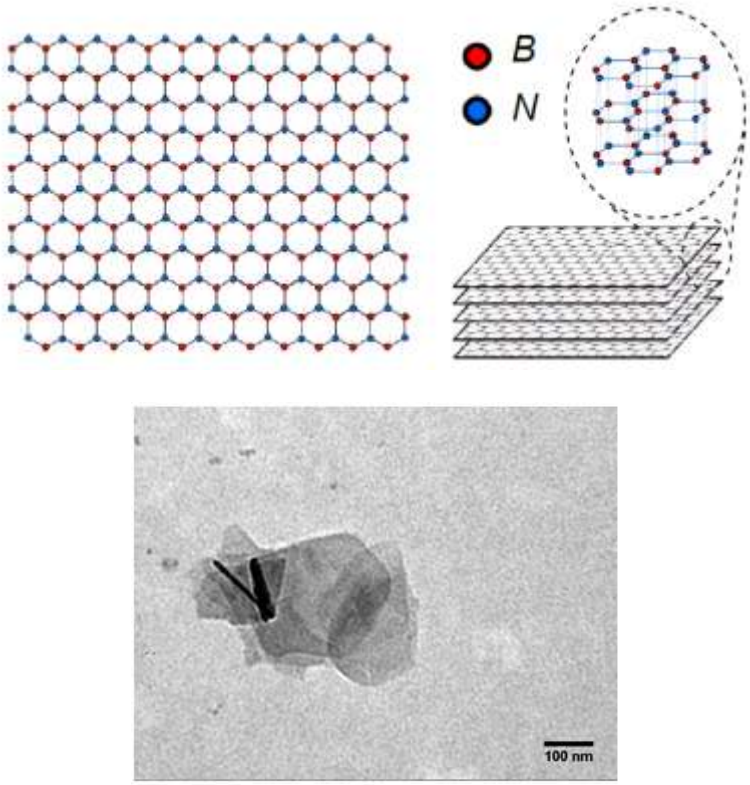

Figure 3.8: Chemical structure (top) and TEM image (bottom) of h-BN layers

Chapter 4: Laser based techniques for OPV materials synthesis, modification and diagnostics

4.1. Photoluminescence-Laser Induced Fluorescence (LIF) spectroscopy

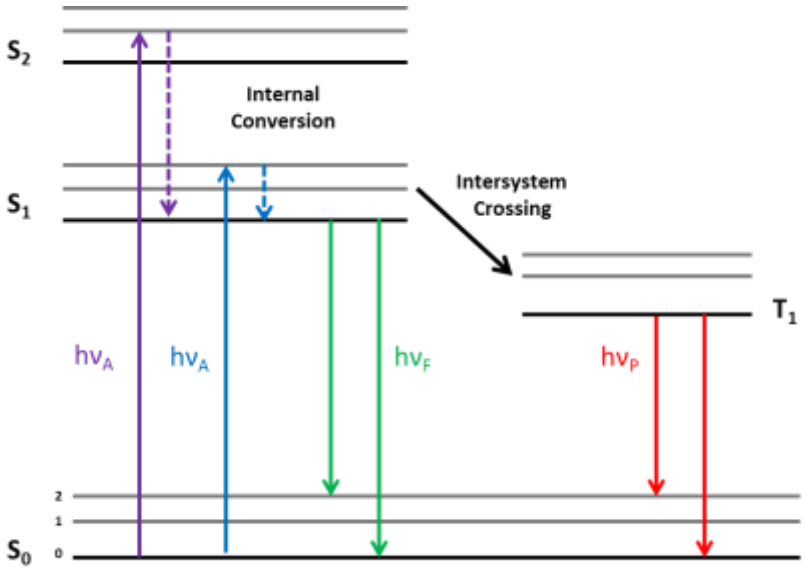

Figure 4.1: Jablonski diagram

Photoluminescence spectroscopy has been extensively used in many studies as a useful tool for the examination of the underlying degradation mechanisms in polymers. It is a nondestructive method to probe the electronic structure of materials[58]. During the analysis, laser beam is directed onto the sample and imparts excess energy into the materials, which causes electron within a material to move into permissible excited states. When these electrons return to their equilibrium states, the excess energy is released either as emitted light (radiative process) or thermal energy (nonradiative process). In these processes, light emission (includes fluorescent and phosphorescent

emissions) is called PL. The energy of the PL relates to the difference in energy levels between the two electron states (excited states and equilibrium state). These absorption and emission processes can be understood using a simplified form of a Jablonski diagram (Figure 4.1). In this diagram, the singlet ground, first and second electronic states are presented by S_0, S_1 and S_2, respectively. Following light absorption, several processes usually occur. The fluorophores are usually excited to some higher vibrational levels of either S_1 or S_2[58]. Thermalization of the excess vibrational energy usually relaxes the molecule to the lowest vibrational level of S_1, generally with lifetimes within 10^{-12} s. However, the lifetimes of fluorescence emissions are typically near 10^{-8} s. The fluorescence emission generally results from a thermally equilibrated excited state (the lowest energy vibrational state of S_1). The return of fluorophores to the ground state typically occurs to a higher excited vibrational ground state level firstly, then quickly (10^{-12} s) reaches thermal equilibrium[58]. That is the reason why a typical PL position is lower in energy than that of the corresponding excitation energy. The energy gap between the PL and the corresponding excitation energy is called as Stokes Shift. When a fluorophore is in the first excited singlet state S_1, it can also undergo a spin conversion to the first excited triplet state T_1 via intersystem crossing (ISC)[58]. Radiative emission from T_1 to S_0 is called phosphorescence, which is generally shifted to lower energies than fluorescent transitions. The T_1 – S_0 transition is forbidden but this condition can be broken, resulting in phosphorescent decay rates typically several orders of magnitude smaller than for fluorescence[58]. PL spectra are recorded at low and room temperature in vacuum. The samples are mounted in a cryostat and are excited with lasers at 325 nm. The laser beam is directed on the sample through the sapphire windows of the cryostat.

Laser Induced Fluorescence (LIF) is a spectroscopic method with similar concept to PL. Laser irradiation is used for the excitation of the sample. The collected fluorescence signal is guided to an iCCD camera through a spectrograph and the corresponded spectrum is illustrated in a computer. This technique is focused on the detection of the emitted photons after the S_1-S_0 transition. Fluorescence spectra are recorded at room temperature. In this work, the 2nd harmonic of Nd:Yag laser @ 532 nm, with pulse duration 10 ns was used for the LIF experiments. Based on these considerations, the

electronic structure of semiconductors can be probed well using these spectroscopic methods.

As it has been mentioned in section 2.5, oxygen may act as a photoluminescence quencher in polymers[58] (figure 4.2).

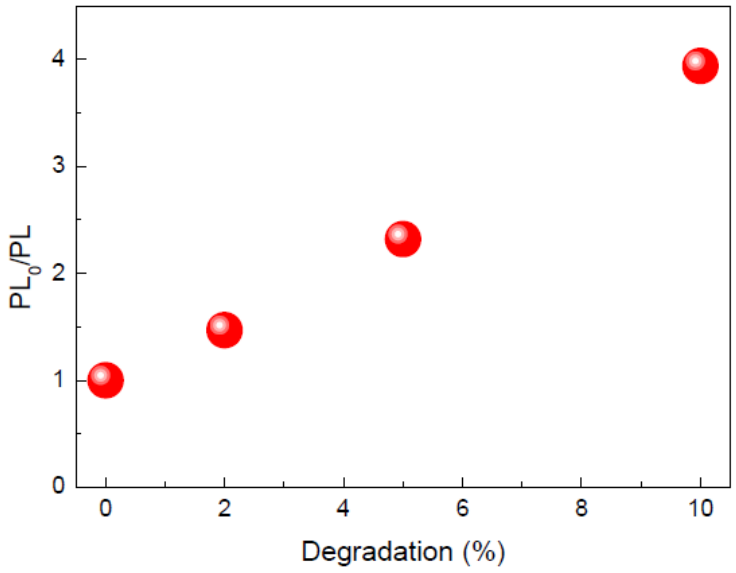

Figure4.2: Stern-Volmer plot of the emission of the samples versus the degradation after exposure to air and light[54]

There are different kinds of luminescence quenching. Dynamic or collisional quenching occurs when the luminescence of a material is reduced upon contact with the quencher and depends on their relative positions at the moment of the excitation[54,58]. Therefore, the rate of collisional quenching in a thin film depends on the morphology. Another frequently observed quenching mechanism occurs when the quencher forms complexes with the emissive molecule in the ground state. This phenomenon is referred to as static quenching. Quenching of luminescence is formally described by the Stern-Volmer equation

$$\mathbf{PL_0/PL = 1 + K_{D,S}Q}$$

in which the ratio between the luminescence intensity in the absence (PL_0) and presence (PL) of the quencher is expressed as a function of the quencher concentration (Q) through the quenching constant (K_D in case of dynamic quenching or K_S for static

quenching)[58]. In many cases, quenching is the result of both collisions and ground-state complex formation with the same quencher[58]. The Stern-Volmer equation, in this case, results in a parabolic behavior with upwards curvature and can be expressed as follows:

$$PL_0/PL = (1 + K_DQ)(1 + K_SQ)$$

According to literature, the utilization of nanoparticles in conjugated polymer matrix retards the oxidation of the polymer[62,63]. Working towards this direction, the photoluminescence study of 2 different BHJ systems, P3HT:$PC_{60}BM$ and PCDTBT:$PC_{71}BM$ doped with metallic nanoparticles, is reported, in order to understand the contribution of metallic nanostructures to the photooxidation process. The gold and aluminum nanoparticles have been fabricated via laser ablation in liquid[64,65]. As it has been already mentioned in section 2.5, triplet excitons of the donor-polymer may excite singlet oxygen that will react with the polymer chains, creating oxygen trap states. According to literature, by incorporating the metallic nanostructures inside the active layer the absorption band of metallic nanoparticles may overlap the triplet exciton band energy of the polymers, preventing this way the creation of oxygen trap states and photoluminescence quenching. In figure 4.3, the role of nanoparticles as a blocker of polymer triplet excitons is shown.

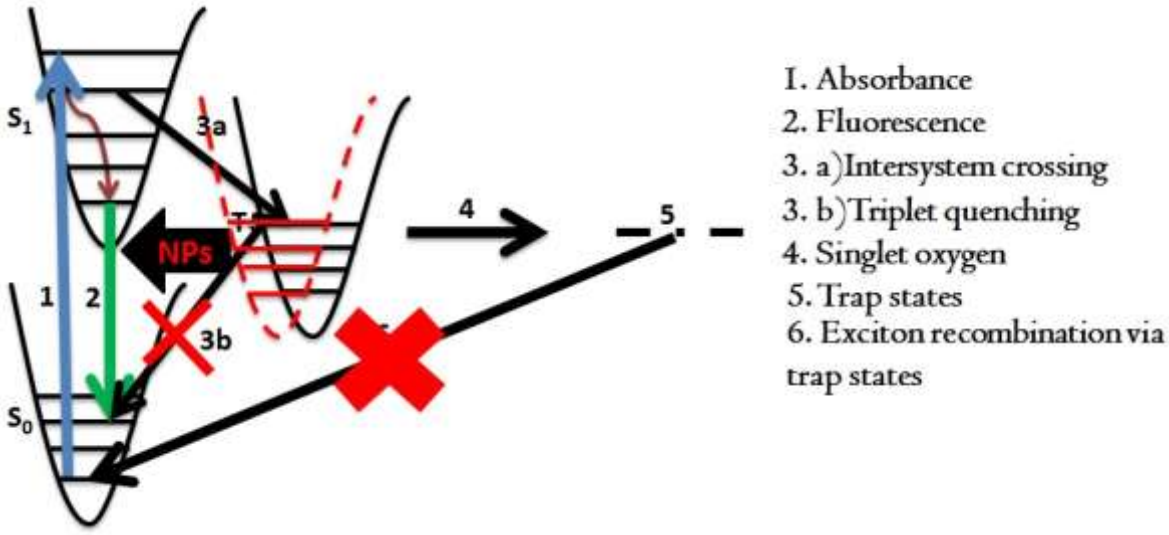

Figure 4.3: Schematic of the photoluminescence

For this purpose, we used LIF and photoluminescence spectroscopy in order to monitor the emission decay of the metallic-doped devices compared to the reference ones. In figure 4.4, an example of a LIF setup is presented. There have been two sets of measurements; in the first, the devices-under study- were illuminated with a solar simulator and in the second, the devices were under dark storage. More details about the experiment are mentioned in Chapter 5.

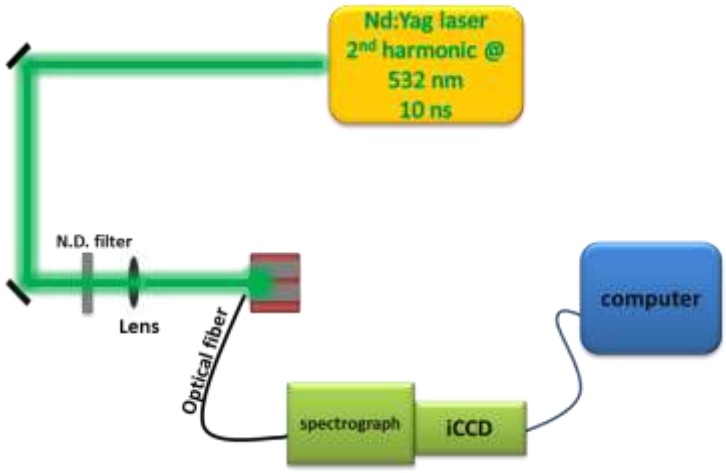

Figure 1.4: Schematic of a LIF setup

4.2. Laser-assisted synthesis of materials in solution

Laser synthesis of nanoparticles via laser ablation in liquids

The laser synthesis of metallic nanoparticles with laser ablation of solids in liquid media is a well-known method for the fabrication of surfactant-free NPs with relatively controllable size distribution[66]. This technique is simple and has the advantage of producing a large variety of NPs that are free of both surface-active substances and counter-ions. The absence of unnecessary reagents such as stabilizers and byproducts that are usually generated in chemical syntheses becomes useful when NPs are used for applications. NPs of different morphologies exhibit distinct optical responses due to the collective oscillations and localization of conduction electrons giving rise to LSPR modes[2]. Laser radiation is focused onto a solid target immersed in a liquid. It is assumed

that the liquid is transparent at laser wavelength while laser irradiation is absorbed by the target. The solid target is placed under a thin (several millimeters) layer of liquid and is exposed to laser irradiation. Different laser sources have been used on this purpose. The only necessary requirement is that the density of the laser energy is high enough to induce local melting on the target and eventual generation of NPs. Laser induced breakdown of submerged targets is characterized by visible plasma emission and the production of shock waves and of cavitation bubbles[67]. The duration of each of these processes is sketched in fig. 4.5. After laser-matter interaction, laser-induced breakdown occurs, followed by the shock wave formation, plasma expansion and cooling, and by cavitation bubble formation, expansion and collapse. Upon the bubble collapse, the nanoparticles, which are produced during the plasma cooling phase, can diffuse in the surrounding liquid and form a colloidal solution[67].

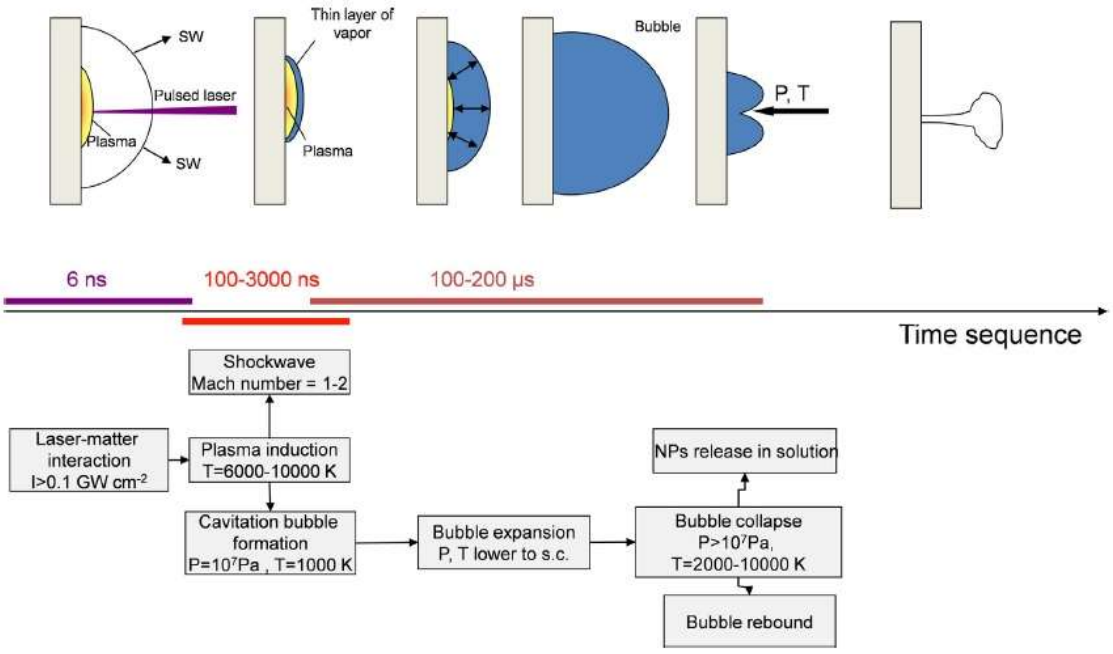

Figure 4.5: Time sequence of the processes involved during pulsed laser ablation in liquid with ns laser[67]

According to literature, different laser parameters, like laser wavelength, pulse duration, energy density and repetition rate have different effects on the efficiency of generation of NPs[66]. In general, the average size of NPs is determined by the laser fluence on the target and not by the duration of the laser pulse[66]. Some metals, like aluminum, are highly reactive with ambient oxygen. The high reactivity can partially be

compensated by ablating using short laser pulses due to faster quenching which could minimize the formation of either oxide or hydroxide on the particle surface. Furthermore, oxidation of NPs generated by this technique can be additionally suppressed by carefully outgassing the air trapped in liquid and/or replacement of it by a neutral gas[64].

The oxidation of NPs generated by laser ablation is closely related to the laser pulse width. Ultrashort laser pulses produce mostly metallic NPs without oxide shell. The NPs are oxidized slowly due to diffusion of air oxygen into the colloidal solution[64]. On the contrary, the longer pulse duration of 150 ps leads to visible oxidation of as-generated NPs. However, in the latter case this oxide shell may provide better stability of NPs against further oxidation by air oxygen serving as a protective layer[64].

Moreover, the absorption maximum due to LSPR of metallic nanoparticles, is dependent to the diameter of the NPs and may be shifted towards red region for higher diameters[64]. The LSPR of NPs is also affected by the liquid medium in which are generated/placed because of the different refractive index. It has been reported that the incorporation of metallic nanoparticles that were initially in ethanol, in the blend of the active layer of OPVs causes red shift of the absorption peak of the NPs[2]. Oxidation of Al NPs would also cause a red shift of their plasmon resonance, since its oxide, Al_2O_3, has higher refractive index in the UV range than water[64].

Photo-assisted synthesis of nanoparticles from liquid precursors

Working in the same concept, NPs generation can be achieved by irradiation of metallic precursors in liquid. For the decoration of two-dimensional (2D) nanosheets (NS) with noble metallic nanoparticles (NPs), the NS were irradiated with KrF excimer laser (248 nm, 20 ns) in the presence of precursors of metallic salts, without the contribution of any surfactants or catalysts. According to literature, when metallic salts are exposed to light (photolysis), generation of metallic nanoparticles occurs[68,69], as is described by the reactions 1 and 2, for silver nitrate ($AgNO_3$) and chloroauric acid ($HAuCl_4$), respectively.

$$AgNO_3 + H_2O \xrightarrow{h\nu} Ag^0 + HNO_3$$ **Reaction 1**

$$2AuCl_4^- \xrightarrow{h\nu} 2Au^0 + 3Cl_2 + 2Cl^-$$ **Reaction 2**

The proposed mechanism regarding the metal NPs anchoring in the GO sheet has been studied extensively[70,71] and is depicted in the figure 4.6 :

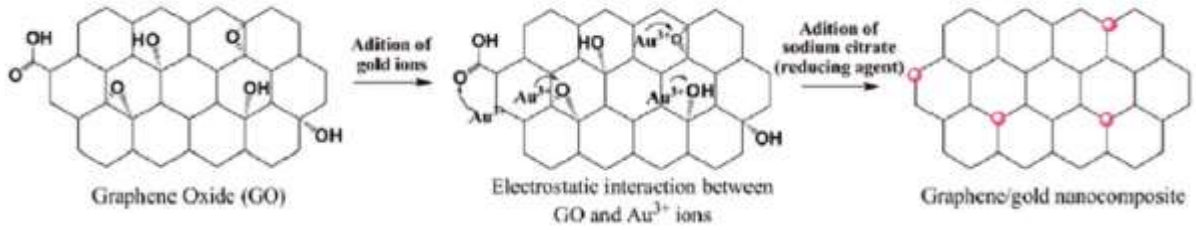

Figure 4.6: Schematic representation of the mechanism of nucleation of gold nanoparticles at functionalized graphene surface[70]

The driving force for the electron transfer from the GO to $AuCl_4^-$ cations stems from the difference between the Fermi levels of GO (4.7 – 4.9 eV below vacuum level) and the reduction potential of $AuCl_4^-$ (is equal to + 1V with respect to standard hydrogen electrode (SHE) potential, whose absolute potential is known to be from -4.43 to -4.73 eV below vacuum level) ($AuCl_4^- + 3e = Au + 4Cl^-$). Thus the Fermi level of GO is higher than the reduction potential of $AuCl_4^-$ and redox couples GO/$AuCl_4^-$ are formed allowing the spontaneous electron transfer from GO to $AuCl_4$ described above. This redox mechanism takes also place between the 2D transition dichalcogenide metals, WS_2 and MoS_2 (Fermi Levels -4.6 – (-) 4.9 eV), with the $AuCl_4^-$. The Fermi level of WS_2 and MoS_2 is 0.8 eV higher than the reduction potential of $AuCl_4$ (figure 4.7[71]) and this leads to successful metal nanoparticles decoration of the 2D NS. In addition, the fermi level of h-BN[72] is 3.31 eV below vacuum level, 2.1 eV higher than the reduction potential of $AuCl_4$, and this also supports the mechanism mentioned above. The suggested mechanism

could be suitable well for deposition of other noble metals with a low reduction potential of their soluble ions, like $AgNO_3$. Our preliminary experiments have shown that a similar synthesis with $AgNO_3$ solution rather than $HAuCl_4$ leads to formation of Ag nanoparticles on the surface of GO.

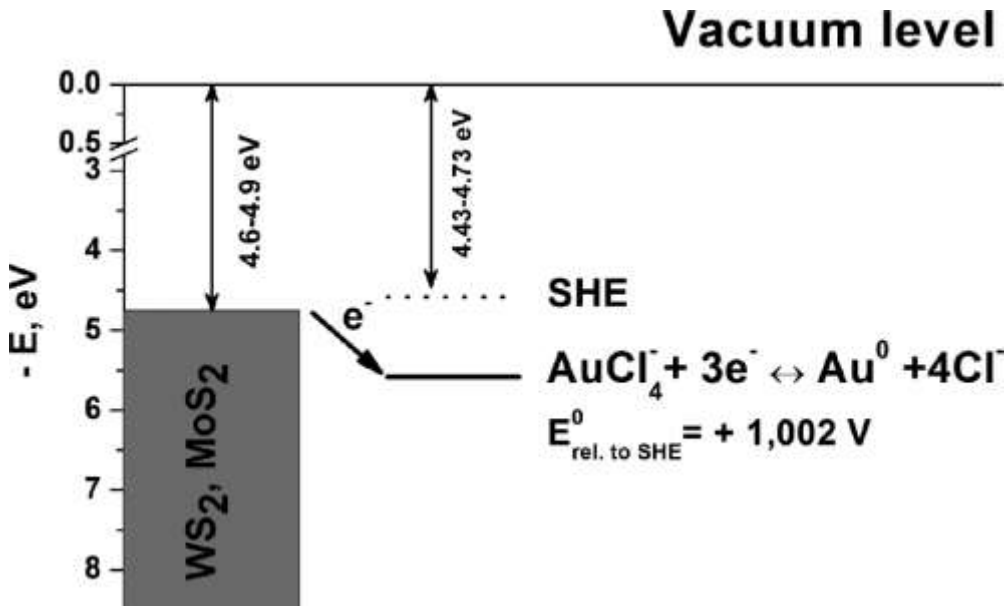

Figure 4.7: Energy scheme representing the relative positions of WS2/MoS2 Fermi levels and reduction potential of the $AuCl_4$ [71].

The preparation is based on photo-activation of NS surface by UV laser photons, followed by chemical reduction of the metallic precursor. No thermal reduction of graphene oxide sheet was envisioned. The oxygen groups of GO are considered as nucleation centers for metal nanoparticles and we would like to exploit them for the metal nanoparticles decoration. The laser intensity that is used for the irradiation of our sample is much lower than the rate that the photo-reduction of graphene oxide requests, so there are no reduction effects on graphene oxide sheets. The UV radiation of a mix solution of graphene oxide and Au metal precursor induces a very reactive environment localized at and around the graphene oxide sheets. The combination of the plasmonic effect in GO – Au NPs solution provides enhanced photothermal effects during laser irradiation that induces melting of the metal NPs. The latter mechanism leads to smaller diameter metal NPs after laser irradiation. The presence of oxygen functionalities at the graphene surface provides reactive sites for the nucleation and

growth of gold NPs. More particularly the nucleation and the growth of metal nanoparticles depends on the degree of oxygen functionalization at the graphene surface sheets. The higher the density of oxygen functional groups promoted the dispersion of gold NPs along graphene oxide sheet's surface. On the contrary a lower density of these groups promoted the growth of Au NPs agglomeration. The UV photoinduced heating (transfer of thermal energy from irradiated GO to the aqueous medium) generates hot and reactive spots at the graphene oxide sheets and their close vicinity. This environment triggers the reduction of the $AuCl_4^-$ anion reduction towards the generation of Au metal nanoparticles. The latter are anchored on the reactive edges and reactive surface (irradiated areas) of the graphene oxide establishing electrostatic type links with the defect sites. The nucleation of Au NPs at GO surface should be mainly governed by the presence of oxygen groups at GO which contribute to an overall negatively charged surface (electrostatic type attachment or linkage). The size of the anchored nano-particles strongly depends on the oxidation level of the graphene template; the more the oxygen groups the smaller the Au NPs that can be obtained (~ 5-10 nm)[70,73].

Additionally, non-oxygen contained defect sites in (1) basal plane and (2) around wrinkled and folded areas between sheets can act as nucleation centers for the anchoring of metal nanoparticles.

Also another topic under investigation is the potential of the universal use of an optical (laser) technique for the decoration of novel 2D materials with metal, free of surfactant NPs beyond graphene. According to our knowledge and based on a literature review that has been performed, it is the first time that a laser induced decoration of other 2D materials (BN, MoS_2 and WS_2) has been reported. The results for GO decoration were presented as a proof of concept that the proposed laser technique can be successfully applied to the other 2D materials. Moreover, for the first time the applicability of a 2D materials platform with metal NPs is demonstrated in ternary OPVs architecture, providing a) the appropriate energy cascade to facilitate the transfer of photogenerated carriers to the respective electrodes and b) the exploitation of scattering and the local plasmonic effect (LSPR) by the use of various sizes metal NPs. In Chapter 6, the

experimental procedure and the applicability of the produced materials in ternary OPV devices is presented.

4.3. Laser induced reduction of Graphene Oxide

Graphene oxide can be used as an effective route to graphene-like materials. Because of the oxygen-containing groups (OCGs) on the graphene sheets, GO becomes insulating and that reduces significantly its applications, especially for electronics. Therefore, reduction methods must be used in order to remove OCGs. Different reduction methods have been developed for the removal of oxygen-containing groups, such as thermal[74,75] and chemical[28,76,77,78,79]reduction. In recent years, photo-reduction has emerged as an appealing alternative because photo-reduction does not rely on either high temperature or toxic chemicals. Photo-reduction of GO has unique properties such as mask-free patterning, room-temperature processing, chemical-free and non-contact treatment, controllable reduction, as well as the formation of micro-nanostructures.

Laser has been employed for deoxygenation of graphene, dehydrogenation and dehalogenation of graphene surface. Such laser induced bond dissociation paves the way for achieving desired band gap in graphene by adequately controlling the extent of such surface bonds. It has been confirmed that upon UV laser irradiation GO reduction is achieved[35,80], without any photocatalysts (figure 4.8). In spite of a certain amount of carboxyl groups remaining, most of the hydroxyl groups of the GO could be selectively removed through this simple irradiation. According to Smirnov's results, the threshold for GO reduction is 3.2 eV ($\lambda < 390$ nm).

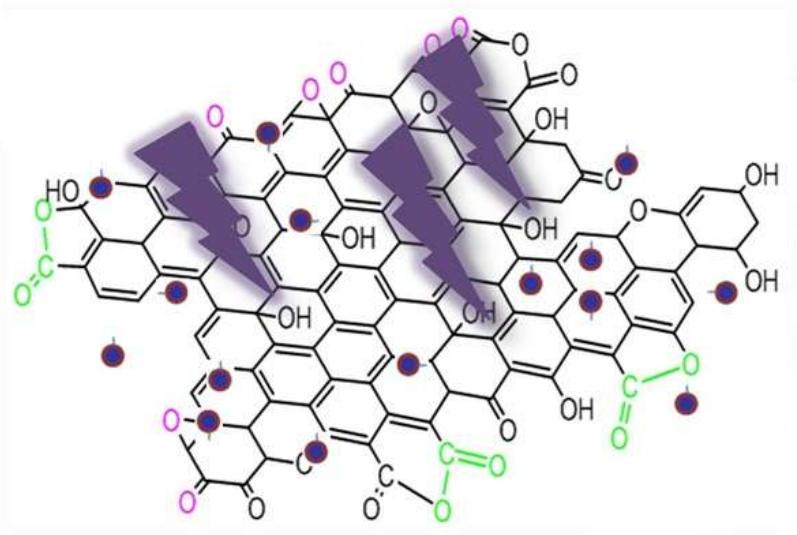

Figure 4.8: Schematic of GO reduction upon UV laser irradiation

In principle, reduction of GO could be achieved either by UV or visible laser source. If the laser source has wavelength smaller than 390 nm, for instance an excimer laser (248 nm), GO would mainly undergo a photochemical process, whereas for laser sources with wavelength larger than 390 nm, GO undergoes photothermal process. Since the energy is provided by a light source, precise control over the wavelength range, intensity and exposure duration lead to the controllable reduction of GO. As it is presented in Chapter 7, photochemical reduction technique proved to be a useful tool for the functionalization of GO.

Chapter 5: Laser based synthesis of materials and diagnostics to enhance the performance and stability of organic solar cells

5.1. Introduction

Enhancement of both the efficiency and stability of bulk heterojunction (BHJ) organic photovoltaic (OPV) devices is reported by the addition of surfactant-free metallic (gold-Au and aluminium-Al) nanoparticles (NPs) into the photoactive layer. The universality of the effect is demonstrated for two different BHJ systems, namely the well-studied P3HT:PC_{60} M as well as the high efficient PCDTBT:PC_{71}BM. It is shown that the lifetime of the devices with metallic NPs, operating under continuous one-sun illumination in ambient conditions, is more than three times longer compared to the reference devices. Using complementary analytical techniques for in-situ studies, we have explored the underlying mechanisms behind the observed stability improvement in the case of P3HT:PCBM system. In particular, Laser Induced Fluorescence (LIF), Photoluminescence decay and Fourier Transform InfraRed (FTIR) spectroscopy experiments were performed and complemented with device degradation electrical measurements. It is found that the embedded NPs act as performance stabilizers, giving rise to enhanced structural stability of the active blend. Furthermore, it is revealed that, the observed improvement can also be ascribed to a NPs-mediated mitigation of the photo-oxidation effect. This study addresses a major issue in OPV devices that is photoinduced stability, indicating that the exploitation of metallic NPs could be a successful approach towards fabricating OPVs exhibiting long-term operating lifetimes.

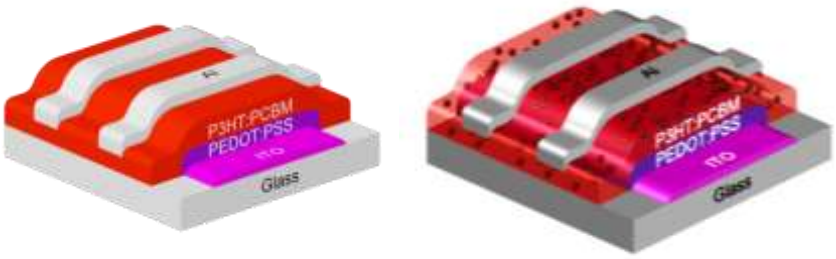

Scheme 1: Schematic representation of a (a) pristine and a (b) metallic doped OPV device

5.2. Experimental

NPs generation

Details for the generation procedure of metallic NPs have already been reported elsewhere[64,81,82]. The generation of metal NPs was performed by ultrafast (femtosecond or picosecond) laser ablation of metallic targets (99.99%). The targets were placed into a Pyrex cell and completely covered by a layer of absolute ethanol. A femtosecond laser beam (wavelength of 800 nm, pulse duration of ~100fs and repetition rate of 1kHz) was focused onto the target. The cell was mounted on a stage, continuously rotated during laser exposure. Laser irradiation gives rise to a high temperature gradient in the metal bulk and melts a thin layer of the target. A fraction of the molten layer of the target is dispersed into the liquid in the form of NPs. As prepared NPs were spherical and had relatively uniform diameters. The respective size distribution determined from a series of TEM images (Figures 5.1 and 5.2) indicates that the majority of Al NPs exhibit sizes ranged from 10 to 70 nm with an average of ~30 nm and while the majority of Au nanoparticles[5] exhibit sizes ranged from 5 to 70 nm with an average ~ 10 nm.

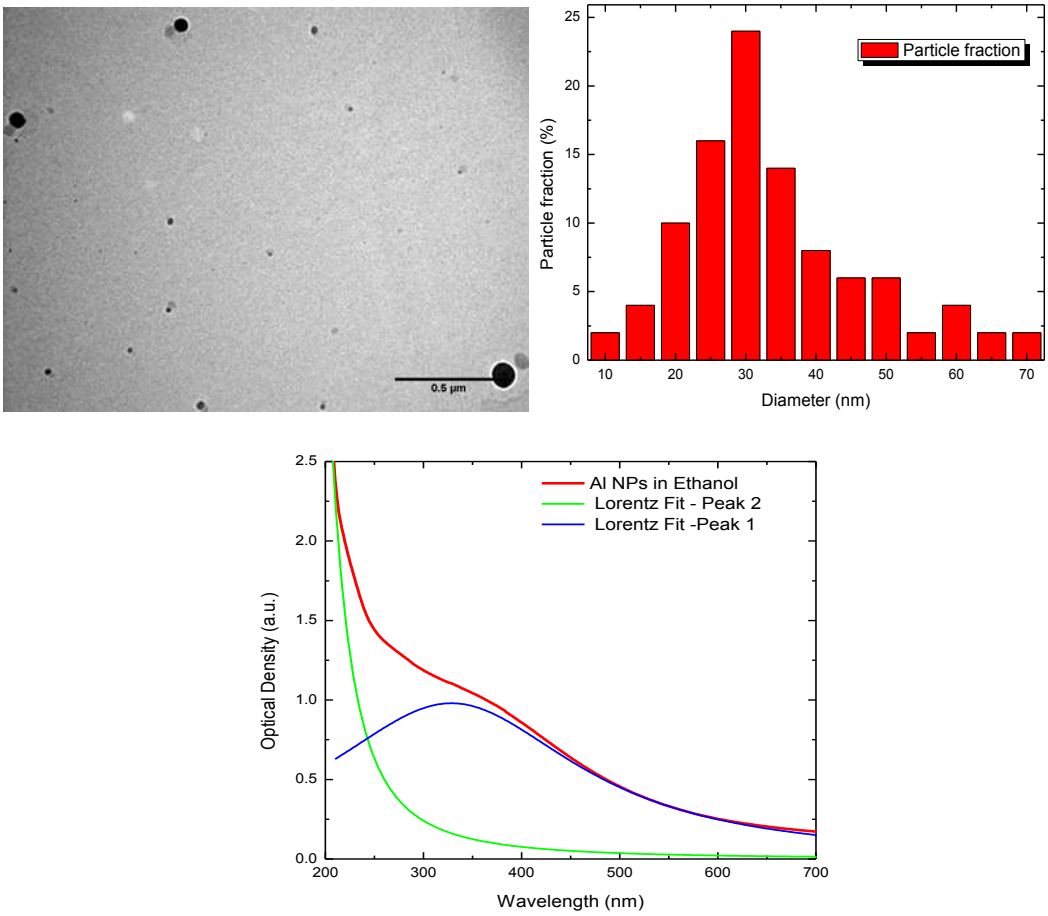

Figure 5.1: TEM image of the fabricated Al NPs (top left) and size distribution of the fabricated nanoparticles (top right). UV-Vis absorption spectrum of Al NPs in Ethanol (bottom). The respective curve fit, performed via Lorentzian peak analysis, is additionally presented.

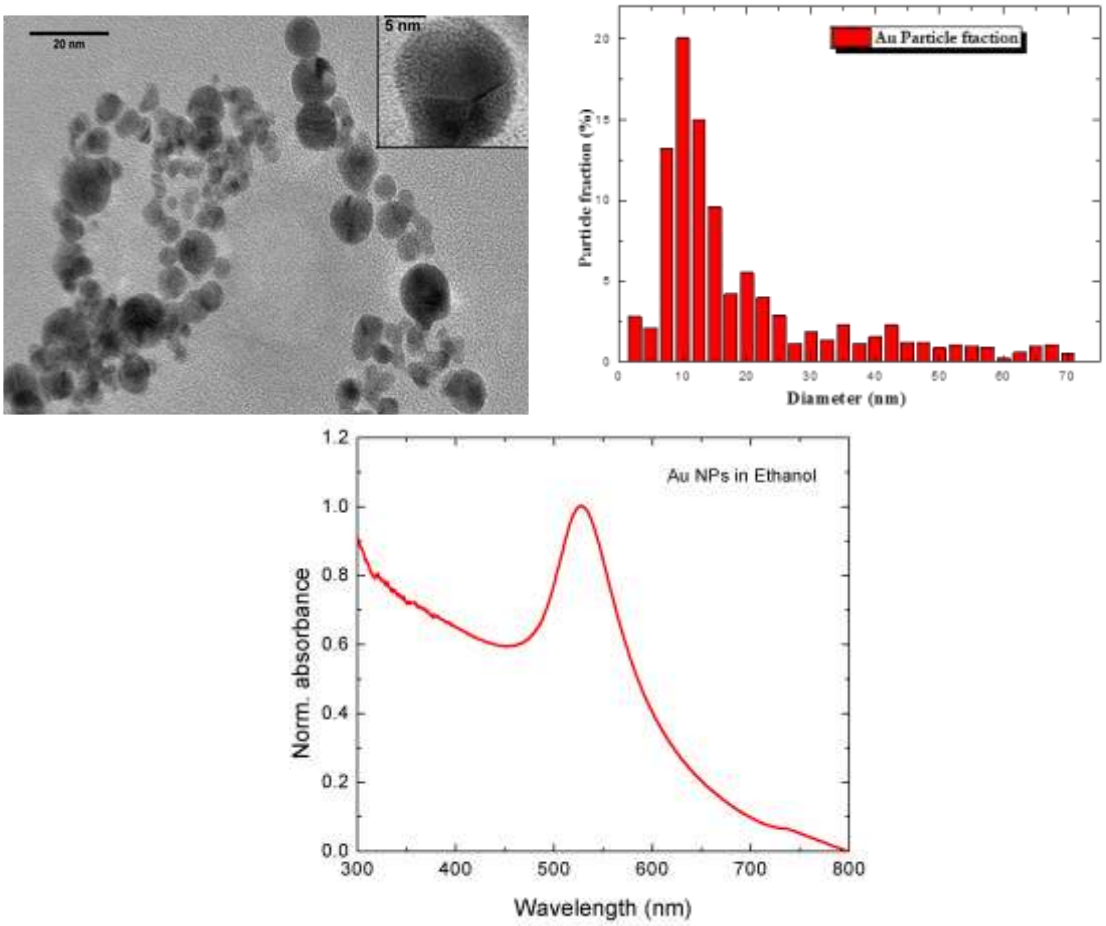

Figure 5.2: TEM image of the fabricated Au NPs (top left) and size distribution of the fabricated nanoparticles (top right)[5]. UV-Vis absorption spectrum of Au NPs in ethanol (bottom)[5].

TiO_x solution preparation

Titanium (IV) isopropoxide ($Ti[OCH(CH_3)_2]_4$, 5 ml), 2-methoxyethanol ($CH_3OCH_2CH_2OH$, 20 ml) and ethanolamine ($H_2NCH_2CH_2OH$, 2 ml) were added to a three-necked flask under nitrogen atmosphere. The solution was then stirred for 1 h at room temperature, followed by heating at 80 °C for 1h and 120 °C for additional 1h. The solution was then cooled to room temperature and 10 ml of methanol was added.

Device fabrication

Regioregular (rr) P3HT was purchased from Rieke Metals and PCBM was purchased from Nano-C. rr-P3HT and PCBM based OPV devices were dissolved in dichlorobenzene (o-DCB) in a 1:1 ratio (40mg total concentration) and stirred overnight at 75°C. The PCDTBT:$PC_{71}BM$ blend was prepared according to the following procedure: PCDTBT (Solaris Chem.) and $PC_{71}BM$ (Solenne B.V.) (1:4 w/w), were dissolved in a mixture of chlorobenzene (CB) and o-dichlorobenzene (o-DCB) (1:3 v/v) and stirred overnight at 70 °C. The devices were fabricated on 20mm x 15mm indium-tin-oxide (ITO) glass substrates with sheet resistance of ~20 Ω/sq. As hole transport layer, poly(ethylene-dioxythiophene) doped with poly(4-styrenesulfonate) (PEDOT:PSS), purchased from Heraeus (Al 4083), was spin-cast from an aqueous solution on the ITO substrate at 5000 rpm for 30 seconds (average thickness ≈ 40 nm) for P3HT:PCBM and at 6000 rpm for 60 seconds (average thickness ≈ 30 nm) for PCDTBT:$PC_{71}BM$ based devices and was subsequently baked for 15 min. at 120 °C in ambient conditions. Following the preparation of the blends metallic NPs were blended into both solutions in nitrogen saturated atmosphere. In order to optimize the PV performances, composite blends with different wt% metallic NPs were initially prepared for both types of blends, however those exhibiting the best performance were chosen among them. All hybrid photoactive layers were subsequently deposited by spin-coating the blend solutions at 1000 rpm. In the case of PCDTBT:$PC_{71}BM$ based devices as electron transport layer was utilized the solution processed titanium sub oxide (TiO_x). The TiO_x interlayer was dissolved in methanol (1:200) and then spin-coated to a thickness of approximately 10 nm (6000 rpm, 40 s) in air[83]. The sample was heated at 80 °C for 1 min in air.

Lastly, 100 nm of Al was deposited through a shadow mask by thermal evaporation on the devices through a shadow mask to define an active area of 4 mm^2 for each device. The P3HT:PCBM based devices were post-annealed at 160°C for 15 min in a glove box under nitrogen atmosphere. The performances of the devices were measured at room temperature with an Air Mass 1.5 Global (A.M. 1.5 G) solar simulator at an intensity of 100 mW cm^{-2}. A reference monocrystalline silicon solar cell from Newport Corporation was used to calibrate the light intensity. All measurements were made in air immediately after device fabrication without any encapsulation process. The external quantum efficiency measurements were conducted immediately after device fabrication

in ambient conditions using an integrated system (Enlitech, Taiwan) and a lock-in amplifier with a current preamplifier under short-circuit conditions. The light spectrum was calibrated using a monocrystalline Silicon photodetector of known spectral response. The OPV devices were measured using a Xe lamp passing through a monochromator and an optical chopper at low frequencies (~200Hz) in order to maximize the sound/noise (S/N) ratio.

Photoluminescence measurements

For the PL experiments the devices were placed into a vacuum chamber with optical access. For sample excitation a He–Cd CW laser operating at a wavelength of 325 nm, with 35 mW power is used. The PL spectra were measured at room temperature and resolved by using a UV grating and a sensitive, calibrated liquid nitrogen cooled CCD camera. For the PL decay experiments the sample were initially (t<0s) illuminated (AM1.5 solar irradiation, 100mW/cm^2) under vacuum. For t>0s the sample was concurrently exposed to light and air. This led to a continuing decay of the PL that is monitored at certain time intervals.

Laser Induced Fluorescence (LIF) experiments

For the LIF experiments the devices were unencapsulated and exposed to ambient air. They were placed on a X-Y stage. For sample excitation, a Spectron, pulsed, nanosecond, Q-switched, Nd:YAG laser, operating at its second harmonic of 532 nm is used. The duration of every pulse is about 10 ns and the energy that was used for the excitation of the devices is ~ 40 μJ (fluence 0,4 mJ/cm^2). The fluorescence measurements were performed at room temperature and resolved by using an Andor Technology Mechelle 5000 spectrograph that is connected with an Andor iStar 734 Series, time resolved, cooled and Intensified Charge Coupled Device (ICCD). For the fluorescence decay experiments, the samples were initially (t<0s) illuminated (AM 1.5 solar irradiation, 100mW/cm^2), exposed to ambient air. For t>0s the samples that were used for the study of the fluorescence decay under illumination were concurrently exposed to light and air. The decay is monitored at certain time intervals. For the samples that were stored in dark, the decay of the fluorescence was also monitored at certain time intervals.

Fourier transform infrared spectroscopy (FT-IR)

FTIR measurements were carried out by means of a Jasco FT/IR 470 Plus interferometer (Italy) equipped with an IRTRON IRT-30 microscope. Each spectrum was acquired in the transmittance mode by executing 300 scans at 8 cm^{-1} resolution.

5.3. Results and discussion

Figure 5.3 displays the illuminated current voltage (J-V) characteristics of the reference and Al NPs doped optimized photovoltaic devices based on two different types of BHJ active layers, i.e. P3HT:PCBM (Figure 5.3a) and PCDTBT:PCBM (Figure 5.3c). The respective averaged photovoltaic characteristics are summarized in Table I.

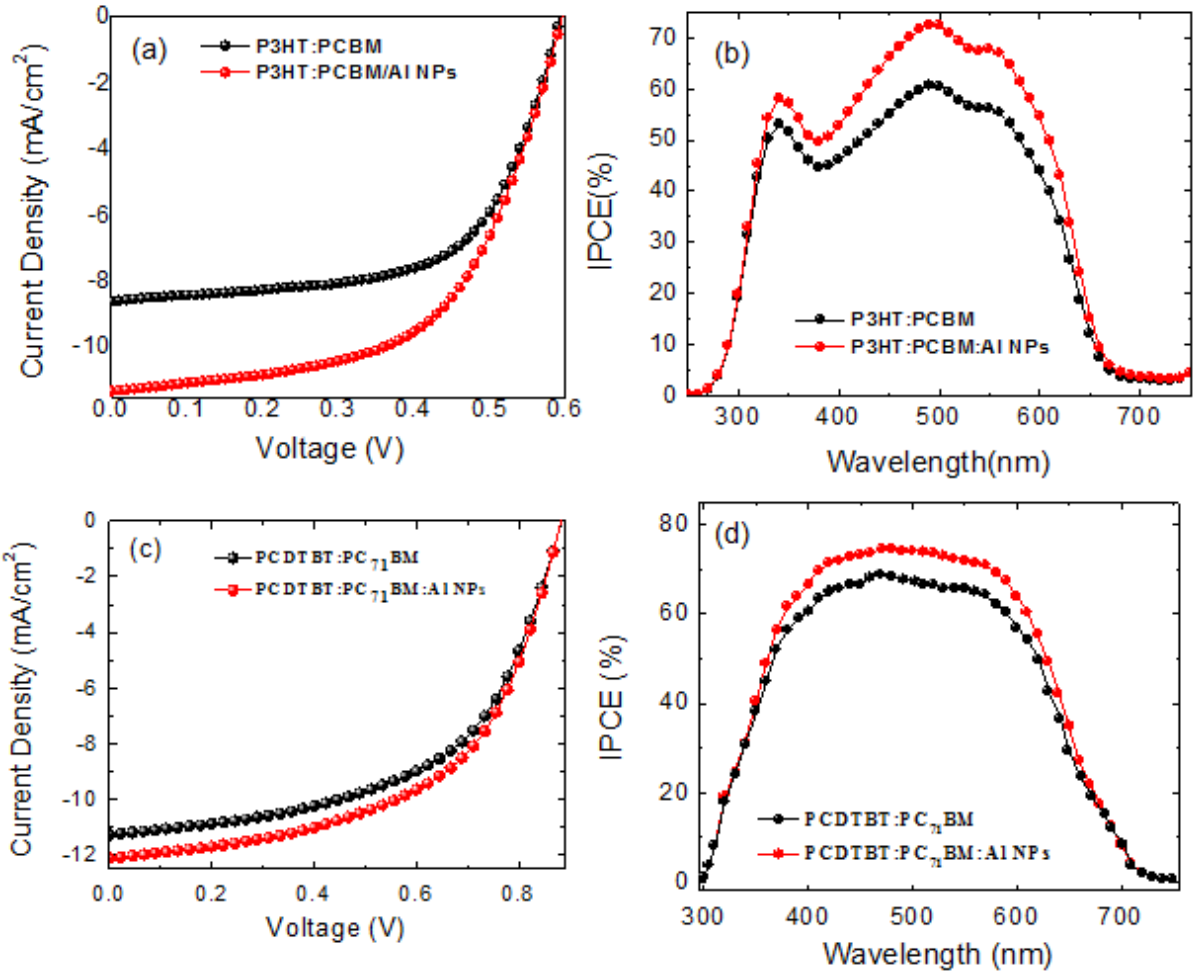

Figure 5.3: Plot of current density-voltage (J-V) characteristics of reference and Al NPs-doped OPV devices using the P3HT:PCBM (a) and PCDTBT:PC_{71}BM BHJ blends (c). The corresponding IPCE curves are plotted in Figures (b) and (d) respectively.

Table I: Electronic properties of the reference and Al NPs doped devices, defined in the text.

Active layer	J_{sc} (mA/cm²)	V_{oc} (V)	FF (%)	PCE (%)
P3HT:PCBM	8.60±0.16	0.60	61.17±0.41	3.16±0.08
P3HT:PCBM:Al NPs	11.32±0.21	0.60	60.22±0.53	4.09±0.11
PCDTBT:$PC_{71}BM$	11.29±0.14	0.88	55.13±0.33	5.48±0.10
PCDTBT:$PC_{71}BM$:Al NPs	12.13±0.23	0.88	56.21±0.45	6.00±0.16

In both cases the incorporation of Al NPs into the active layer induces a significant improvement in the device short-circuit current (J_{SC}), whereas the open-circuit voltage (V_{OC}) and fill factor (FF) remains almost constant. As a result the respective PCEs are increased by 29.6 % and by 9.5 % respectively. We have previously reported that the improved performance of Al NPs doped P3HT:PCBM blend can be attributed to multiple light scattering effects from the large-diameter Al NPs. It has also been reported that the incorporation of Au NPs as well enhances the performance of the photovoltaic[5]. This enhancement is mainly attributed to LSPR effects[5]. The observed enhancement in the high-efficiency PCDTBT:PCBM BHJ system as well, suggests that doping with metallic NPs is a universal and efficient way to enhance the PCE of BHJ OPVs. Following the fabrication and initial measurement of photovoltaic characteristics, the stability of the devices against degradation is measured via performing successive J-V recordings. In order to simulate outdoor conditions, the degradation experiments were performed with the devices being unencapsulated and exposed to ambient air during operation. Results are presented for two different measurement procedures related to sample storage conditions among measurements. In particular, between two successive J-V recordings, devices were either stored in the dark or were continuously illuminated in the open circuit mode. Figures 5.4a and b presents the evolution of the respective normalized PCEs (aging curves) over exposure time for the reference and Al NPs-doped devices following continuous operation under illumination.

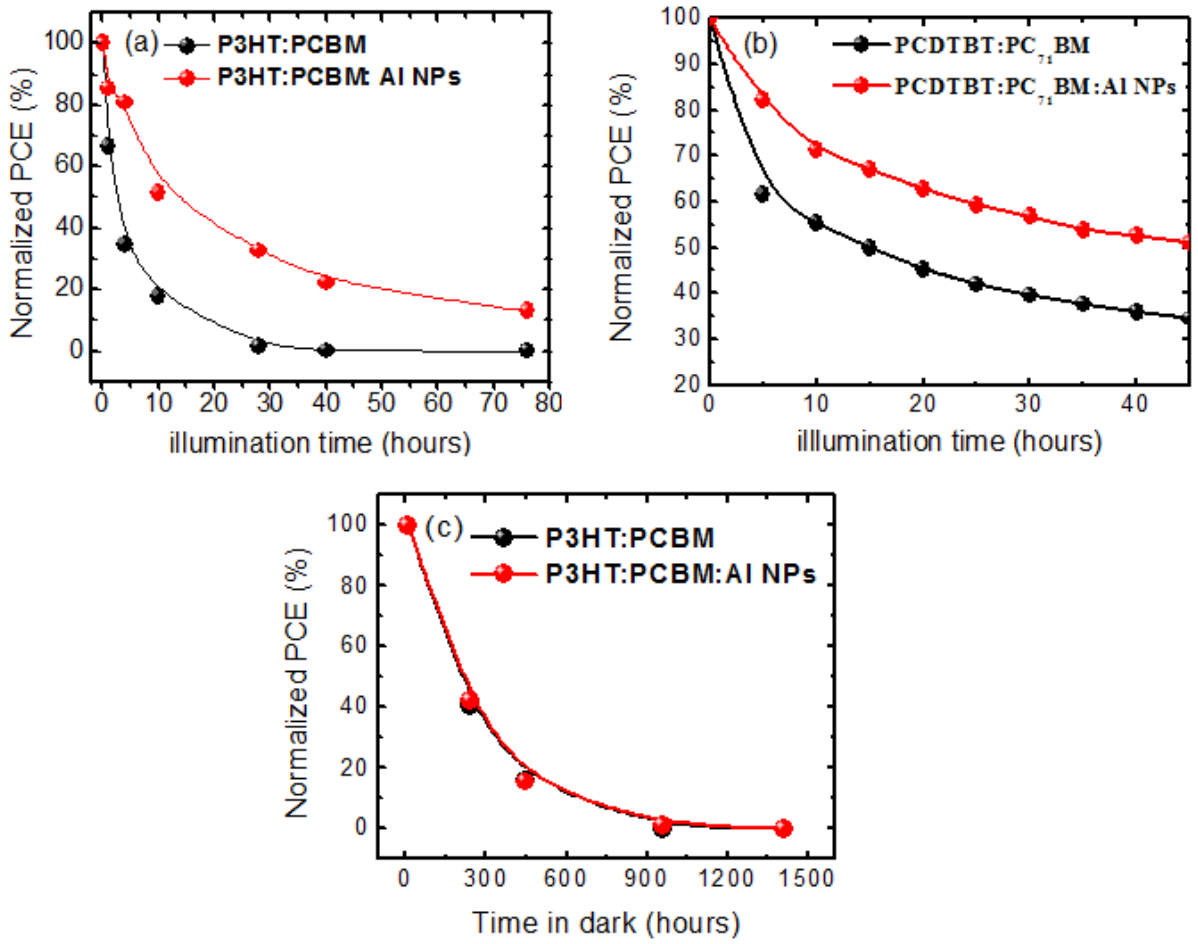

Figure 5.4: Normalized PCE values vs. illumination time for the reference and Al NPs-doped OPV devices using the P3HT:PCBM (a) and PCDTBT:$PC_{71}BM$ BHJ blends (b). The respective PCE dependence on dark storage time for the P3HT:PCBM based devices is shown in Figure (c).

For each data point of the curves, a complete J–V characteristic was recorded and the normalized, J_{sc}, FF, V_{oc} and PCE values were subsequently calculated. It is clear that for both BHJ systems PCE can be better preserved due to the presence of metallic NPs. The effect on PCE of the devices is more visible in the case of Al nanoparticles as it is shown in figure 5.5. By the incorporation of Au NPs the lifetime of the photovoltaic device was increased by a factor of 2, while the lifetime of Al doped device was increased by a factor of 5[81]. This effect may be attributed to the higher reactivity of Al to oxygen compared to Au[81]. This hypothesis was investigated with FT-IR analysis and the results are presented later in this section. On this purpose, this study focused mainly on Al doped devices.

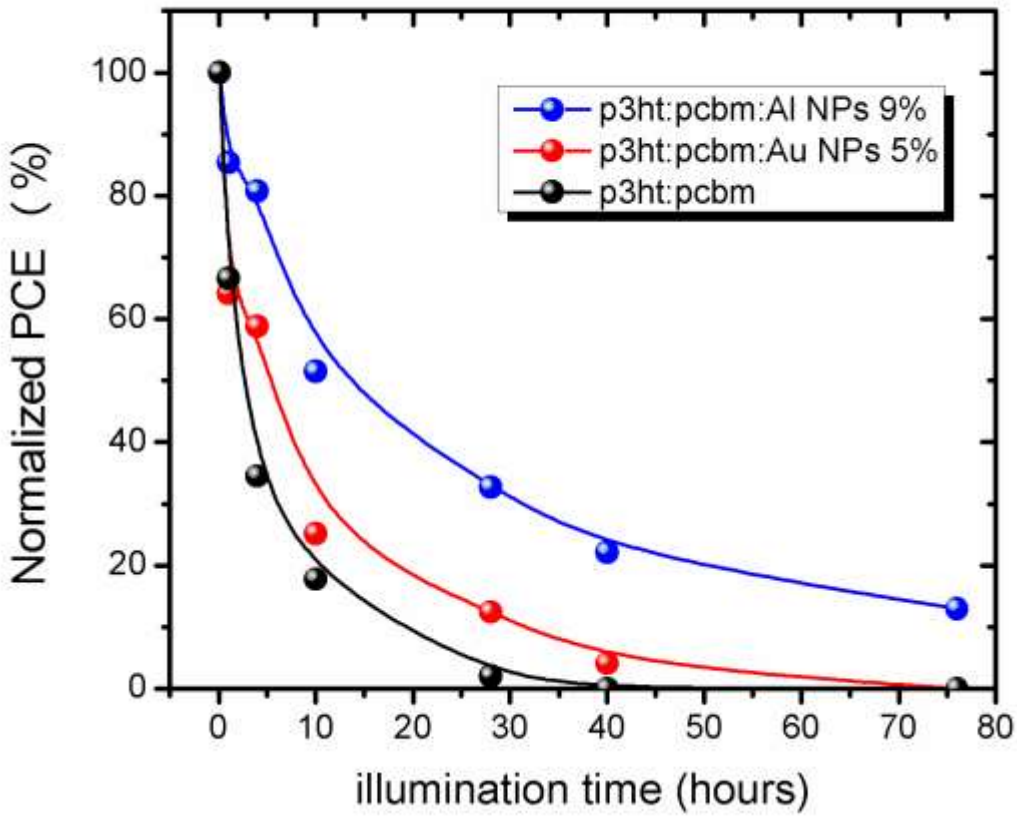

Figure 5.5: Normalized PCE values vs. illumination time for the reference and NPs-doped OPV devices using the P3HT:PCBM BHJ blend.

Indeed, for the P3HT:PCBM and P3HT:PCBM:Al NPs active layers 2.5 and 13.5 hours of continuous illumination are required for a 50% reduction of PCE with respect to its initial value. The situation is similar for the PCDTBT:PCBM and PCDTBT:PCBM:Al NPs systems required 14.5 and ~45 hours respectively for the same PCE reduction to be

attained. The above results indicate that incorporation of Al NPs into the BHJ active layer significantly mitigates performance deterioration due to photo-degradation. On the contrary, as indicated in Figure 5.4c, there is practically no difference in the corresponding PCE evolutions between the reference and Al NPs doped P3HT:PCBM-based devices stored in dark. Similar observations were made for the device hosting a PCDTBT:$PC_{71}BM$ active layer (not shown). It can be concluded that the observed stability enhancement phenomenon takes place only under illumination, suggesting that Al NPs strongly affect the OPVs photodegradation pathways[84] while their effect is not related to ageing mechanisms occurring in the dark[85].

In order to probe the underlying mechanism behind the observed effect of Al NPs against photodegradation, we have proceeded to optical spectroscopy studies of the pristine and doped P3HT:PCBM blends. The reason is that it is the best characterized BHJ system, but more importantly it is highly reproducible, thus enables a quantitative spectroscopic study. In a first step, we have considered, based on the above results, that the presence of Al NPs may hinder the process behind photoinduced oxidation of the conjugated polymer component in the blend[62,63]. As presented in Scheme 2, during photo-oxidation of semiconducting polymers, singlet oxygen, formed via energy transfer from the polymer triplet exciton, reacts with the polymer to generate exciton traps (paths 6a and b in Scheme 2).

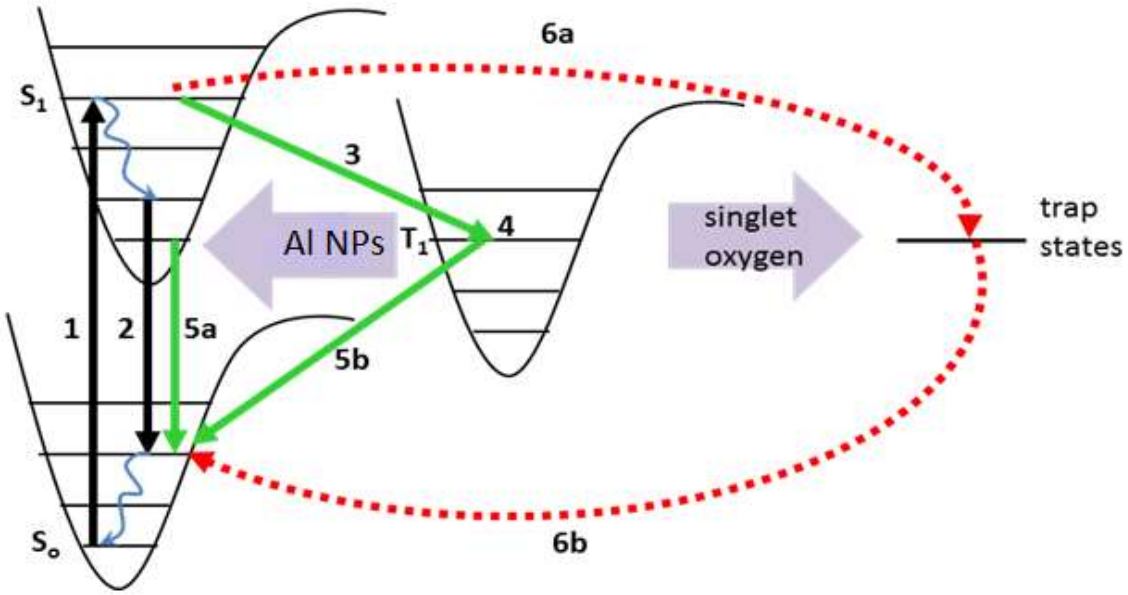

Scheme 2: Schematic of the photo-oxidation process in polymer: Al NPs active layer. Energy from the polymer triplet excitons excites singlet oxygen, which reacts with the polymer chains to form exciton trap states. The Al NPs embedded into the blend act as quenchers of the triplet excitons and in this way the photooxidation process can be impeded. 1: Absorption; 2: Luminescence 3: System Intercrossing; 4: Triplet State; 5a: Fluorescence; 5b: Triplet quenching; 6a, 6b: Exciton recombination via trap states. This process is limited in the presence of a triplet quencher.

Such traps are topological defects comprised of carbonyl groups formed on the ends of polymer chains and provide an additional nonradiative channel for the polymer singlet excitons. As a result, quenching of polymer luminescence is induced. In Donor:Acceptor (D:A) blends, the charge transfer from polymer to fullerene is the dominant process and therefore it partially prevents intersystem crossing to a triplet state. Under certain conditions, the formation of triplets in polymer:fullerene blends is also possible as it depends on the relative energy positions of polymer triplet excitons and the fullerene LUMO level[53]. Formed triplet excitons located on the polymer can then nonradiatively relax to the ground state. Additional reactions emerge upon introduction of molecular oxygen, which has a triplet ground state configuration ($^3O_2$). The polymer triplet excitons can undergo energy transfer to the triplet oxygen to generate excited singlet oxygen ($^1O_2$*). It can be concluded that the mechanisms described in Scheme 2 are valid and present in polymer:fullerene blends as well. In the present case Al NPs may play the role of a stabilizer that blocks the action of oxygen. In particular, as shown in Scheme 2, we postulate that the triplet excitons may be quenched as a result of the overlap of their energy levels with the plasmon resonance of the embedded Al NPs (paths 3,4,5b in Scheme 2)[86].

To investigate this possibility, PL decay measurements, which are a proper mean to quantify singlet quenching in P3HT under oxygen exposure, were performed. Figure 5.6 presents the results for the reference compared to the Al NPs-doped blend. These measurements correspond to the evolution of the first emission peak values, at 635 nm, following laser excitation at 325 nm.

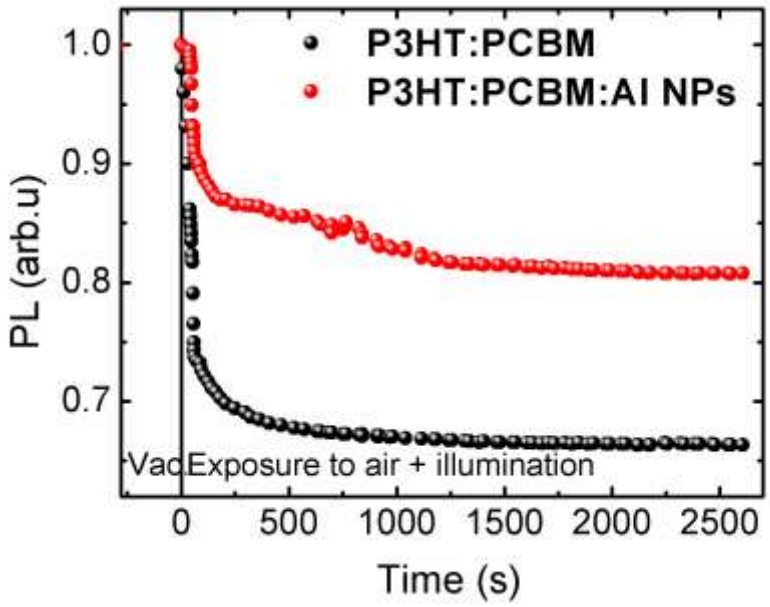

Figure 5.6: Photoluminescence decay of reference (black spheres) and Al NPs doped (red spheres) P3HT:PCBM based devices

It is clear that the addition of NPs into the blend significantly retards its PL intensity decay rate. Indeed, the absorption spectrum of Al NPs in ethanol (Figure 5.1) comprises a characteristic broad peak corresponding to the NPs' plasmon resonance. This peak centers at ~340 nm, however it is expected to be substantially red-shifted when the NPs are embedded into the higher-refractive index, compared to ethanol, polymer matrix[87]. Such red shift combined with the broadband nature of NPs' absorption peak may give rise to partial overlap with the triplet excitons band lying in the range [500-800] nm for both polymer donor systems used in this study[88]. Considering that the NPs resonance has an excitation lifetime of a few picoseconds, the donor-acceptor interaction between the comparatively long-lived triplet excitons of P3HT and the Al NPs will result in a strong quenching of the triplet state and, thus, the photo-oxidation rate. Alternatively, the photoexcited excitons are highly mobile along the conjugated polymer backbone and may hop between chains towards lowest-energy areas of the film. It is possible that the Al NPs dispersed in the polymer blend will give rise to variations in the local energy environment of the triplet excitons, attracting them towards Al NPs, where the triplet exciton-Al NPs interaction can easily take place[62]. Specifically, as the size of particles decreases to the nanometer scale, the surface area of the particles increases dramatically, and the NPs act as an effective scavenger of the polymer triplet state[56].

In order to further study the degradation process, fluorescence experiments were additionally performed. For this purpose reference and Al NPs doped devices were submitted to long-term degradation process in air and the decay of their fluorescence signal was recorded both under dark storage and during illumination (three pairs of samples for each case). In this way it was possible to discriminate the aging processes related to light exposure from those due to ambient environment only (air). Moreover, we were able to examine the contribution of the Al NPs to the photovoltaic effect and the stability of the device. The collected fluorescence spectra are presented in Figure 5.7, while Figure 5.8 compares the normalize fluorescence intensity, with the data from the Au-doped devices included (the fluorescence spectra are not shown), calculated using the peak values of such spectra, at 635 nm, following laser excitation at 532 nm, as a function of the dark storage and illumination times respectively.

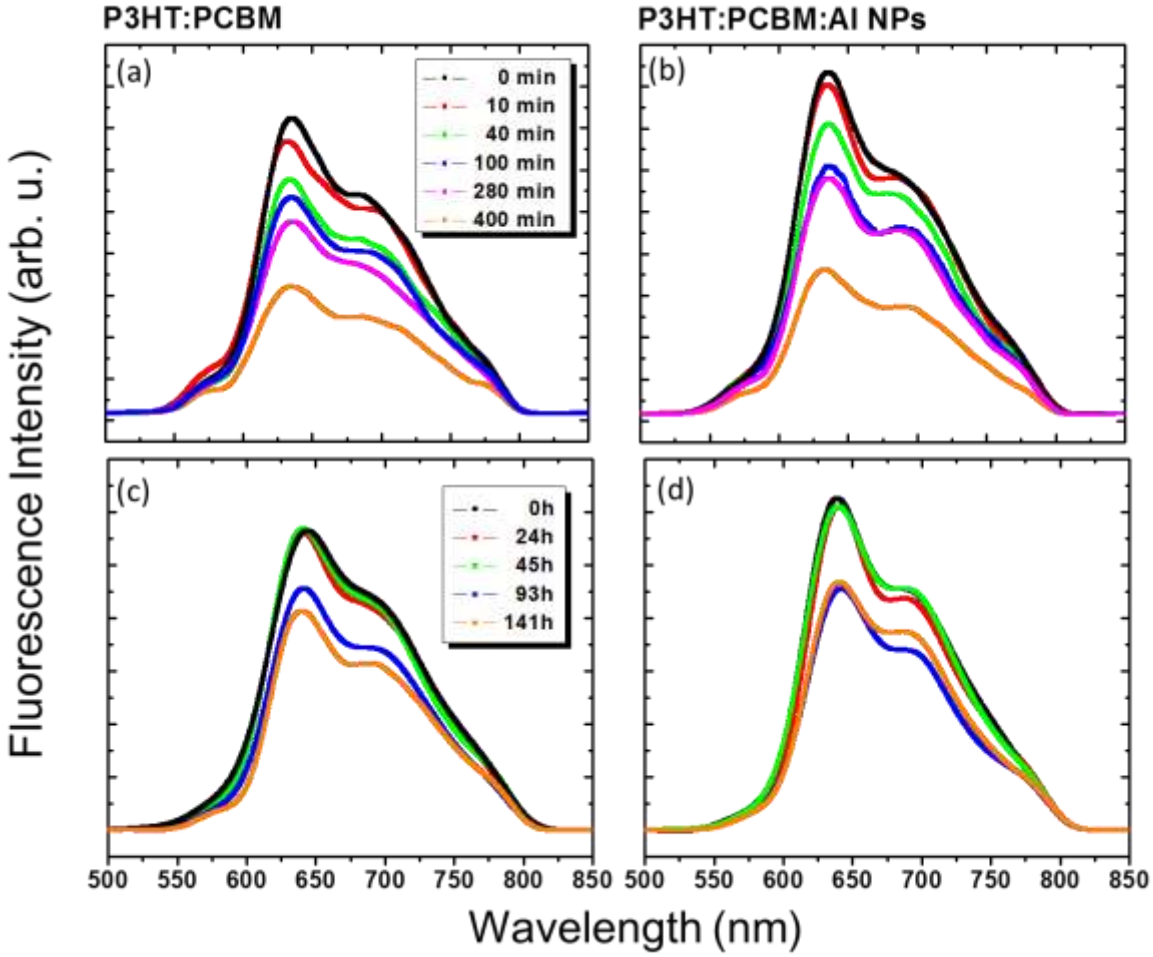

Figure 5.7: Laser induced Fluorescence spectra of: reference (a) and Al NPs-doped devices (b) after illumination at certain time intervals shown in the inset, reference (c) and Al NPs-doped (d) devices stored in dark. Excitation wavelength at 532 nm, Nd:YAG ns laser.

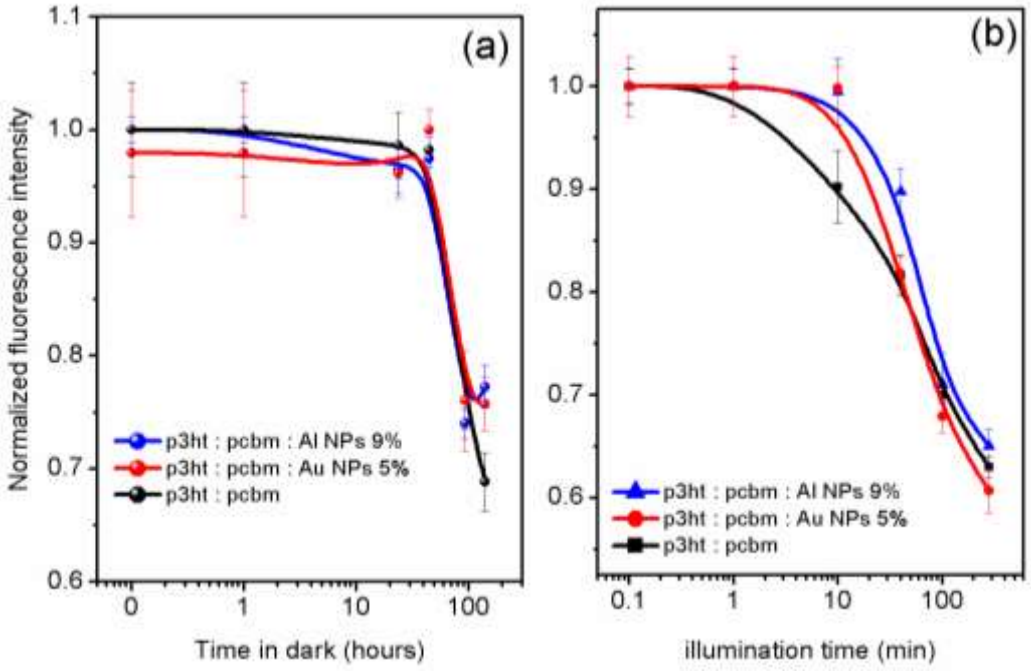

Figure 5.8: (a) Normalized fluorescence decay of reference and NPs doped devices stored in the dark. (b) Normalized fluorescence decay of reference and NPs doped devices that were illuminated at certain time intervals. Excitation wavelength at 532 nm, Nd:YAG ns laser. The normalized values corresponding to the peak emission wavelength at 635 nm are plotted.

As can be seen in Figure 5.8b, the fluorescence signal of the reference device degrades rapidly upon illumination, following a first order exponential decay. On the contrary, the NPs based device is more stable under illumination, especially Al NPs device, in the first 10 min of illumination. In this case the fluorescence decay is well fitted by a sigmoidal curve, indicating the fluorescence decay mitigation effect. On the contrary, there is no evidence of any mitigation effect when the same blends are monitored, while the samples were stored in dark in ambient air (Figure 5.8a). These results are in accordance with the PCE degradation experiments presented in Figure 5.4c and further confirm the NPs mediated preservation effect of the polymer optical properties, evident only under prolonged illumination.

The different dynamics observed for the fluorescence decay signal between light and dark conditions imply the presence of two separate degradation pathways affecting the BHJ system. Our results above suggest that incorporation of Al NPs affects only the pathway under light exposure. To further explore these phenomena, FTIR spectroscopy

is used providing an insight on the chemical bonding changes taking place under illumination or dark storage of the reference and Al NPs doped devices.

As shown in Figure 5.9, the FTIR spectra of the reference and Al NPs devices in its pristine state exhibit remarkable differences. In particular, the reference device shows a broad band at 1530 cm^{-1}, being the convolution of the two resonant quinoidal and benzoic structures of the thiophene ring in PEDOT, which are equally represented in the as-deposited film[89]. This broad band also includes the C=C stretching of P3HT aromatic ring positioned at 1515 cm^{-1}. In the pristine state of the Al NPs doped sample, however, two sharp and distinct bands are evidenced at 1515 cm^{-1} and 1548 cm^{-1} respectively. This may be an indication that the Al NPs interfacing the PEDOT:PSS buffer layer could modify the balance between the two resonant structures of PEDOT and consequently its packing structure. Furthermore, the band at (1292-1314) cm^{-1} in the reference sample red shifts towards 1263 cm^{-1} in the Al NPs doped sample. This region is generally associated to the acyl- or phenol- C-O stretching corresponding to the ethylene-dioxy group in PEDOT. The red shift is a further hint of a structural rearrangement occurring in the buffer layer due to Al NPs doping. Finally, in the reference sample the following PSS characteristic bands are visible: asymmetric S-O stretching vibrations at 1120 cm^{-1} and S=O stretching due to SO_3^- band at 1388 cm^{-1}. These bands are red shifted towards 1059 cm^{-1} and 1330 cm^{-1} respectively, in the Al NPs doped system. The latter band is a shoulder convolved to the stronger ethylene-dioxy signal. The above observations comply with partial Al NPs diffusion at the active layer/buffer layer interface, causing modification of the PEDOT:PSS chain motion.

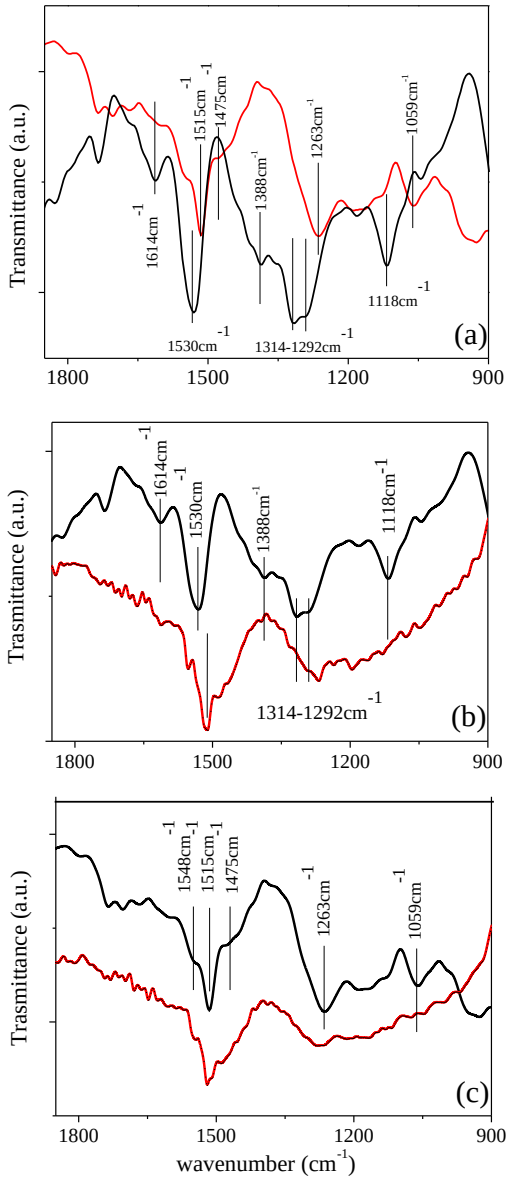

Figure 5.9: (a) FTIR measurements of pristine samples; Reference sample: black line; AlNPs sample: red line. FTIR measurements of reference (b) and (c) Al-doped devices; black line: pristine state, red line: dark storage state. The vibrational modes corresponding to the wavenumbers labeled in the Figure, are reported in Table 2.

Figures 5.9b and 5.9c presents the FTIR data for reference and NPs based layers following dark storage for three weeks in air. A general observation is that the characteristic bands intensities decrease after storage, indicating degradation of the buffer layer. For the reference system, the bands showed the most remarkable modifications are discussed in the following. First, there is a red shift of the C=C

stretching thiophene ring vibration from 1530 cm^{-1} to 1515 cm^{-1}, the final value almost approaching the characteristic band of pure P3HT, while a less intense band at 1548 cm^{-1} is detected after dark storage. This is an indication that exposure to ambient conditions has modified the balance between the resonant quinoidal and benzoic structures of the thiophene ring in PEDOT, characterizing the as-deposited films. As a result, the (less conductive) benzoic contribution of PEDOT becomes dominant over the quinoidal (conductive) one. An additional spectrum modification is related to the band including the 1292 and 1314 cm^{-1} modes red shifting towards 1270 cm^{-1}. This region is associated to the ethylene-dioxy group in PEDOT and the red shift observed implies structural rearrangement occurring during ambient storage. In addition, the PSS characteristic bands at 1118 cm^{-1} (asymmetric S-O stretching vibrations) and at 1388 cm^{-1} (S=O stretching due to SO_3^-) are strongly reduced, indicating that PSS modification occurs upon dark storage, possibly due to ambient moisture (PSS is highly soluble in water). Such degradation may affect the bond between SOH_3 group and the insulating chains of PSS, inducing a reduced interaction between PEDOT and PSS.

Similar to the reference sample, sample the band intensities of the FTIR spectrum of Al NPs doped system decreased after storage (Figure 5.9c) indicating degradation of both the structure of the PEDOT:PSS and P3HT polymeric components. However, contrary to the reference system, the characteristic peaks of PEDOT and P3HT were not shifted. The only remarkable effect is the suppression of the PSS characteristic bands at 1059 cm^{-1} and at 1263 cm^{-1}, suggesting that the contribution to buffer layer degradation is limited to its hygroscopic component as a consequence of exposure to ambient moisture.

The comparison of the FTIR spectra of the reference sample in its pristine vs illuminated states, presented in Figure 5.10, does not evidence any shift of the buffer layer vibrational bands, indicating that the PEDOT:PSS layer remains stable upon light exposure. However, there is a prominent decrease of the 1530 cm^{-1} peak intensity, attributed to both PEDOT and P3HT. However, since no variation was observed for the rest of PEDOT and PSS vibrational modes, we may assume that the 1530 cm^{-1} intensity loss is a fingerprint of P3HT photo-oxidation, as previously reported in the literature[90]. Further information of the BHJ degradation under light exposure can also be deduced from the strong reduction of the band at 1190 cm^{-1}, related to C-C-O stretching in PCBM.

This suggests that illumination may favour diffusion of the water molecules into the BHJ and PCBM esters hydrolysis spontaneously occurs[52]. This is also confirmed by the appearance of the broad band at 3550 cm^{-1} (inset of Figure 5.10a), which is the spectral marker of the stretching mode of (OH) groups (being alcohol the secondary product of the ester hydrolysis). On the contrary, the FTIR bands of the NPs doped system remains unchanged after prolonged illumination. Only a band intensity decrease was observed, indicating a general degradation of the structure of the PEDOT:PSS and P3HT polymeric components. The above data suggest that no structural modifications occur in the Al NPs doped system upon prolonged illumination.

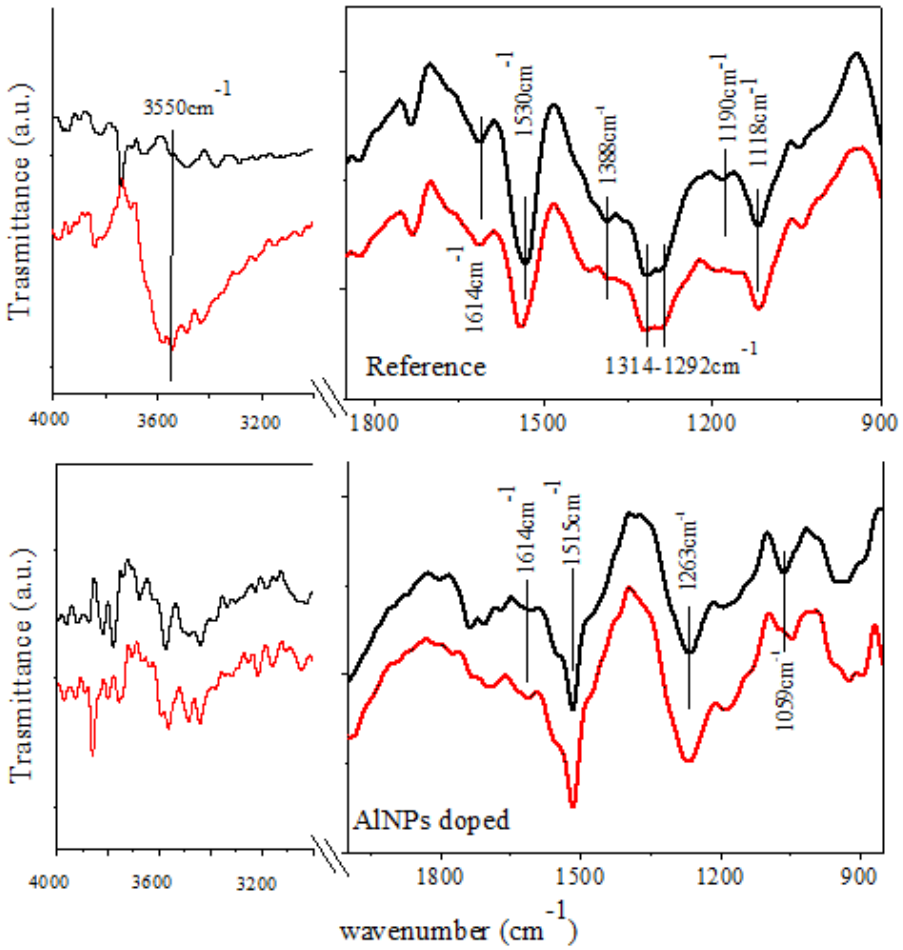

Figure 5.10: FTIR measurements of reference (top) and Al-doped devices (bottom); black line: pristine state, red line: illuminated state. The vibrational modes corresponding to the wavenumbers labelled in the Figure, are reported in Table 2.

Table II: Vibrational modes corresponding to the wavenumbers labeled in Figures 5.9 and 5.10

Wavenumber (cm^{-1})	Functional group
1059	$-SO_3^-$ sym. stretch.
1118	S-O asym. stretch.
1190	C-O stretch. in esters
1263	Red shift of 1292 vibration
1292-1314	C-O stretch. Ethilendioxy group
1388	S=O stretch.
1475	Red shift of 1515
1515	C=C sym. Stretch. in aromatic
1530-1548	Tiophene stretch.
1614	C=C asym. Stretch. in aromatic
3550	O-H stretch.

Summarizing the FTIR results, we can state that the following aging processes are evidenced under dark storage of the reference sample: PEDOT degradation (favouring of a less conductive structure) and PSS modification. The former process is inhibited when Al NPs are introduced in the BHJ and only PSS modification, related to its hygroscopic nature, persist. This effect may be due to the presence of some Al NPs in contact with the hole transporting layer that may hinder the PEDOT:PSS chain motions leading to an effective increase of the conformational stability. It should be mentioned here that the identical dark lifetime degradation measured for both types of cells, namely reference and Al NPs doped, indicate that the dark IV characteristics may not be sensitive to such changes in the PEDOT:PSS structure. This is in accordance to the literature, stating that the dark current is typically not a figure of merit of solar cell devices[91]. Conversely, all aging processes evidenced in the reference sample under illumination, are inhibited upon incorporation of Al NPs into the BHJ blend.

The FTIR results complemented with the PL and fluorescence studies presented above provide us with important information on the different degradation pathways occurring upon illumination. In particular, our results show that P3HT photo-oxidation, which is the primary pathway, is significantly mitigated in the Al NPs doped OPV cells possibly due to the reason that Al NPs function as triplet quenchers (Scheme 2). Besides this, a second degradation pathway present upon illumination is related to PCBM hydrolysis,

which gives rise to the creation of trap states acting as fluorescence quenchers and thus influence exciton generation. We postulate that solar illumination could mediate the formation of an aluminium-oxide (Al_2O_3) coating on the NPs surface. In particular, due to exposure to air and moisture conditions, water molecules diffusing in the BHJ will react under illumination with the NPs surface leading to Al_2O_3 corrosion, which is well known as a spontaneous reaction process[92]. Such process is facilitated by the absence of any surfactant coating on the Al NPs surface[93,94], since the NPs used here were produced by a physical synthetic method. As a result of this process, the availability of water molecules promoting PCBM hydrolysis is limited. Finally the third aging process identified by FTIR analysis is associated to a degradation of the PEDOT:PSS layer. This aging pathway is always present upon exposure to air, while the presence of Al NPs at the active layer/buffer layer interface partially influences the PEDOT:PSS chain motion.

5.4. Conclusions

This work focused on a main concern of organic photovoltaic (OPV) devices that is photoinduced stability, aiming to shed light on the degradation mechanisms during certain time intervals of solar exposure in ambient conditions. We have reported on a remarkable enhancement of OPV devices lifetime upon incorporation of Al NPs into the BHJ active layer. The stability enhancement of bulk heterojunction OPV blends incorporating surfactant free metallic nanoparticles (NPs) into the photoactive layer was investigated by Laser Induced Fluorescence (LIF), Photoluminescence (PL), Fourier transform infrared (FTIR) spectroscopy complemented by device degradation electrical measurements. These measurements revealed the mitigation of two different photodegradation pathways attributed to the presence of Al NPs. Firstly, NPs incorporation blocks the polymer donor photooxidation via oxygen-assisted formation of triplet excitons, possibly due the overlap of such excitonic levels with the plasmon resonance of the embedded Al NPs. Secondly, it inhibits the PCBM hydrolysis, possibly due to the light mediated corrosive reaction with water molecules leading to Al_2O_3 surface layer formation. This work proposes the application of Al NPs doping as an efficient way to enhance the lifetime of other types of polymer devices as well, including light emitting diodes, detectors and sensors.

Chapter 6: Laser synthesis of 2D Nanosheets (NS)-Nanoparticles (NPs) hybrids for ternary plasmonic organic solar cells

6.1. Introduction

A novel top-down and universal optical technique for the effective decoration of two-dimensional (2D) nanosheets (NS), of graphene oxide (GO), boron nitride (BN) and tungsten disulfide (WS_2), with noble metallic nanoparticles (NPs) is reported. The NS-NPs assemblies were formed under ambient conditions, via a facile, rapid and solution compatible laser assisted process in the presence of a metallic precursor. It is shown that a few seconds of irradiation is sufficient to decorate the NS lattice, while the NPs density can be readily controlled upon variation of the irradiation time. It is found that the laser induced anchoring of Au NPs onto NS basal plane and edges resulted in enhanced light harvesting that is potentially useful for energy conversion and storage applications. To demonstrate the potential of the approach for practical applications, the incorporation of WS_2-Au NPs assemblies into the photoactive layer of ternary bulk heterojunction (BHJ) organic photovoltaic (OPV) cells is realized. The power conversion efficiency (PCE) of the binary device consisting of a PCDTBT:$PC_{71}BM$ blend as the donor-acceptor pair was 5.6%, while after the employment of WS_2-Au NPs the efficiency enhancement of the ternary device was approximately 13% reaching a total PCE of 6.3%. The facile, rapid and room temperature nature of the photo-induced method proposed here provides unique opportunities for the cost-effective synthesis of bulk amounts of NS-NPs assemblies in solution for many optoelectronic applications.

6.2. Experimental

Reagents and materials

The pristine NS were purchased from Graphene Supermarket in dispersions (GO=500 mg L^{-1}, BN=5.4 mg L^{-1}, WS_2=26 mg L^{-1}). The BN flake lateral size was 50-200 nm consisting of 1 to 5 monolayers. The WS_2 flake lateral size was 50-150 nm and they were consisted of 1 to 4 monolayers. The size of GO flakes was 0.3-0.7 μm consisting of at least 80% monolayers. The chloroauric acid ($HAuCl_4$, ethanol as solvent) and silver nitrate ($AgNO_3$, distilled water as solvent) salts were supplied from Sigma Aldrich.

Laser irradiation process

Mixed dispersions of NS with $HAuCl_4$ in ethanol or $AgNO_3$ in water were placed into a quartz cuvette and were subjected to illumination by excimer laser UV pulses (wavelength of 248 nm, 20 ns pulse duration). A couple of irises secured the formation of a spatially uniform laser beam spot that illuminated the solution. During illumination, the irradiated dispersions were continuously agitated via a magnetic stirrer. A schematic representation of the experimental process is depicted in Figure 6.1a. To investigate the process of the laser induced NPs anchoring onto NS, the irradiation power, the number of pulses and the relative concentration of NS over the salt precursor were varied.

Materials characterization

Characterization was carried out after purification by three centrifugation/decantation and re-dispersion steps to ensure that any non-covalently attached NPs were removed. In particular, the morphology of pristine and NPs' decorated NS was characterized with High Resolution Transmission Electron Microscopy (HRTEM), using a JEOL-2100 LaB_6 ultra-high-resolution electron microscope. The UV-Vis absorption spectra of the initial and laser-irradiated solutions were obtained using a Perkin Elmer, LAMBDA 950 UV/VIS/NIR spectrophotometer. Raman spectroscopy is performed at room temperature using a Nicolet Almega XR Raman spectrometer equipped with a 470 nm

laser as an excitation source. For the preparation of the samples, the NS and NS-NPs assemblies were drop casted onto quartz substrates.

Devices fabrication and characterization

PCDTBT and $PC_{71}BM$, both purchased from Solaris Chem, were dissolved in 1,2-dichlorobenzene:chlorobenzene (3:1) (o-DCB:CB), with a 1:4 (4 mg:16 mg) ratio and stirred overnight at 70 °C. The resulting PCDTBT:$PC_{71}BM$ solutions were mixed with different amounts of WS_2 and WS_2-Au NS (1.0%, 1.5%, and 2.5% v/v) to obtain the final blends. The photovoltaic devices were fabricated onto 20 mm by 15 mm indium-tin-oxide (ITO) on glass substrates with a sheet resistance of ~20 Ω sq^{-1}. The impurities are removed from the ITO glass through a 3-step cleaning process (soap solution, acetone and isopropanol). WS_2 and WS_2-Au NS were also dissolved into o-DCB followed by utrasonication for 1 h. Following this cleaning process, the substrates were spin-casted with a poly (3,4-ethylenedioxythiophene):poly (styrene sulfonate) (PEDOT:PSS) layer at 6000 rpm for 60 s, obtaining a 30 nm hole transport layer. The films were baked for 20 min at 120 °C inside a nitrogen-filled glove box to dry any residual moisture. All photoactive layers (PCDTBT:$PC_{71}BM$ and PCDTBT:$PC_{71}BM$:WS_2 and PCDTBT:$PC_{71}BM$:WS_2:Au) were subsequently deposited on top of the PEDOT:PSS layer by spin-coating at 1000 rpm, until the thickness reached approximately 80 nm determined by cross-sectional SEM images. The cells were dried at 60 °C for 1 min and subsequently a 10 nm Ca interlayer and a 100 nm Al top electrode were deposited through a shadow mask by thermal evaporation to complete device architecture, creating an active area of 0.04 cm^2.

The optoelectronic performance of the solar cell devices were measured at room temperature with an Air Mass 1.5 Global (A.M. 1.5 G) solar simulator at an intensity of 100 mW cm^{-2} inside a glove box. Current–voltage (J–V) measurements were performed using an Agilent B1500A Semiconductor Device Analyzer. A reference monocrystaline silicon solar cell from Newport was used to calibrate the light intensity. The external quantum efficiency (EQE) measurements were conducted immediately after device fabrication and encapsulation method because of the sensitivity of Ca on air conditions.

The respective EQE spectra were monitored using a Xe lamp passing through a monochromator and an optical chopper at low frequencies (~200 Hz) in order to maximize the signal/noise (S/N) ratio.

6.3. Results and discussion

Synthesis of 2D NSs-NPs assemblies

The laser-induced reaction leading to NPs nucleation onto the 2D NS took place into a quartz cuvette, containing the initial NS dispersion into which the precursor molecules were dissolved. The efficiency of the process was unexpectedly high, as the final product was delivered via irradiation with a single laser pulse. In order to find out the optimum parameters for the NS decoration a series of different volume ratios of NS over precursor solution were investigated. The best results, as far as the uniformity of NS decoration and the stability of the final solutions against precipitation, were obtained for NS:precursor ratios of 1:1, 1:2 and 1:4 respectively, using two different laser fluences of 100 or 1000 $mJcm^{-2}$. It should be emphasized that the irradiated dispersions were stable, since no precipitation is observed even after months of storage in ambient conditions.

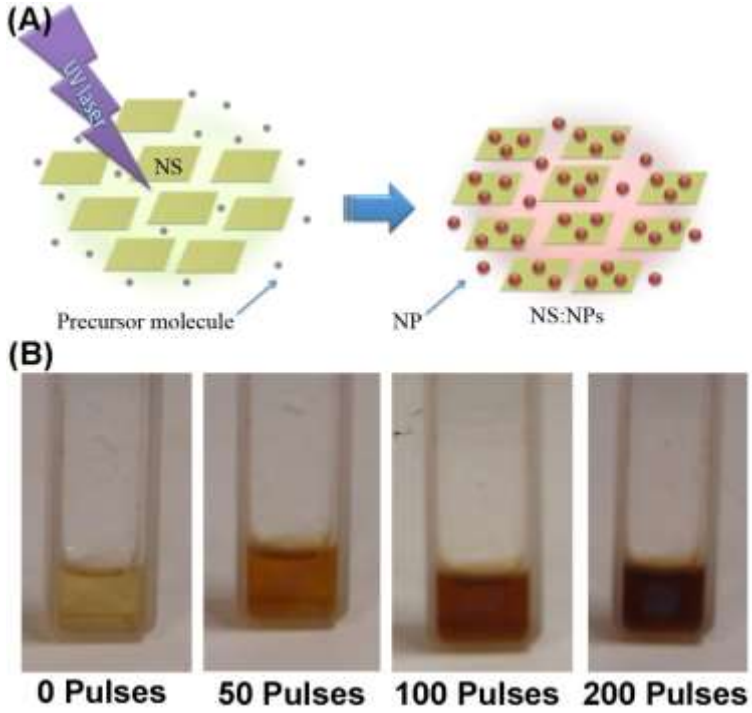

Figure 6.1: A) Schematic of the experimental process of laser-induced generation of NS:NPs assemblies; B) Pictures of the reference and laser treated GO-$HAuCl_4$ dispersions, irradiated with different numbers of 100mJcm^{-2} UV pulses.

In a first experiment we have irradiated GO NS in the presence of $HAuCl_4$ metallic precursor. As the GO NS surface was activated and decorated with Au NPs, upon irradiation with consecutive UV pulses, the coloration of the mixture was gradually turned from bright yellow to dark red (Figure 6.1b). The corresponding UV-vis spectra of GO-Au assemblies formed are presented in Figure 6.2a. As expected, the spectrum shows the appearance of a distinct peak at 545 nm, corresponding to the surface plasmon resonance (SPR)[95] of gold NPs. We postulate that the photo-reduction of the $HAuCl_4$ solution was the main source of NPs generation.

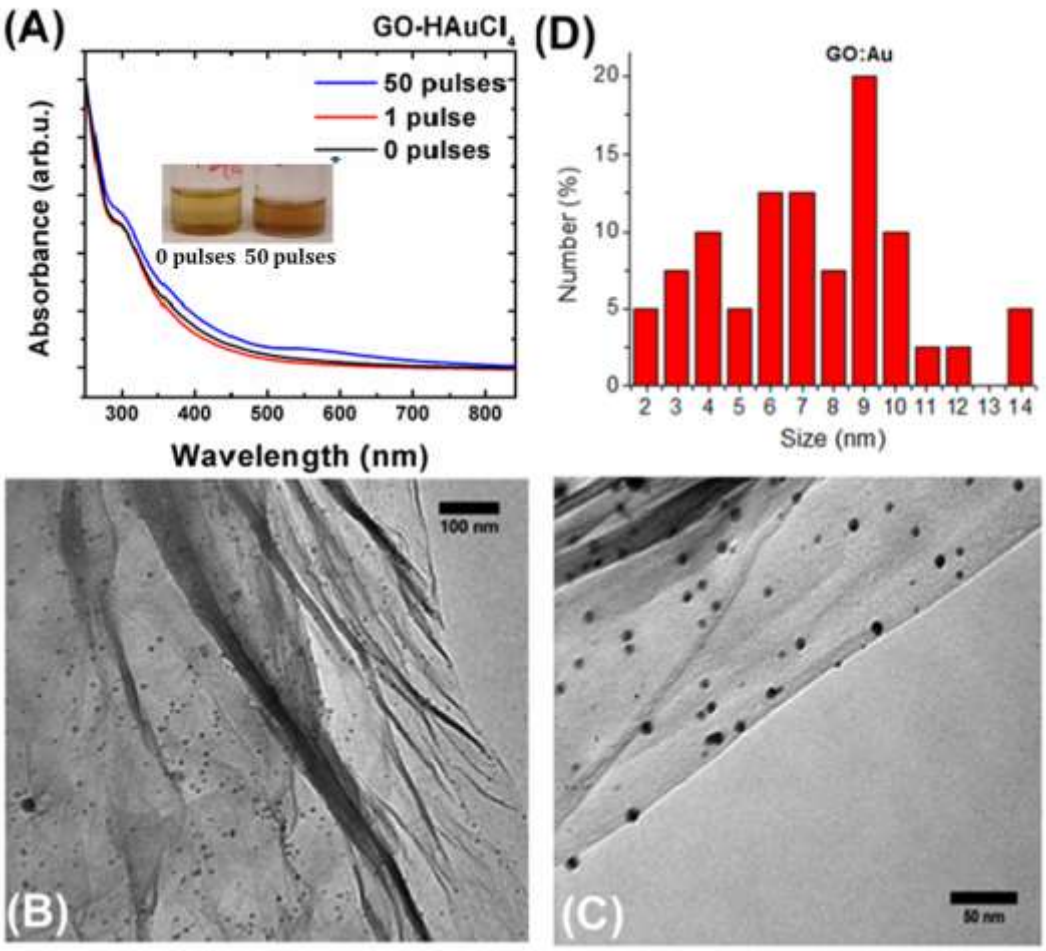

Figure 6.2: (A) UV-vis absorption spectra of pristine GO-$HAuCl_4$ dispersions in ethanol before (black line) and after irradiation with 50 UV laser pulses of 100mJcm^{-2}. The inset depicts an image of the respective dispersions; (B), (C): TEM images of the GO-Au assemblies after the illumination of the mixed solutions at ratio 2:1 with a single UV pulse and fluence of 100 mJ cm^{-2}; (D) Size distribution of the Au NPs grafted onto the GO NSs.

Similar results were obtained in the case of GO-Ag assemblies formed upon irradiation of GO-NS-$AgNO_3$ dispersions (Fig. 6.3). In this case as well, following an elevated number of pulses, a characteristic peak at ~400 nm appeared in the UV-vis spectrum of the irradiated dispersion, corresponding to the SPR of Ag NPs[96].

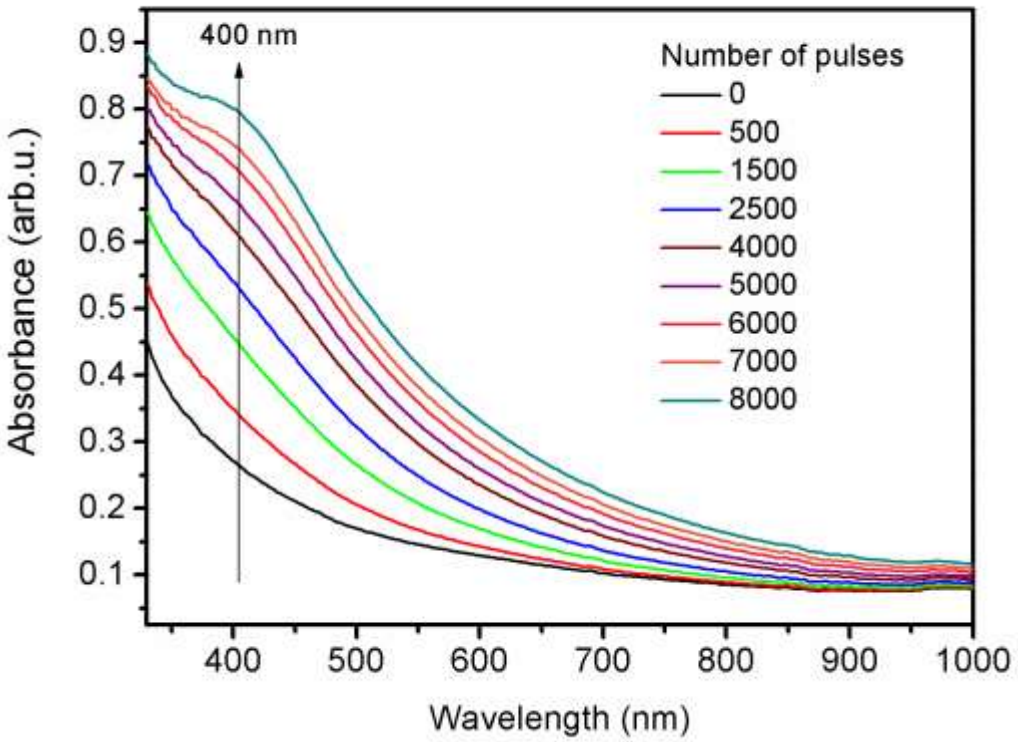

Figure 6.3: UV-vis absorption spectra of pristine GO-$AgNO_3$ dispersions in water, irradiated with different numbers of 100mJcm^{-2} UV pulses.

Further evidence that the NPs were successfully grafted onto GO NS was obtained by TEM imaging. Figures 6.2b, c shows typical TEM images of GO:Au assemblies formed using a single UV laser pulse of 100 mJ cm^{-2}. It is clear that NPs are uniformly distributed on the NS surface. The corresponding size distribution of the nucleated Au NPs is presented in Figure 6.2d.

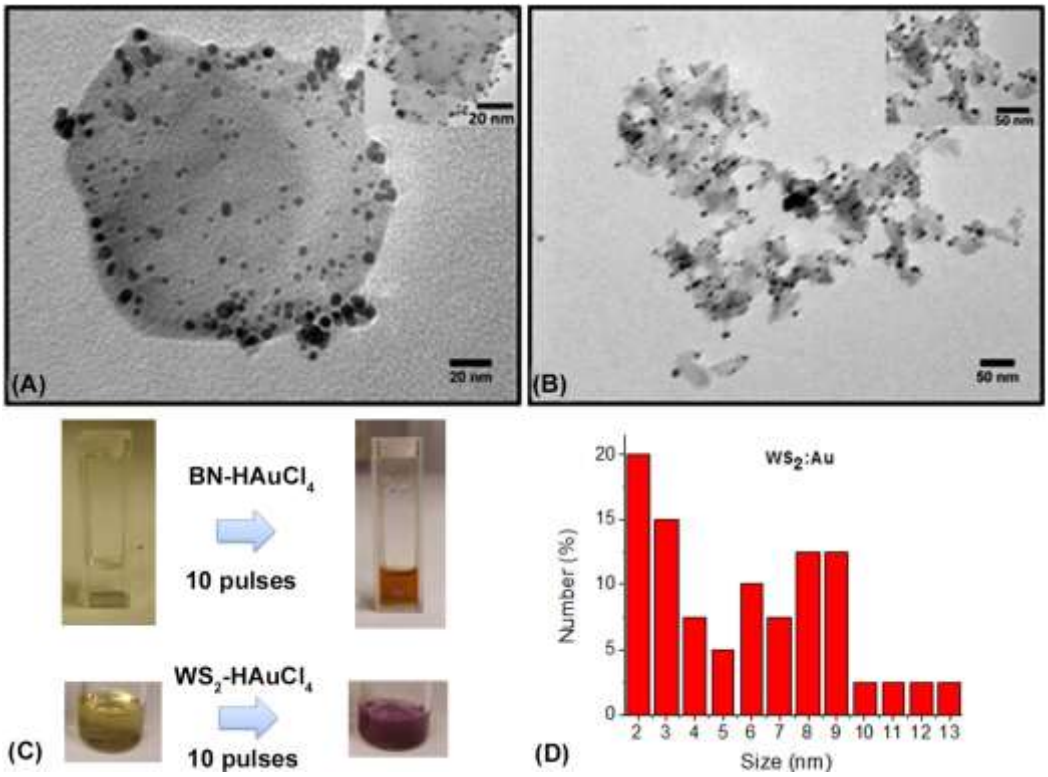

Figure 6.4: a) BN-AuNPs and b) WS_2-AuNPs NS formed after single UV laser pulse irradiation TEM images of BN-Au and WS_2-Au assemblies following the illumination of the mixed solutions (ratios 1:4 and 1:2 respectively), with a single UV pulse and fluence of 100 mJ cm^{-2}; (d) Size distribution of the Au NPs grafted onto the WS_2 NS, produced by a single, of 100mJcm^{-2}, UV pulse.

The laser-assisted assembly of NPs can be universally applied to other 2D NS such as WS_2, MoS_2 and BN. Figures 6.4a, b and 6.5a shows the respective TEM images for BN-Au and WS_2-Au and MoS_2-Au assemblies respectively, synthesized via irradiation of 1:1 mixture solutions with a single pulse of 100 mJ cm^{-2} fluence. In addition, Figures 6.5b show TEM images of BN-Au assemblies after laser irradiation of different ratios BN-$HAuCl_4$ at two energy densities (100 mJ/cm^2, 1 J/cm^2).

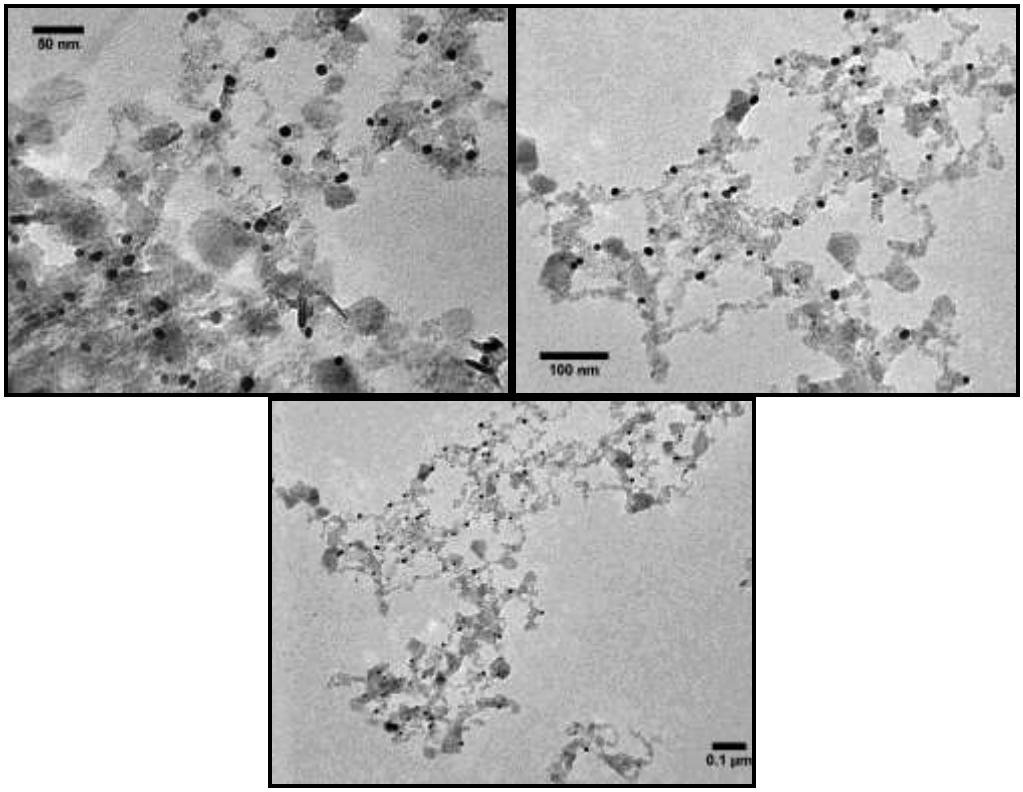

Figure 6.5a: TEM images of MoS_2-Au assemblies

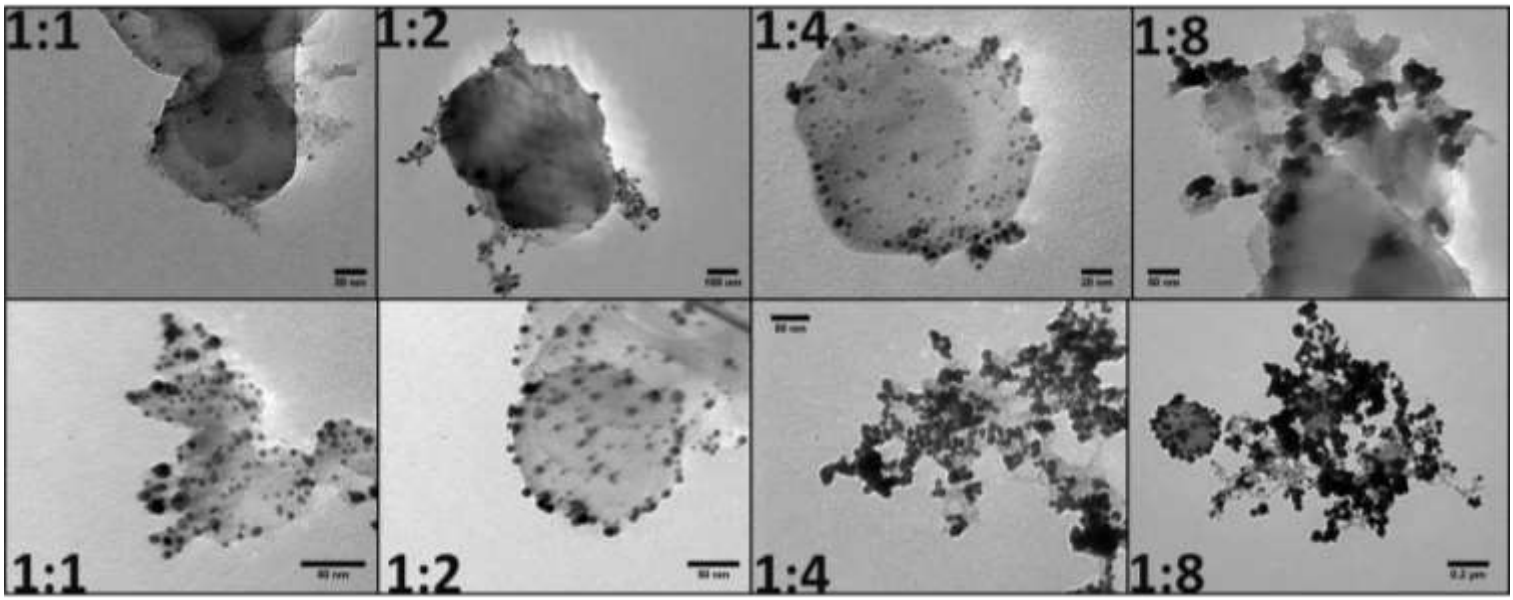

Figure 6.5b: TEM images of BN-$HAuCl_4$ solutions at different ratios after laser irradiation with single UV laser pulse at 100 mJ/cm^2 (top) and 1 J/cm^2 (bottom).

By increasing either energy density or relative ratio between 2d NS and $HAuCl_4$, formation of more NPs is observed (Figure6.5). As in the case of GO, gold NPs were uniformly dispersed onto the NSs surface. The corresponding NPs size distributions can be shown in Figure 4d for WS_2:Au and Figures 6.6, 6.7 for MoS_2-Au and BN-Au respectively; in all cases the NPs size ranged from ~1 to ~15 nm.

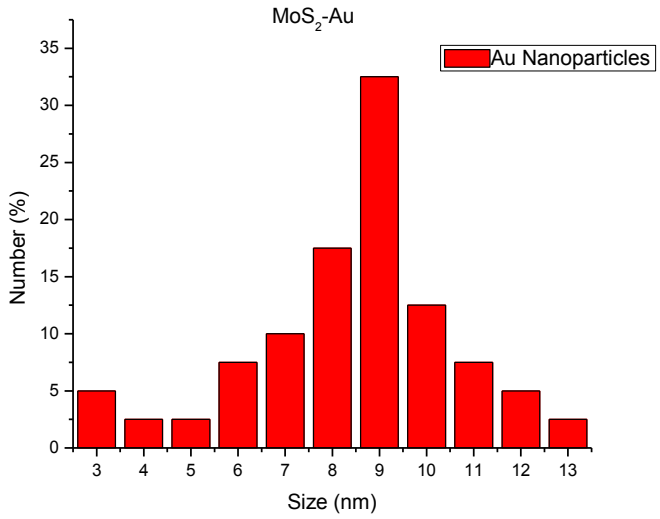

Figure 6.6: Size distribution of MoS_2-Au assemblies, produced by a single, of 100mJcm^{-2}, UV pulse.

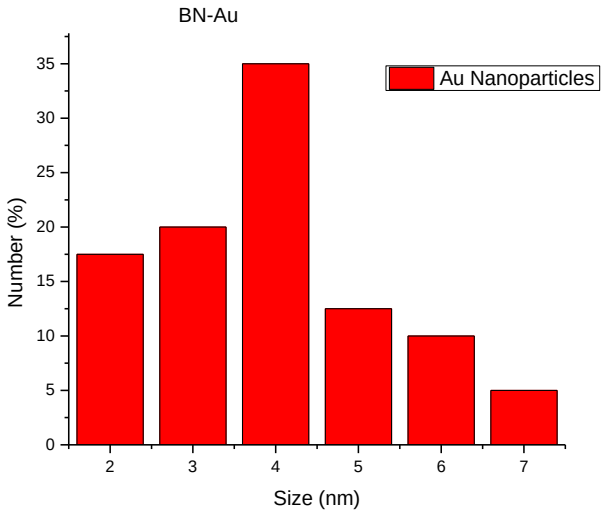

Figure 6.7: Size distribution of BN-Au NPs, produced by a single, of 100mJcm^{-2}, UV pulse.

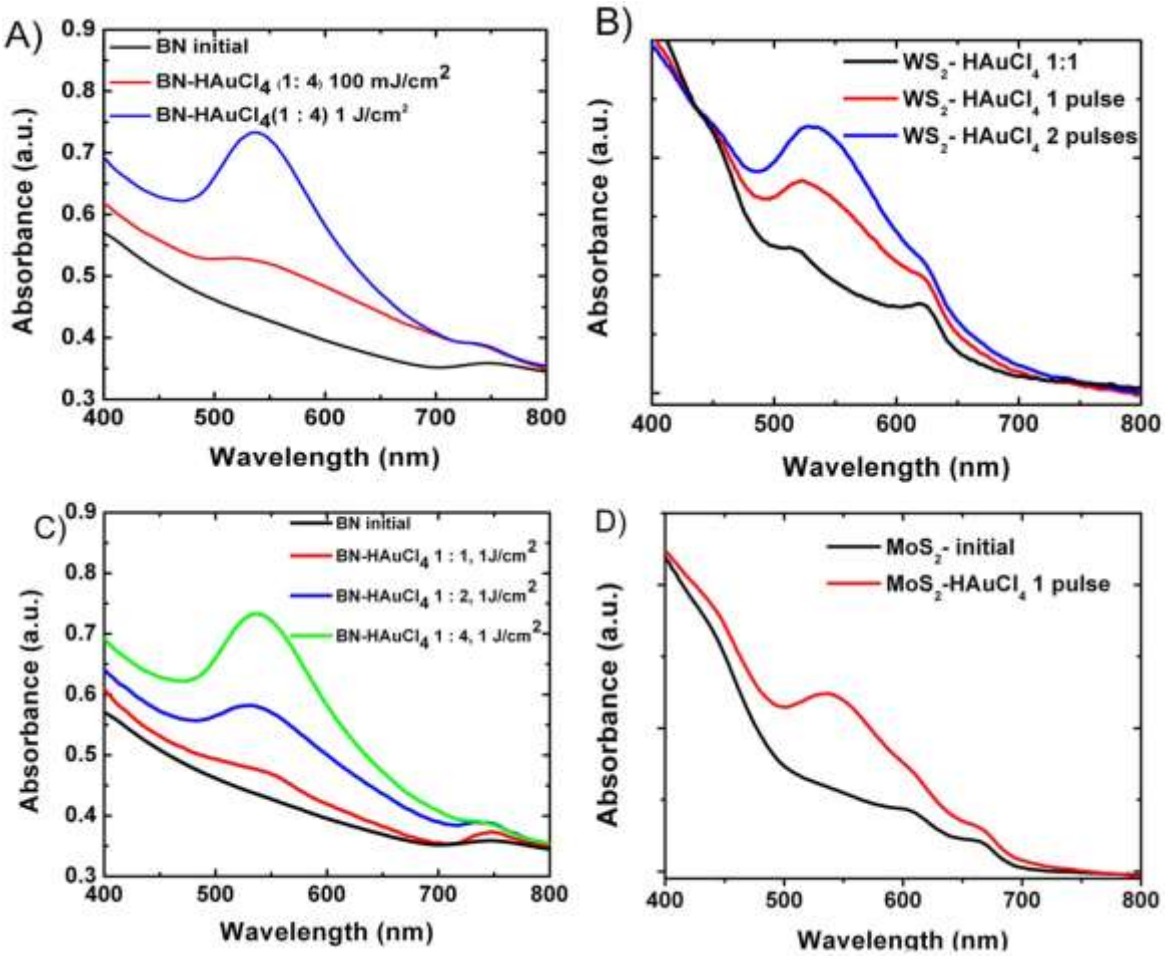

Figure 6.8: UV-Visible absorption measurements of laser illuminated a) BN-$HAuCl_4$ and b) WS_2-$HAuCl_4$ solutions with different laser fluences. UV-Visible absorption measurements of laser illuminated c) BN-$HAuCl_4$ with different relative concentrations and d) MoS_2-$HAuCl_4$ solutions before and after laser irradiation.

To further investigate the process of the laser induced NPs anchoring onto NS, the irradiation power, the number of pulses and the relative concentration of NS over the salt precursor were varied. Figure 6.8 depicts representative UV-Vis absorption spectra of laser treated BN-$HAuCl_4$ (Figs. 6.8a and 6.8c), WS_2-$HAuCl_4$ (Fig. 6.8b) and MoS_2-$HAuCl_4$ (Fig. 6.8d) dispersions at different laser fluences, number of pulses and different NS:precursor relative concentrations. A general trend is that as one increases the fluence or the pulse number or the NS:precursor ratio, the gold plasmon resonance peak becomes more pronounced. TEM imaging (not shown) revealed that the density of NPs anchored onto NSs increases accordingly. Similar results were obtained in the case of NS-Ag NPs assemblies (Figs 6.9, 6.10, 6.11).

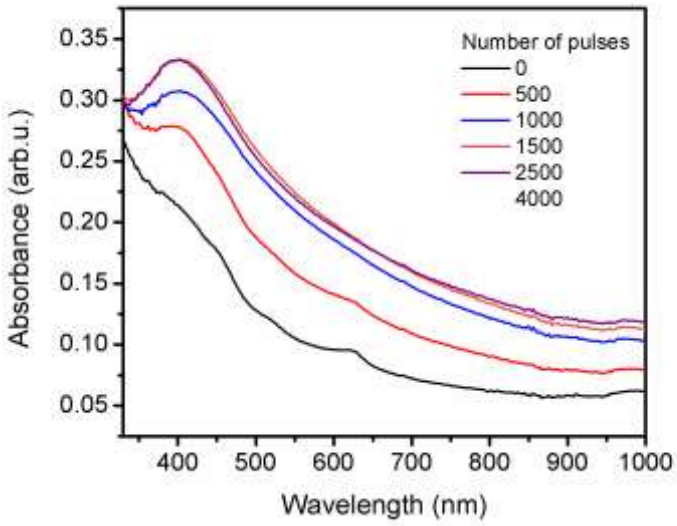

Figure 6.9: UV-vis absorption spectra of pristine WS_2-$AgNO_3$ dispersions in water, irradiated with different numbers of 100mJcm^{-2} UV pulses.

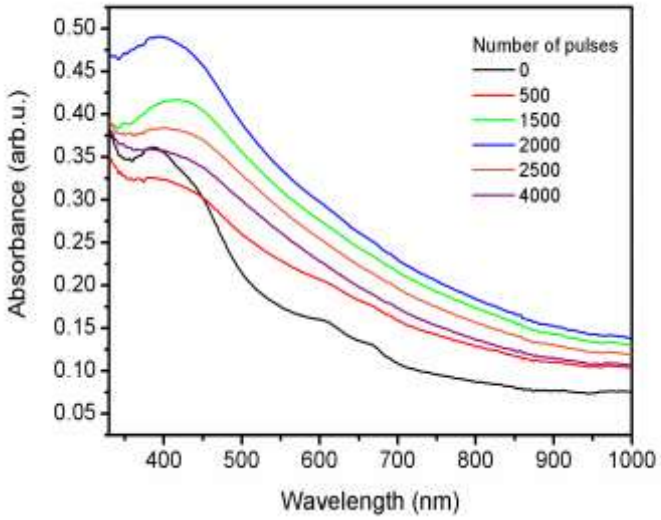

Figure 6.10: UV-vis absorption spectra of pristine MoS_2-$AgNO_3$ dispersions in water, irradiated with different numbers of 100mJcm^{-2} UV pulses.

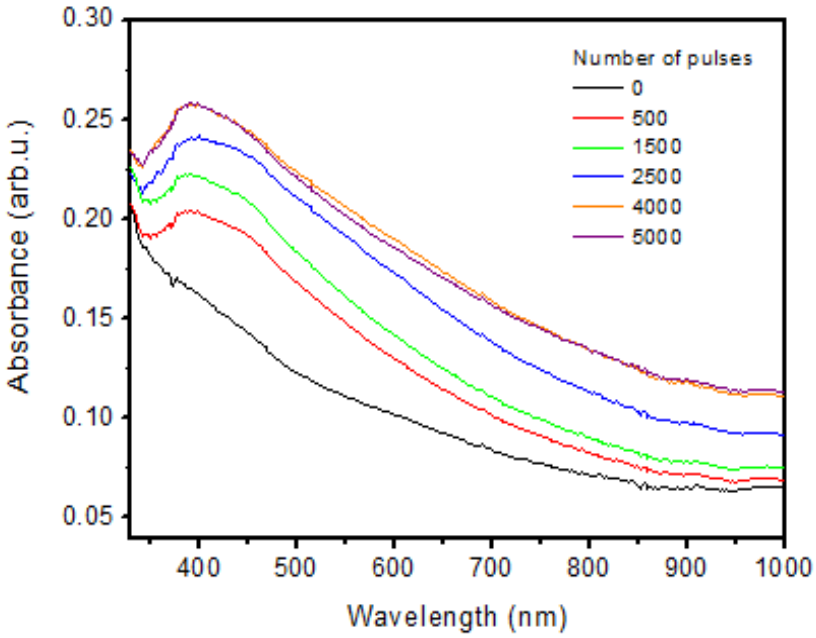

Figure 6.11: UV_VIS spectra of BN-$AgNO_3$ dispersions in water, irradiated with different numbers of 100mJcm^{-2} UV pulses.

Raman spectroscopy was employed in order to identify any laser induced structural modification of the laser treated NS dispersions. The Raman spectra of GO-Ag and GO-Au NSs, presented in Figure 6.12a, indicate that the molecular structure of GO NSs had not been affected by the laser induced synthetic process. As a result, the characteristic G and D Raman peaks of GO at 1313 cm^{-1} and 1585 cm^{-1} showed no significant changes following the irradiation process. A similar observation was made in the case of the laser synthesized WS_2-Au NSs. Indeed, the Raman spectra of the NSs before and after single pulse UV laser irradiation do not indicate any significant differences.

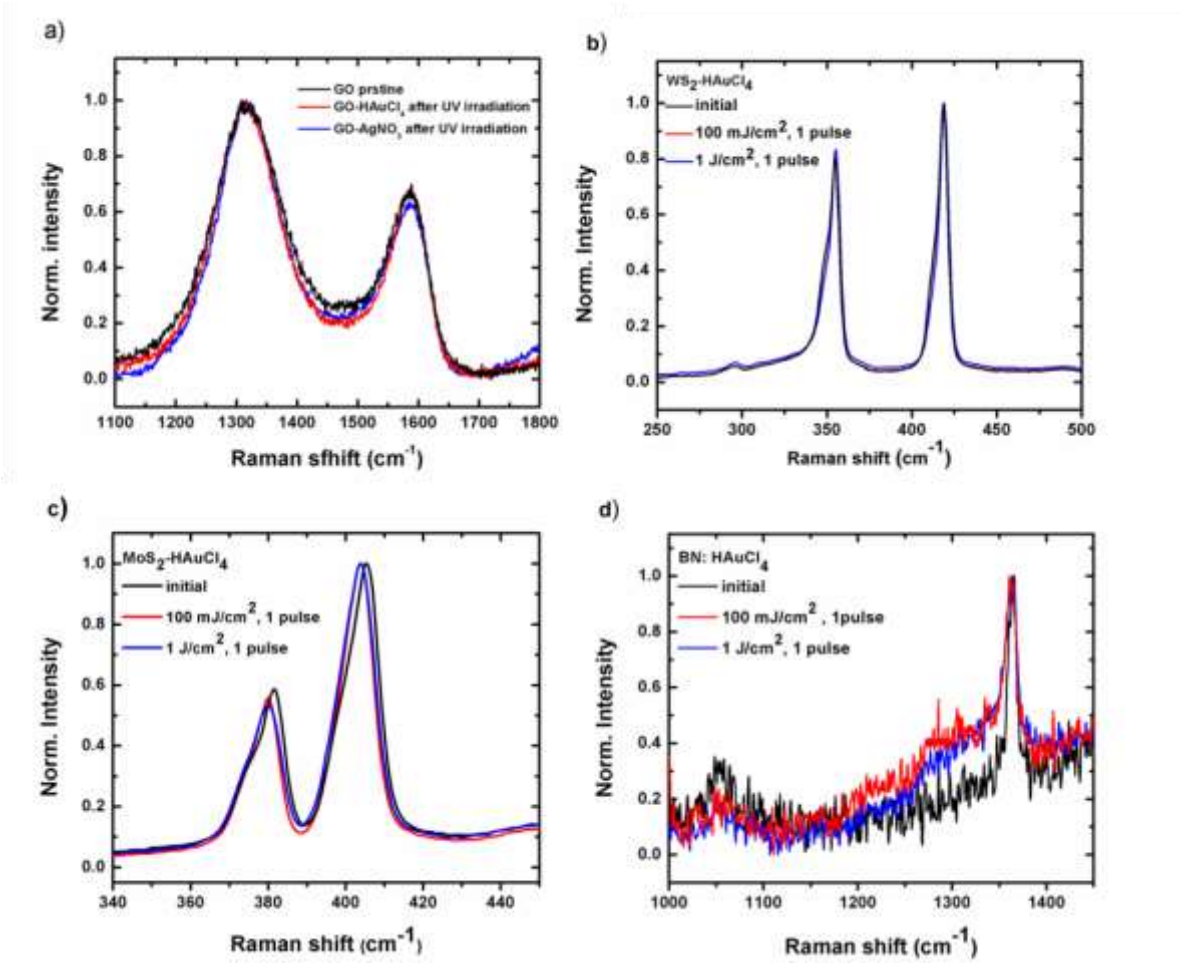

Figure 6.12: Normalized Raman spectra of a) GO, b) WS2, c) MoS2 and d) BN NS before and after laser induced decoration with metallic nanoparticles.

Figure 6.12b presents the respective spectra showing the characteristic E_{2g} and A_{1g} modes of WS_2 at 355 cm^{-1} and 418 cm^{-1} respectively. Finally, the pristine and Au NPs decorated BN NSs demonstrate a basic Raman peak at 1363 cm^{-1}, which is the characteristic peak of the hexagonal BN (h-BN) phase[97] (Figure 6.12c). The second peak appeared at around 1050 cm^{-1} corresponds to the translational optical (TO) vibrational mode of the crystalline BN (c-BN) phase. Both peaks showed no significant difference upon laser irradiation. The above results indicate that the assembly of NPs onto NS surface, without inducing any chemical modification to the pristine 2D NS.

The interest and the application of 2D materials in various building blocks of thin film solar cell technology, has been reported quite extensively[33,98,99,100,101,102,103,104]. Among the strategies adopted to facilitate the energy cascade procedure and promote the

transport of light generated charge carriers to the respective electrodes is the introduction of a third component into the photoactive binary layer, resulting in the formation of a ternary blend structure device[45,105]. The motivation behind this approach is the insertion of a material having its highest occupied molecular orbital (HOMO) and lowest unoccupied molecular orbital (LUMO) between the HOMO and LUMO of the polymer and the fullerene. This material can act either as a secondary donor or acceptor material, offering an extra interface for exciton dissociation and charge transfer[106].

Fabrication of ternary OPV devices

Semiconductor NS might be promising materials for light harvesting applications due to their unique electrical and optical properties, as well as suitable bandgap values for energetically favorable electron transfer from the polymer donor[6]. Moreover, further improvement in OPVs performance can be achieved via the use of hybrid assemblies based on NS combined with plasmonic metallic NPs[2]. In this context, the laser-generated NS-NPs assemblies developed in this work may be suitable to be used as the energy cascade material in ternary OPVs, leading to increased performance, through improved optical absorption due to the NPs, and to improved excitons dissociation and charge collection due to the 2D NS. As a proof of concept, the performance of a ternary OPV[21] based on the addition of WS_2-Au assemblies into a PCDTBT: $PC_{71}BM$ BHJ layer was investigated. It should be noted that WS_2 is chosen among the various 2D materials used here, due to its perfect energy levels[107] matching with the state of the art polymer donors used in OPVs.

The relative position of the additive component energy levels with respect to the electronic levels of the donor and the acceptor materials determines the performance of the ternary solar cell configuration. For this purpose, the HOMO and LUMO levels of WS_2 and WS_2-Au were measured by cyclic voltammetry. The measurements were conducted in a three electrode apparatus, using a Pt foil as the counter electrode and a Ag/AgCl electrode as the reference one. The voltammetric behaviors of WS_2 and WS_2-Au in acetonitrile (CH_3CN) using 0.1 M tetra-butyl-ammonium-hexa-fluorophosphate (TBAPF6) as the electrolyte at a scan rate of 100 mV s^{-1} are demonstrated in Figure 6.13.

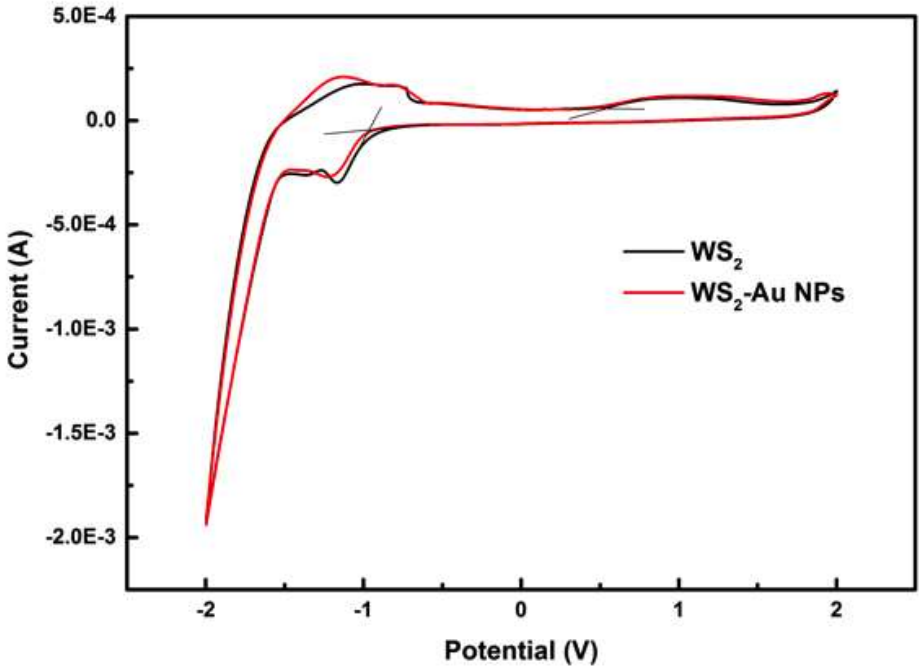

Figure 6.13: Cyclic voltammogram of WS_2 and WS_2-Au NPs in CH_3CN using 0.1 M TBAPF6 as electrolyte. Scan rate was set at 100 mV s^{-1}

The respective bands were calculated using previously reported formulas[108]. The WS_2 valence band position is approximately at -5.75 eV, calculated from the oxidation peak onset (0.65 V), while its conduction band extracted from the onset of the reduction peak (-0.97 V) is positioned at -4.13 eV. The above measurements are in agreement with previously reported values[107]. The decoration of WS_2 NS with Au NPs had no significant effect on the measured energy levels, as indicated by the slight change in the oxidation and reduction peaks in Figure 6.13. Figures 6.14a and 6.14b depict the device architecture and the energy levels of the components of the devices. It can be observed that the excitons created into PCDTBT can diffuse to both PCDTBT:WS_2-Au and PCDTBT:$PC_{71}BM$ interfaces. Moreover, the conduction band of WS_2-Au is located between the LUMO levels of PCDTBT and $PC_{71}BM$, acting as energy intermediate step, so that the electrons can be transferred towards the cathode via this energetic cascade pathway. It can be concluded that the energy levels of WS_2 perfectly match the energy levels of PCDTBT-donor and $PC_{71}BM$-acceptor, acting as an efficient electron-cascade material.

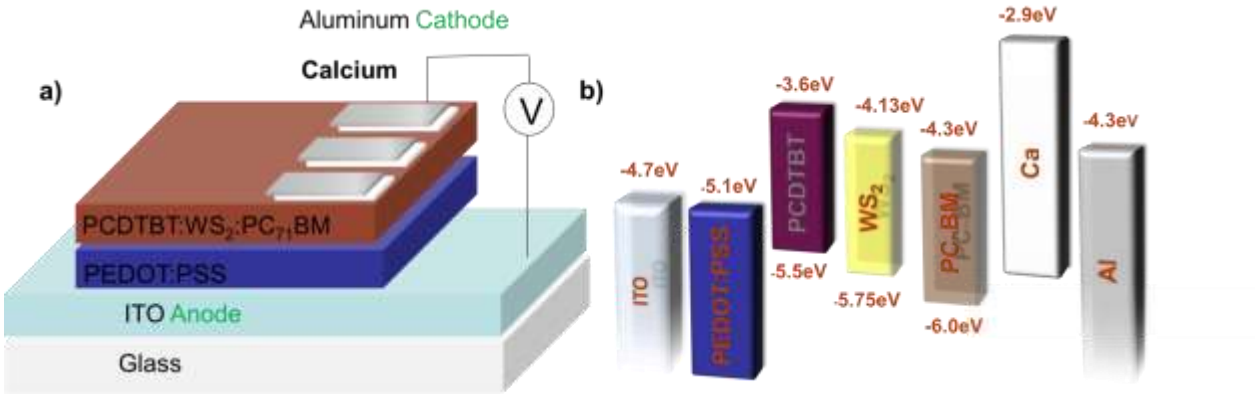

Figure 6.14: a) Schematic illustration of the sandwich-type BHJ solar cell; b) Energy level diagram of the ternary OPV cell incorporating WS_2-Au NS, showing the energy bands of the different components.

The effect of WS_2 and WS_2-NPs assemblies on the performance of BHJ solar cells was investigated by altering the additive content into the photoactive layer. In both cases the optimum additive content was found to be 1.5% v/v. Figure 6.15a demonstrates the current density-voltage (J-V) curves of the best-performed devices in each case of the three different active layers studied, namely PCDTBT:$PC_{71}BM$ (reference), PCDBT:WS_2:$PC_{71}BM$ PCDBT:WS_2-Au:$PC_{71}BM$ while, Table 1 summarizes the respective photovoltaic characteristics.

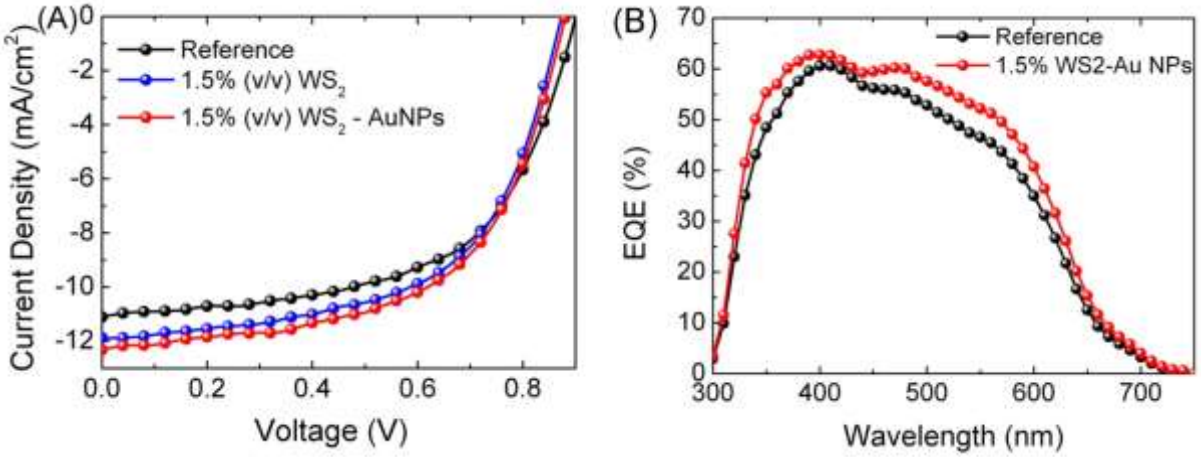

Figure 6.15: (a) J-V characteristics under 1 sun illumination (100 mW cm^{-2}) for the optimized devices incorporating the reference PCDTBT:$PC_{71}BM$, the PCDTBT:WS_2-Au:$PC_{71}BM$ and the PCDTBT:WS_2-Au:$PC_{71}BM$ blends. (b) IPCE spectra for the control device and the one containing the WS_2-Au assemblies as a ternary component.

An enhancement of the PCE of the optimized PCDTBT:WS_2:$PC_{71}BM$ based device, compared to the reference one, was observed. Specifically the PCE increased from 5.6% to 6.1%, showing an improvement of 8%, attributed to the increase of the J_{sc}. The latter is caused by improved charge-carrier separation, transportation and collection.

Notably, PCE was further enhanced for the optimized PCDTBT:WS_2-Au:$PC_{71}BM$ based devices, showing an improvement of 12.5% compared to the reference. To investigate the origin of this additional enhancement, the UV-Vis absorption spectra of PCDTBT:$PC_{71}BM$ films with and without the presence of WS_2 (1.5 %) and WS_2-Au (1.5 %) were measured and are presented in Figure 6.16. It is clear that the incorporation of both WS_2 (1.5 %) and WS_2-Au NS enhances the light harvesting of the active layer, compared to the reference film, in a broad wavelength range (380 nm-430 nm), indicating the presence of light scattering effects.

Table 1. Average photovoltaic characteristics for binary and ternary OPV devices with WS_2 and different WS_2-Au contents, as additives. To account for experimental errors, the reported averages for each case are taken for 10 identical devices, consisting of six cells each.

Device structure	J_{SC} (mA cm^{-2})	V_{OC} (V)	FF (%)	PCE (%)
PCDTBT:$PC_{71}BM$	10.6±0.13	0.89±0.1	60.2±0.3	5.6±0.1
1.5% (v/v) WS_2	11.9±0.21	0.87±0.1	59.1±0.2	6.1±0.1
1.0% (v/v) WS_2-Au	11.1±0.18	0.86±0.1	57.3±0.3	5.4±0.2
1.5% (v/v) WS_2-Au	12.3±0.22	0.89±0.1	58.4±0.2	6.3±0.1
2.5% (v/v) WS_2-Au	10.8±0.14	0.86±0.1	57.0±0.4	5.2±0.2

This complies with the TEM images of the respective NS shown in Figure 6.4b. Besides this, the spectrum of the WS_2-Au based film shows an enhancement in the wavelength region from 480 to 600 nm, which is consistent with the SPR peak of the WS_2-Au assemblies shown in Fig. 6.8b. Therefore, the absorption spectra indicate that the SPR

of the WS_2-Au nanocomposites may be responsible for the additional improvement in the OPV device performance.

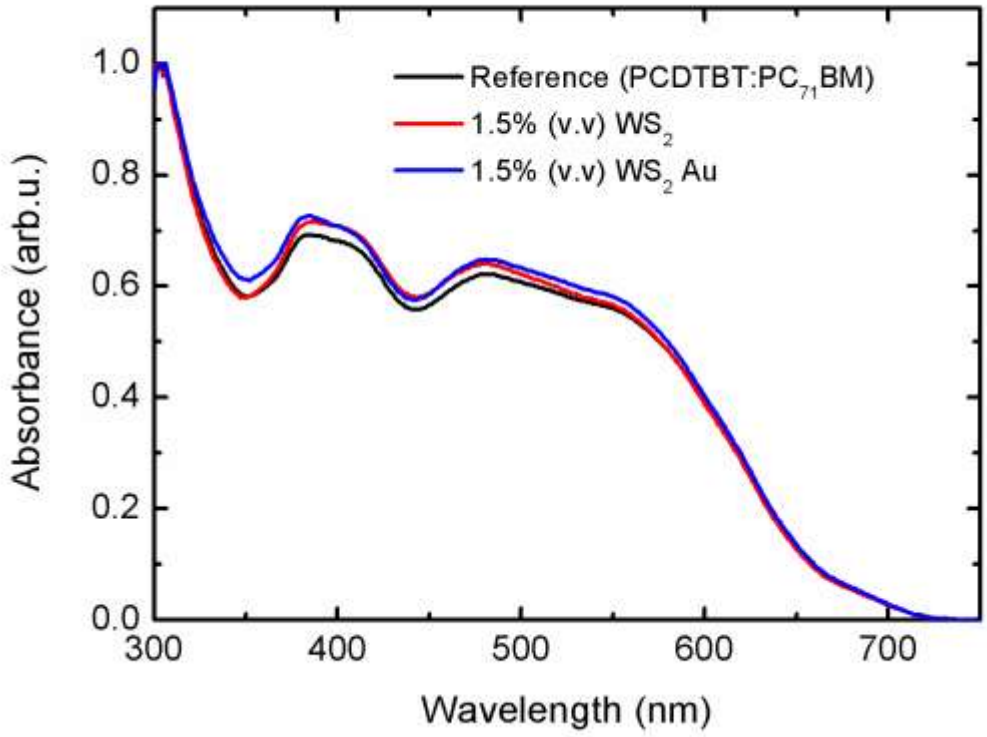

Figure 6.16: Absorption spectra of PCDTBT:PC71BM (Reference cell), ternary Solar cell with 1.5% (v/v) WS2 and ternary Solar cell with 1.5% (v/v) WS2 Au NPs.

Further insight into the light harvesting effects observed is provided by the external quantum efficiency (EQE) spectra of the reference and WS_2-Au based devices respectively, presented in Figure 6.15b. It can be observed that, although PCE for the WS_2-Au based OPV is increased, compared to the reference, in the entire wavelength range, the enhancement is more pronounced in the range 470nm-600nm. This observation complies with that obtained from the absorption spectra analysis and further supports the indication of SPR enhancement effect due to the presense of Au NPs onto the WS_2 nanosheets.

In summary, our results presented above indicate that the efficiency enhancement in the case of the WS_2-based ternary blend, can be attributed to superior charge transport

properties inside the photoactive layer, compared to the binary active layer, due to the energy levels offset between the polymer and the WS_2 intermediate component. The additional improvement in the performance of the ternary devices incorporating WS_2-Au assemblies as the third component, may be due to SPR-assisted enhanced generation of excitons.

The deterioration of the OPV performance for higher WS_2-Au content into the active medium can be attributed to additive-induced changes in the blend morphology. It is well reported that carrier scattering increases with active layer roughness, giving rise to inefficient collection of the photon-generated carriers from the respective electrodes[24]. In order to investigate this we have performed atomic force microscopy (AFM) measurements of the reference binary and the ternary layers, shown in Figure 6.17.

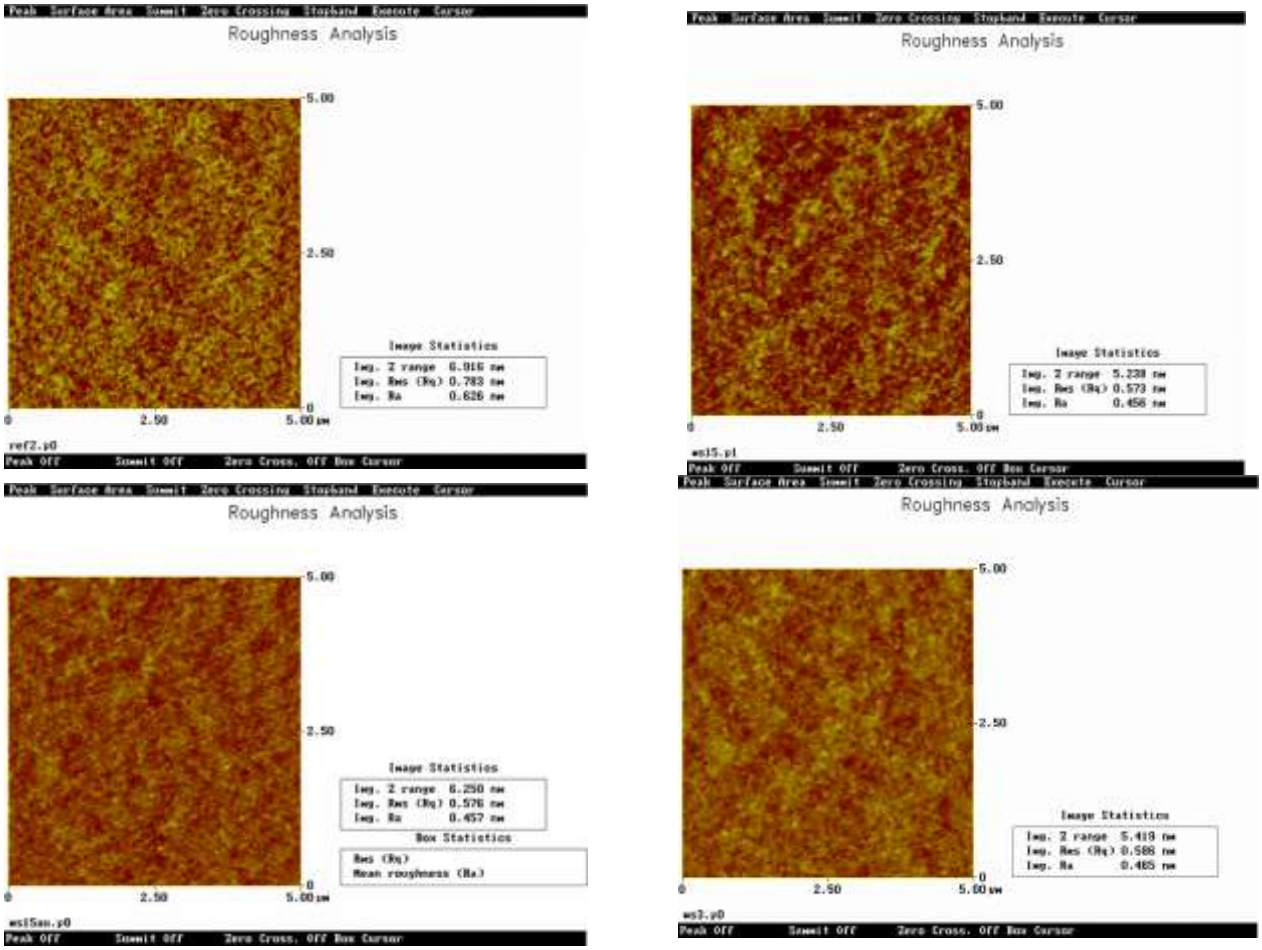

Figure 6.17: AFM images of four different devices tested a) PCDTBT:$PC_{71}BM$, b) PCDTBT:1.5% (v/v) WS_2:$PC_{71}BM$, c) PCDTBT:1.5% (v/v) WS_2-Au NPs:$PC_{71}BM$ and d) PCDTBT:2.5% (v/v) WS_2:$PC_{71}BM$. The rms roughness is 0.783 nm, 0.573 nm, 0.576 nm and 0.586 nm respectively.

Such measurements demonstrate that the lowest roughness is obtained for the layers incorporating 1.5% (v/v) WS_2 NS and 1.5% (v/v) WS_2-Au NS respectively (rms roughnesses of 0.573 nm and 0.576 nm respectively). On the contrary, the addition of higher NS concentrations leads to a corresponding increase in the layer roughness, giving rise to the degradation of the donor/acceptor interfaces, and in turn of the OPV performance.

6.4. Conclusions

In summary, we have demonstrated a facile, fast, in situ synthesis of 2D NS-NPs assemblies, via laser induced grafting of metallic NPs onto NS in solution. This is a simple, one-step process, performed at room temperature and does not require any catalysts or surfactant agents. Furthermore, it can be universally applied for practically any 2D material, giving rise to various combinations of NS-NPs assemblies. As a proof of the potential application of such assemblies, the incorporation of WS_2-Au NPs into the photoactive layer of ternary BHJ OPVs was demonstrated. The results revealed a noticeable enhancement in the photocurrent and the PCE of the respective OPV devices, attributed to the efficient synergy of plasmon enhanced absorption of Au NPs with the superior charge transport properties due to the energy levels matching between the polymer and the intermediate WS_2 NS component. Undoubtedly, this is a useful approach towards extending the spectral range of enhanced light harvesting in OPVs. The rather simple and scalable method provides unique opportunities for the cost-effective synthesis of bulk amounts of NS-NPs assemblies in solution for various applications, including printable optoelectronic devices.

Chapter 7: Photochemical Synthesis of Solution-Processable Graphene derivatives with Tunable Band-gap for Organic Solar Cells

7.1. Introduction

A photochemical route for the facile synthesis of tunable bandgap graphene-based derivatives from graphene oxide (GO) through controlled laser irradiation in liquid phase is presented. The method is facile and fast, yielding these materials within 2 hours and with excellent long-term stability. It makes use of photogenerated solvated electrons that give rise to GO reduction, accompanied by preferential attachment of the desired functional unit, intentionally dispersed into the precursor GO solution. As a proof of concept, Graphene Oxide-Ethylene-DiNitro-Benzoyl (LGO-EDNB) was photochemically synthesized and utilized as the electron acceptor material in organic bulk heterojunction solar cells (OSCs) with PCDTBT as the electron donor. The graphene derivatives are highly dispersible in organic solvents used in OSCs, while their energy levels can be readily tuned upon fine-tuning of the bandgap, which is directly related to the irradiation dose applied during the synthesis process. The utilization of LGO-EDNB with a bandgap of 1.7 eV, and a resultant lowest unoccupied molecular orbital (LUMO) level of 4.1 eV, leads to maximum open-circuit voltage of 1.17 V and to power conversion efficiency (PCE) of 2.41%, which is the highest PCE for graphene based electron acceptors to date.

7.2. Results and Discussion

All the reactions took place into a quartz reactor (Figure 7.1), containing the initial GO dispersion into which the precursor molecules were dissolved. In Figures 7.1, 7.2 and 7.3 the overall reaction process; no mechanistic details are implied. We found that laser excitation is required for the reaction (see below). In particular, as shown in Figure 7.2, the synthesis of LGO-EDNB comprises two distinct photochemical steps, an acylation and a coupling one.

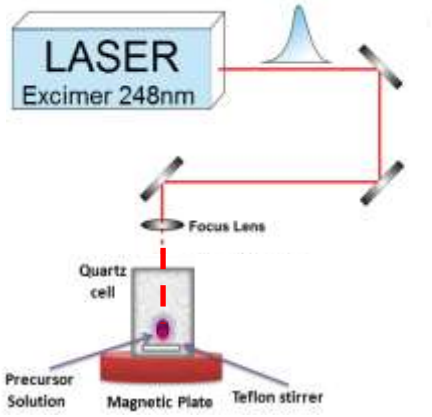

Figure 7.1: Schematic of the experimental setup used for the photochemical synthesis of LGO-EDNB.

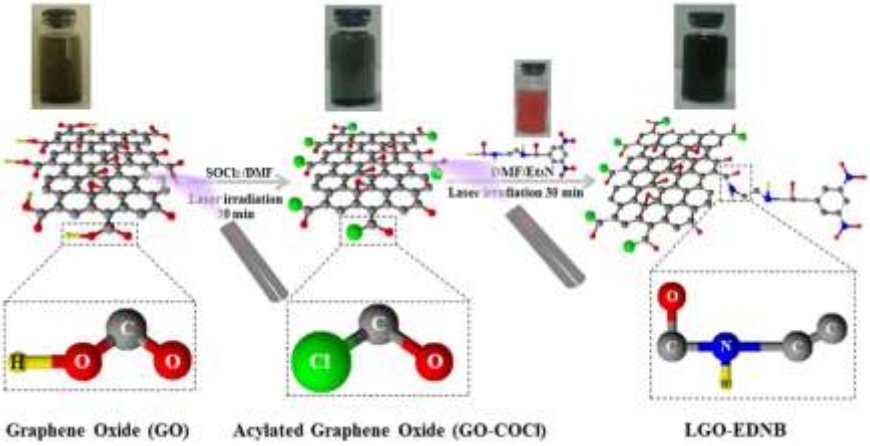

Figure 7.2: Schematic display of the spontaneous acylation of graphene oxide and (Bottom) the spontaneous grafting of ethylenediaminedinitrobenzoyl (EDNB), induced by pulsed laser.

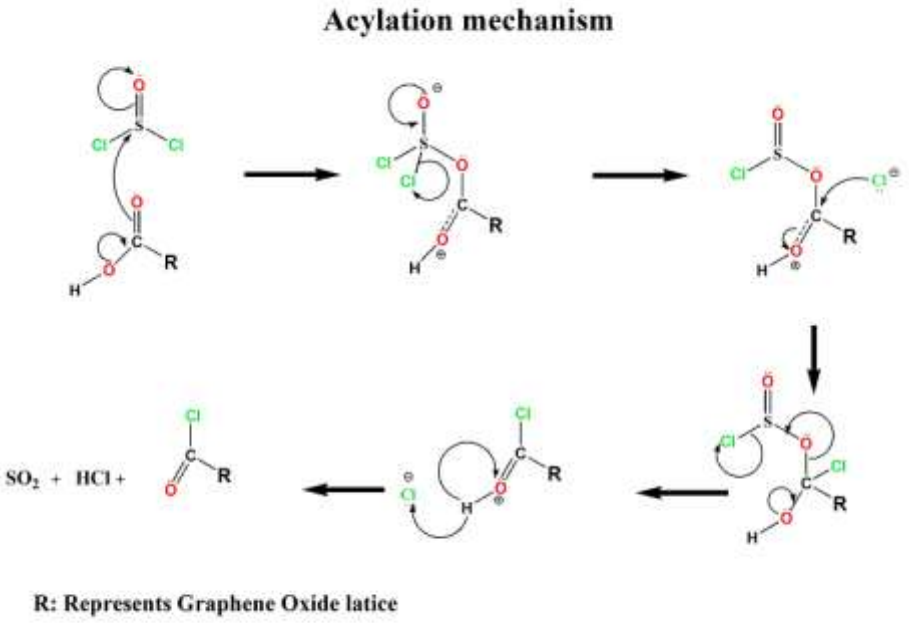

a)

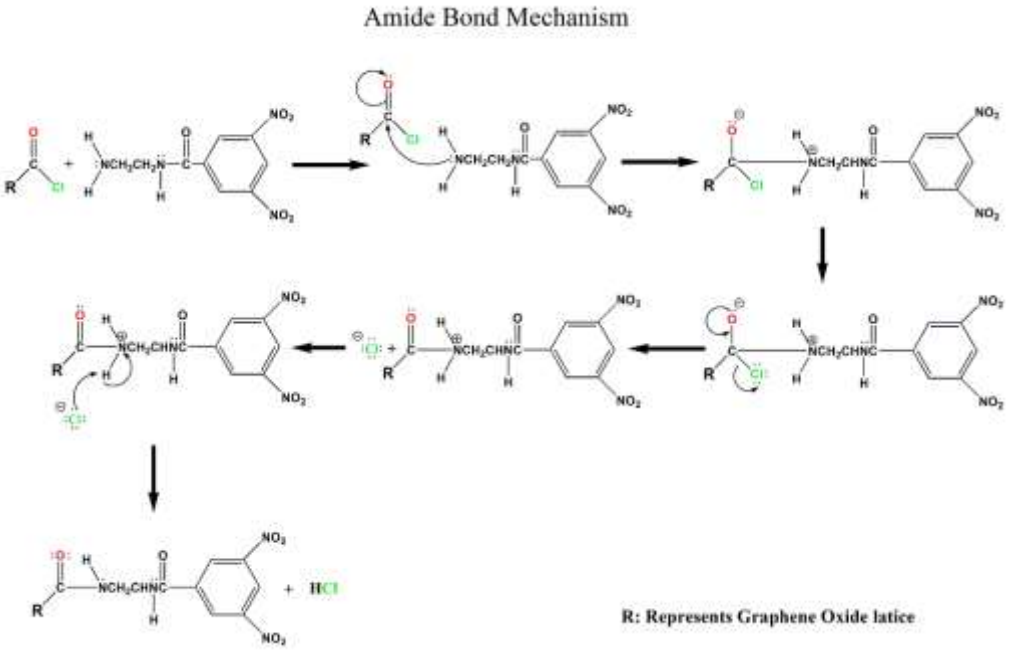

b)

Figure 7.3: The Proposed Reaction Mechanisms of (a) Acylation (b) Amide bond Mechanism.

During the first step, UV laser irradiation of GO in the presence of $SOCl_2$ gives rise to acylation of the -COOH side groups to -COCl. This reaction is highly exothermic and above a critical laser intensity cracking of the quartz tube was observed. Figure 7.3 illustrates a proposed reaction mechanism where thionyl chloride interacts in a nucleophilic fashion with a carboxylic group[109].

Light excitation provides the thermal energy required for displacement of chloride ion and subsequently carbonyl oxygen forms a sulfite ester intermediate which readily reacts with nucleophiles, as it is a good leaving group (Figure 7.3a). Upon formation of the acyl chloride, the displaced sulfite ion is unstable and decomposes into SO_2^+ and Cl^-. In the second step, the acylated GO sheets were irradiated in the presence of triethylamine (Et_3N) and are linked with small molecule via amide bonds, formed between the COCl groups and 3,5-dinitrobenzoyl chloride with the amino groups of Et_3N (Figure 3b).

During the different reaction steps notable changes in the coloration of the irradiated solution were observed (Figure 1). The exothermic nature of the reactions observed in our experiments complies with laser-initiated chemical transformations via photothermal bond cleavage, previously reported in GO as well as in hydrogenated and halogenated graphene[110]. It can thus be proposed that rapid heat transfer[111] from GO to the precursor solution due to the photothermal reduction of GO lattice is triggering the acylation and amidation reactions. Accordingly, the efficiency of the photochemical process is unexpectedly high; the final product can be delivered within a couple of hours, which is much faster than the commonly used synthetic routes.

Following irradiation, spectroscopy (XPS) was used to probe the chemical modifications introduced into the GO lattice. Figure 4a compares typical XPS spectra of GO and LGO-EDNB respectively. From these data it can be seen that the intensity of the O1s peak relative to that of C1s is reduced while the characteristic N1s peak appears after irradiation. These results indicate laser-induced simultaneous reduction and N-based functionalization of the GO sheets. The Na peaks visible in the XPS scans are contributions from the sample mounting procedure and can therefore be ignored. Analysis of the core level characteristic peaks allowed insight to be gained into the nature of the chemical bonds in each case.

Figure 7.4b presents in high resolution the respective C1s of GO (top) and LGO-EDNB (bottom) produced upon irradiation with 10 pulses of 10 mW power, respectively. In particular, the XPS spectrum of GO showed a second peak at higher binding energies, corresponding to large amounts of sp^3 carbon with C-O bonds, carbonyls (C=O), and carboxylates (O-C=O), resulted from harsh oxidation and destruction of the sp^2 atomic structure of graphene[112]. After irradiation, the C-O/C-C intensity ratio decreases from 1.09 to 0.71 indicating reduction of the GO lattice. At the same time the N1s/C1s intensity ratio becomes equal to 0.17. Photo-excitation is a well-established method for GO reduction, mediated by photogenerated solvated electrons[113]. However, since our KrF laser source is of high photon energy (248 nm, 5eV) it is much more efficient for photothermal dissociation of oxygen-related bonds[110].

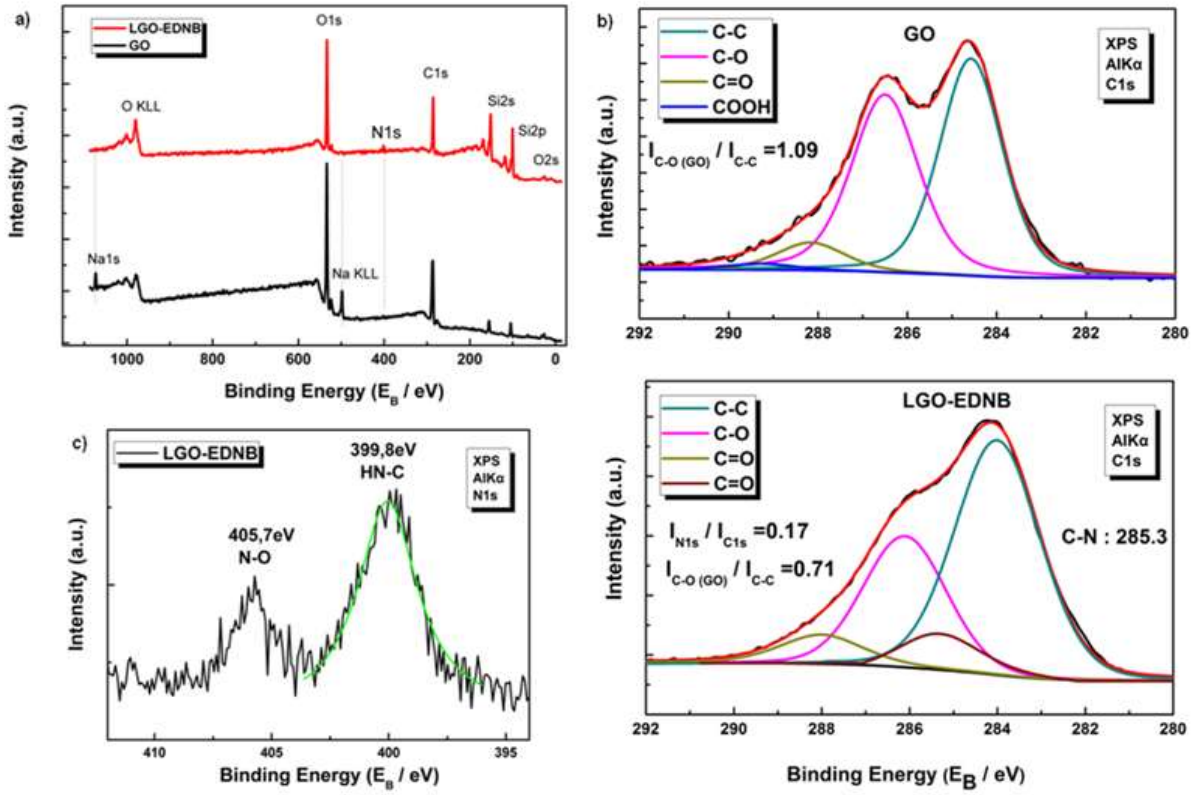

Figure 7.4: (a) XPS survey spectra of GO and LGO-EDNB; (b) high-resolution XPS C1s spectra of GO (top) and LGO-EDNB (bottom); (c) high-resolution N1s XPS spectra.

We investigated the bonding configurations in laser synthesized derivative based on high-resolution N1s XPS spectra; a typical example is presented in Figure 7.4c. It comprises two peaks, one of higher binding energy, corresponding to N-O bonding and one of lower, corresponding to N-C bonds[114].

In particular, the peak at 399.8 eV is likely to be associated with various reduced forms of nitrogen such as NH_2 (399.4 eV), NHOH (400.3 eV), NH-pyrrolic (400.5 eV) and azoxy (399.98 eV) groups[115], while that of 405.7 eV corresponds to the NO_2 groups bound to aromatic carbon within the EDNB functionalized unit[109,116].

LGO-EDNB was further checked by Fourier transform infrared (FT-IR) spectroscopy (Figure 7.5), showing two new bands at 1543 and 1345 cm^{-1} compared to pristine GO, which are characteristic of the symmetric and asymmetric stretching modes of the NO_2 group[117].

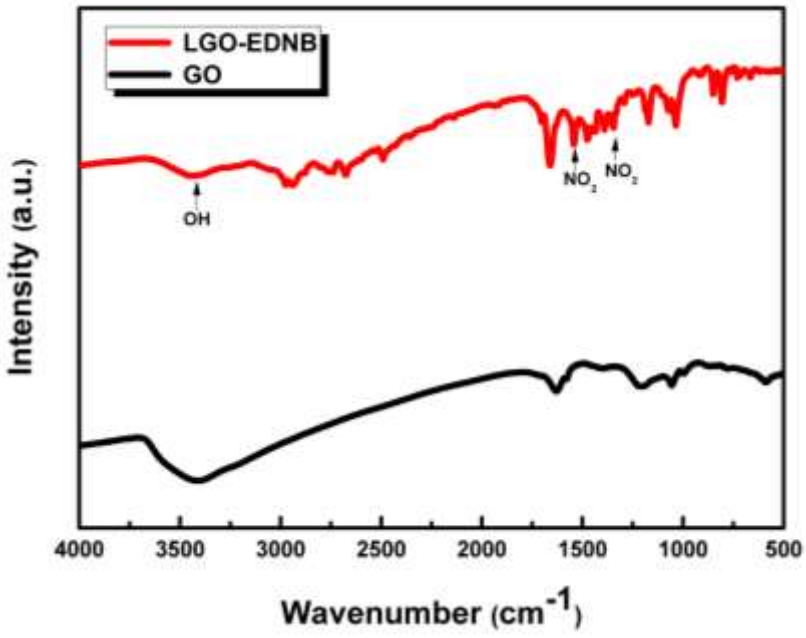

Figure 7.5: Fourier transform infrared (FT-IR) spectra of LGO-EDNB

Compared to the FT-IR spectrum of the pristine GO dispersion, it is clear that the -OH characteristic peak at ~3400 cm^{-1} is significantly reduced, denoting that there is a partial

reduction of the GO lattice during the irradiation process, in accordance to the XPS results. Figure 7.6 also depicts the Raman spectra of GO and LGO-EDNB. GO displays characteristic peaks at 1581 and 1346 cm^{-1}, corresponding to G and D bands, respectively.

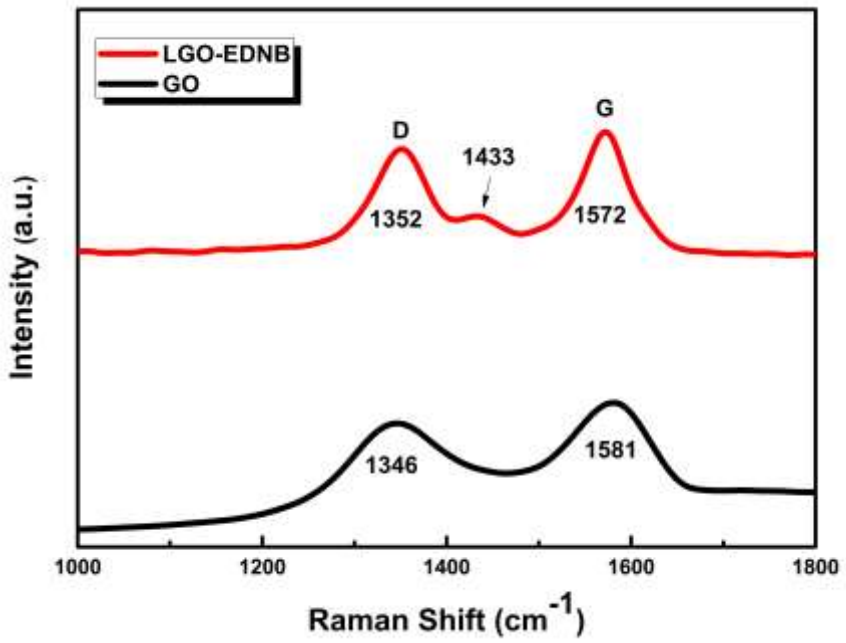

Figure 7.6: Raman spectra of GO (black) and LGO-EDNB (red).

These peaks were shifted to 1572 and 1352 cm^{-1} respectively in the spectrum of LGO-EDNB. Furthermore, the I_D/I_G intensity ratio is increased from 0.84 in pristine GO to 0.94 in LGO-EDNB. Notably, the spectrum of LGO-EDNB appears an additional weak shoulder at 1433 cm^{-1} that can be attributed to the deoxygenation of GO[118], due to the grafting of the parietal EDNB moieties to the COOH groups of the GO sheets. All these observations confirm the substantial modification of the GO lattice due to the laser-induced functionalization process.

In our technique, by carefully tuning key laser parameters, the lattice reduction degree and, in series, the functionalization level could be readily controlled. In particular, it is observed that an increase of P in the range from 10 mW to 50 mW or an increase of Number of pulses

at a certain Power, gives rise to a corresponding decrease of the respective N1s peak intensity.

Accordingly, as shown in Figure 7.7a, there is a rapid decrease of the N1s/C1s intensity ratio upon increasing Np at a constant P=10 mW, while at the same time a sharp increase in the GO reduction ratio is evident. This sharp drop of the functionalization degree with exposure time may be due to the simultaneous rapid reduction of the oxygen moieties from the GO lattice. As a result, according to the proposed mechanism presented in Figure 7.3, the available carboxyl-related functionalization sites become significantly lower. This effect was further studied by UV-vis spectroscopy. Figure 7.8 presents the respective absorption spectra showing that, as the exposure time increases, the LGO-EDNB absorption is enhanced in the whole spectral range. At the same time, the absorption band becomes progressively broader, indicating laser mediated bandgap modulation[119] of the LGO-EDNB derivatives.

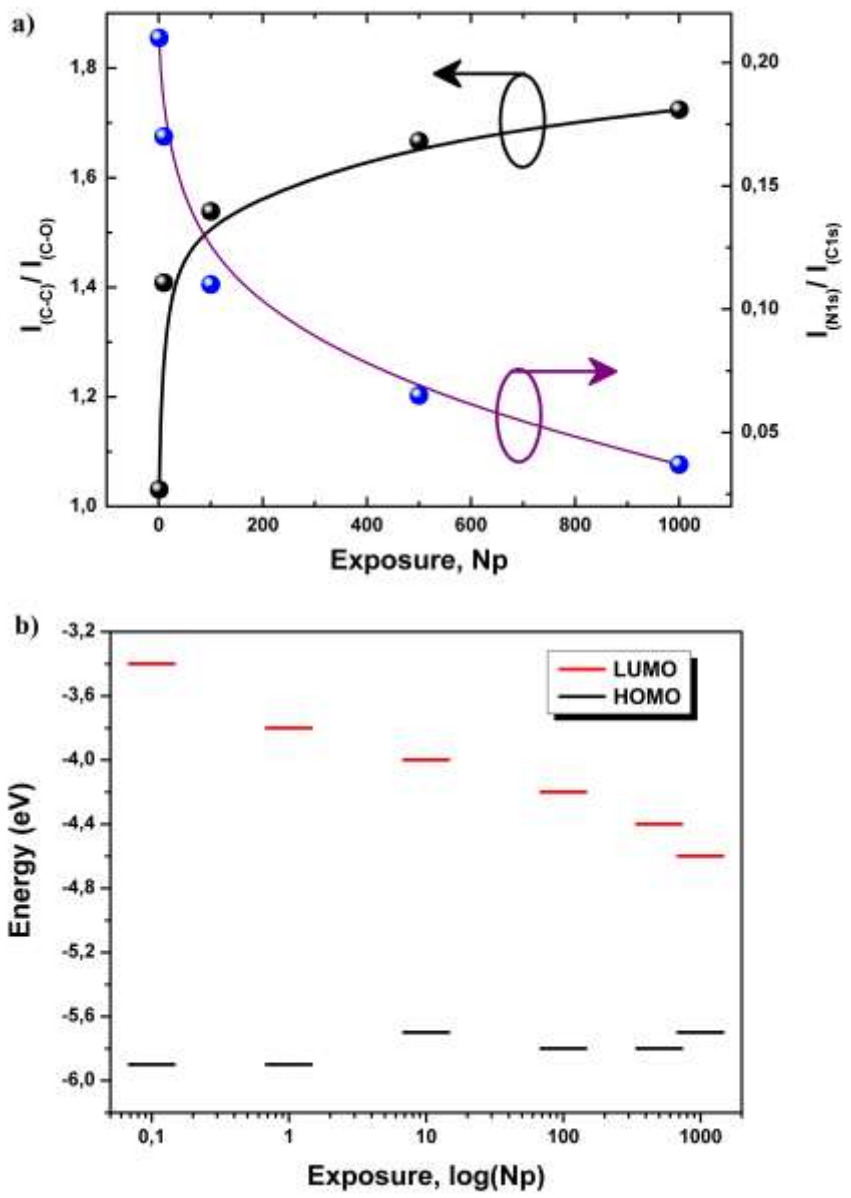

Figure 7.7: (a) GO reduction and functionalization levels as a function of Np (b) the evolution of the HOMO and LUMO levels as a function of irradiation time. The HOMO-LUMO levels of GO-EDNB are also shown for comparison.

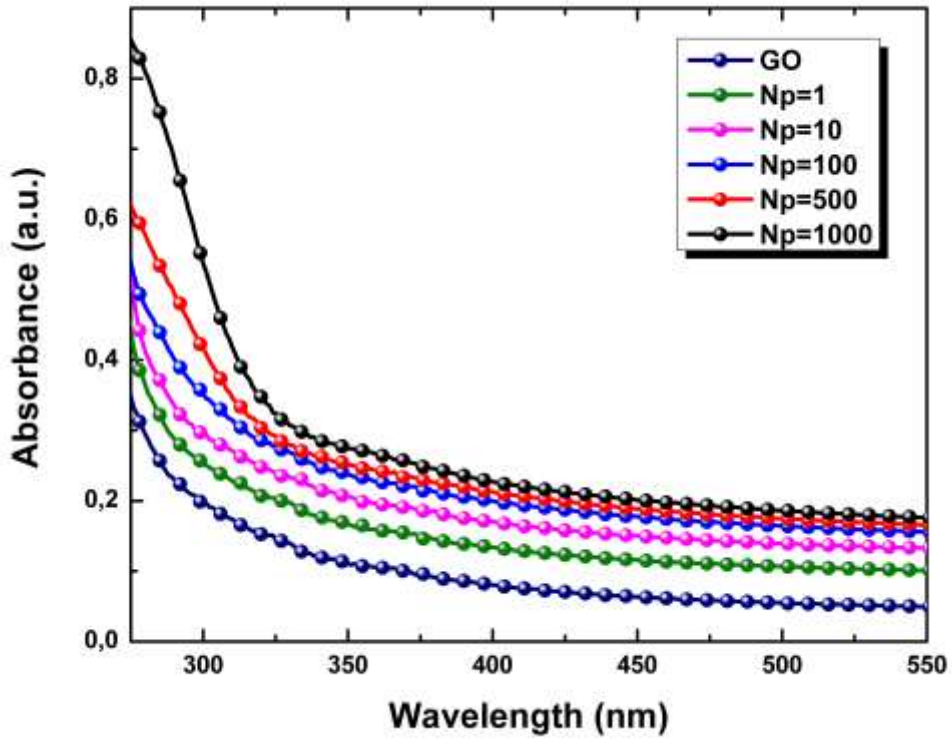

Figure 7.8: The absorption UV-vis spectra of LGO-EDNB as a function of irradiation time

To further explore potential changes in the electronic bandgap, CV measurements were carried out on LGO-EDNB derivatives produced at different exposure times.

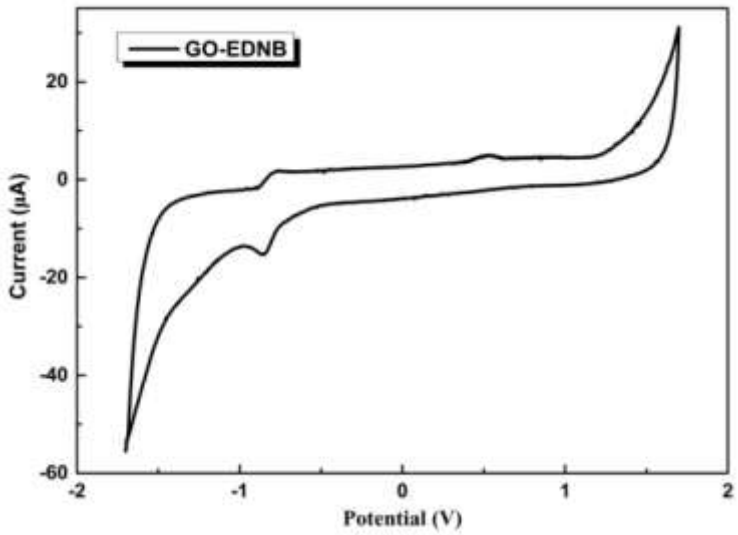

Figure 7.9: The voltammetric behavior of LGO-EDNB (prepared at 10mw, 100 pulses)

The results revealed well-defined oxidation and reduction peaks (Figure 7.9), the position of which changes with the exposure time. From the onset of oxidation ($E_{[onset,\ ox\ vs.\ Fc+/Fc]}$) and reduction ($E_{[onset,\ red\ vs.\ Fc+/Fc]}$) potentials, the highest occupied and lowest unoccupied molecular orbitals (HOMO and LUMO, respectively) can be calculated. The obtained electrochemical data are summarized in Figure 7.7b that presents the evolution of the HOMO and LUMO levels as a function of irradiation time. It is evident that the HOMO-LUMO level separation, and thus the bandgap, decreases with increased exposure time most likely due to a synergetic effect of the EDNB-functionalization and the partial reduction processes (Figure 7.10).

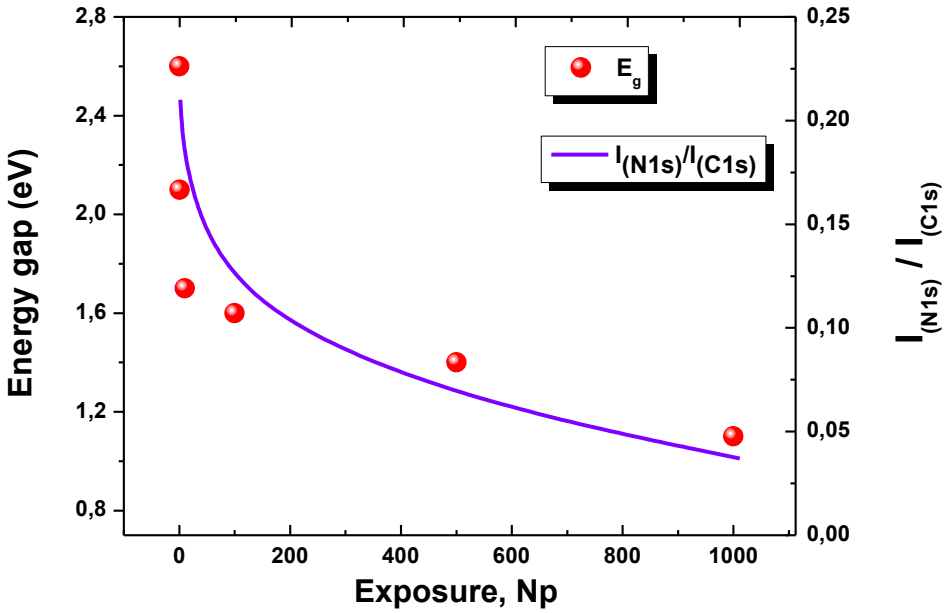

Figure 7.10: The HOMO-LUMO levels separation of LGO-EDNB as a function of irradiation time.

It can be postulated that the large-scale coupling between EDNB and GO sheets facilitates charge transfer interaction, giving rise to the decreased bandgap observed for LGO-EDNB[120,121]. It has been demonstrated that laser induced photochemical transformations which involve cleaving of bonds from a graphene surface produce heat which can effectively be used to understand the kinetics of such transformations[34,39]. In our case we observed that for a constant laser power, increase of the laser repetition rate gives rise to a corresponding enhancement of the temperature rise accompanying the laser functionalization process. Based on the above observation we postulate a mechanism that involves the absorption of the 5 eV photon energy by GO (bandgap of ~2.3 eV[115]) resulting in the formation of a heated electron gas that subsequently cools over a picosecond time scale via exchanging energy with the GO lattice. The observed temperature rise reflects the steady-state net heat transfer from GO to the EDNB precursor solution following the deoxygenation of GO by photothermal energy conversion. Heat transfer facilitates charge transfer interaction and coupling between EDNB and GO and as a result the HOMO-LUMO

separation of the final LGO-EDNB product is close to the bandgap of the reduced GO lattice. Time-resolved pump-probe experiments are required to further investigate the energetics and dynamics of this interaction during laser irradiation.

The bandgap tunability of the laser-functionalized graphene derivatives demonstrates potential application of LGO-EDNB in solution processed electronics. In addition to this, the direct linking of the electron-withdrawing nitro group with the GO backbone facilitates enhanced exciton dissociation, due to the presence of the aliphatic linker of ethylenediamine, which demonstrates its potential application as electron acceptor in OSCs. On the other hand, we found that the LGO-EDNB flakes produced are extremely soluble in common organic solvents compared to the starting GO material as well as the chemically synthesized GO-EDNB[28]. Indeed, thermogravimetric measurements performed on LGO-EDNB and GO-EDNB (Figure 7.11) indicate the higher degree of functionalization in case of LGO-EDNB; more amide bonds are formed, as well as more chromophores nitro groups are linked at the edges of GO sheets.

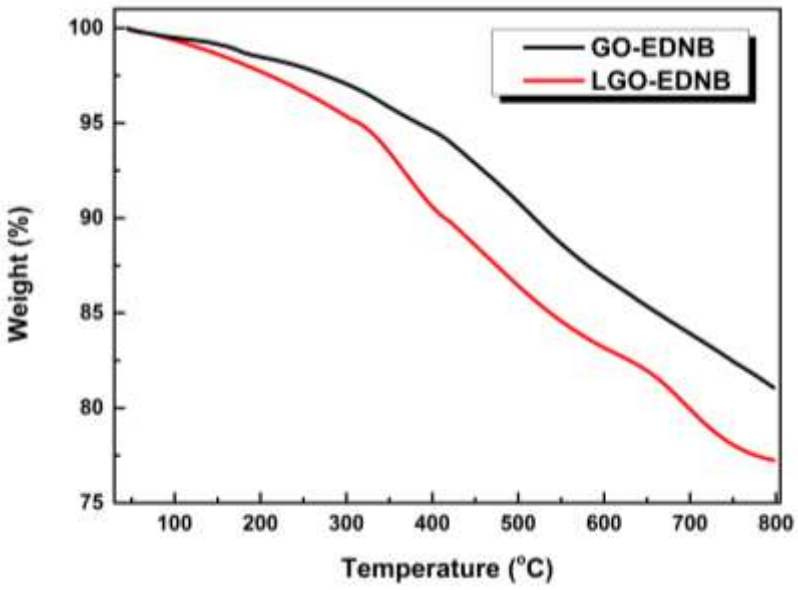

Figure 7.11: The TGA graphs of LGO-EDNB, prepared using Np=10 pulses, and GO-EDNB obtained under inert atmosphere of N_2, with heating rate 10 °C/min.

Owing to the higher degree of functionalization and the presence of excess aliphatic groups (-CH2-), the dispersibility within the polymer matrix is facilitated and thus the interactions between the polymer and graphene phases are enhanced. All the above properties are desirable towards the structure/property characterization and OSC device fabrication by solution processing.

In order to investigate the electron accessible nature of LGO-EDNB, BHJ photovoltaic devices were fabricated utilizing the LGO-EDNB as the electron acceptor and the PCDTBT as the electron donor. For this purpose, OSCs with the conventional device structure glass /indium tin oxide ITO/PEDOT:PSS/PCDTBT:LGO-EDNB/Al, where fabricated. The corresponding OSC structure and the energy level diagram of the different materials comprising the devices are shown in Figure 7.12a and 7.12b. Before analyzing the photovoltaic characteristics, it is important to describe the functionality of the electron acceptor component of the BHJ during the device operation. The solar light irradiates the photoactive layer through the PEDOT:PSS/ITO electrode side, while the donor molecules absorbs photons to produce excitons. The photo-induced excitons dissociate at the donor-acceptor interface into electrons in the lowest unoccupied molecular orbital (LUMO) of the acceptor, and holes in the highest occupied molecular orbital (HOMO) of the polymer donor. Therefore, the LUMO level of the acceptor should be ideally below that of the donor so that the electrons can be readily transported to the Al electrode. At the same time its HOMO level should be above that of the donor to facilitate holes' transport.

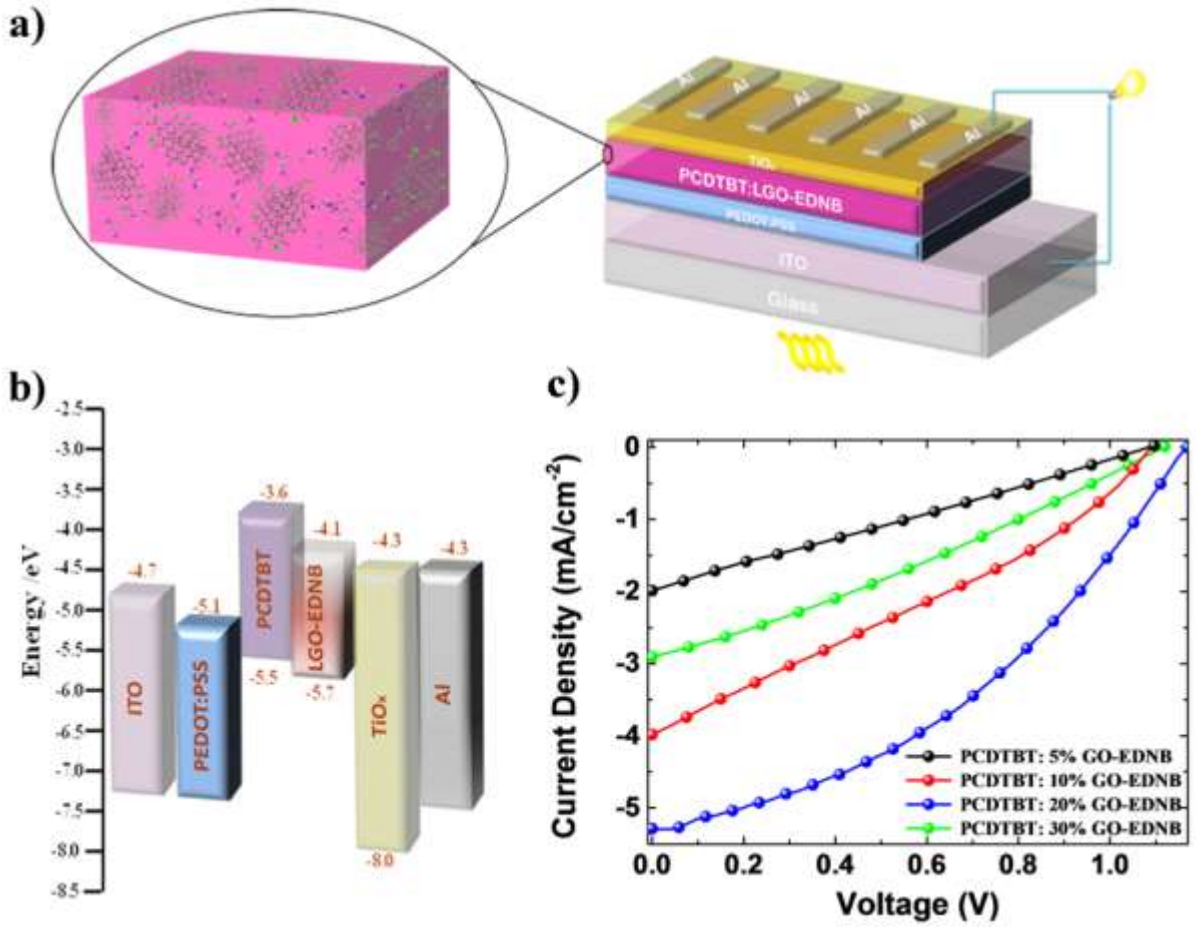

Figure 7.12: (a) Schematic illustration of BHJ OSC device with LGO-EDNB as the electron acceptor (b) The energy level diagram depicting the relevant energy levels under flat conditions of all materials used in OSCs (c) J-V characteristics of OSCs with different LGO-EDNB concentrations.

Initially, a series of devices using LGO-EDNB acceptors obtained at different exposure times and exhibit different HOMO-LUMO levels (Figure 7.7b), were tested. It is found that the best photovoltaic performance was measured for the OSCs incorporating the LGO-EDNB derivative obtained for Np=10 pulses, regardless the polymer-donor ratio. This can be attributed to the best matching between the energy levels of this derivative and the polymer donor that facilitates efficient exciton dissociation, as indeed can be observed in figure 7.12b. Besides this, the lower HOMO level of LGO-EDNB acts as an efficient barrier to hole extraction, through the acceptor material, minimizing charge recombination. It is

important to note that devices fabricated with chemically synthesized GO-EDNB[28] as electron accepting materials failed to produced photovoltaic effect, apparently because its LUMO level ($LUMO_{GO\text{-}EDNB}$=3.4 eV), shown in Figure 7.7b, is lower that of PCDTBT ($LUMO_{PCDTBT}$=3.6 eV).

In a next step, OSCs fabricated using different blend ratios of the best performed PCDTBT:LGO-EDNB BHJ were compared. As it can be seen in the respective J–V curves of Figure 7.12c and the summarized photovoltaic parameters in Table 1, device performance strongly depends on the donor-acceptor ratio. Indeed, the maximum efficiency is attained using the composite BHJ blend containing 20% of LGO-EDNB. For concentrations higher than 20% w.t., the photocurrent is believed to be limited due to increased aggregation of graphene sheets leading to a lower photogeneration rate. The measured of V_{oc} of 1.17 V for PCDTBT:LGO-EDNB OSC showed the best efficiency, can be explained as the difference between the LGO-EDNB LUMO (-4.1 eV) and the PCDTBT HOMO (-5.5 eV) energy levels[122]. The above results show the importance of the tunability of the LGO-EDNB acceptor HOMO-LUMO levels, suggesting the applicability of our technique to practically any polymer donor system.

Table 1. Average photovoltaic characteristics and standard deviations for OPV devices based on PCDTBT:LGO-EDNB composites with different LGO-EDNB content (5, 10, 20 and 30 wt%). The numbers in parentheses represent the values obtained for the champion OPV cells. To account for experimental errors, the reported averages and deviations for each device are taken for 10 identical devices, consisting of 6 cells each.

Device Structure	J_{sc}(mA/cm^2)	V_{oc}(V)	FF(%)	PCE(%) (max. value)
ITO/PEDOT:PSS/PCDTBT:LGO EDNB(5%)/TiO_x/Al	1.99±0.22	1.10±0.05	25.5±0.4	0.55±0.11 (0.66)
ITO/PEDOT:PSS/PCDTBT:LGO-EDNB(10%)/TiO_x /Al	3.98±0.20	1.09±0.06	31.1±0.3	1.34±0.17 (1.51)
ITO/PEDOT:PSS/PCDTBT:LGO-EDNB(20%)/TiO_x /Al	5.29±0.25	1.17±0.06	39.2±0.5	2.42±0.29 (2.71)
ITO/PEDOT:PSS/PCDTBT:LGO-EDNB(30%)/TiO_x /Al	2.91±0.19	1.12±0.03	29.0±0.3	0.95±0.09 (1.04)

The best performed PCDTBT:LGO-EDNB based device showed a J_{sc} of 5.29 mA/cm^2 and PCE 2.41 %, which is the highest than the previously reported which incorporated covalently-modified graphene[123,124] and 71% higher than the state of the art graphene-based electron acceptor materials[29]. Such efficiency enhancement can be attributed to the formation of internal polymer/graphene junctions giving rise to higher exciton dissociation and balanced charge transport throughout the entire volume of the PCDTBT:LGO-EDNB composite. The photovoltaic properties of our LGO-EDNB-based devices are rather satisfactory considering that these OSCs use a new type of electron-acceptor material, different from the most-studied fullerene system. Indeed, the performance of those devices was reached without any attempt to optimize the morphology of the active blend which is the significant extrinsic factor that impacts all the device characteristics. Further studies

focusing on the graphene sheet size and blend structure effects on the OSC characteristics are required for further optimization.

7.3. Experimental

Synthesis of Graphite oxide (GO): Graphite oxide was prepared from purified natural graphite powder (Alfa Aesar, ~200 mesh)**,** by a modified Hummers method[125]. Briefly, graphite powder (0.5 g) was placed into a cold mixture of concentrated H_2SO_4 (40 mL, 98%) and $NaNO_3$ (0.375 g) under vigorous stirring for 1h, in an ice bath. $KMnO_4$ (3.0 g) was slowly added into the reaction mixture over 1 h. The mixture was then stirred at room temperature for 4h. Afterwards, the reaction mixture was allowed to reach room temperature before being heated to 35 ^oC for 30 min, forming a thick paste. It was then poured into a beaker containing 50 mL of deionized water and further heated to 90 ^oC for 30 min. 200 mL of distilled water was added, followed by a slow addition of H_2O_2 (3 mL, 30%), turning the color of the solution from dark brown to yellow. The reaction mixture was then allowed to settle down and decanted. The graphite oxide obtained was then purified by repeated high-speed centrifugation (4200 rpm, 3 min) and redispersing in deionized water to neutralize the pH (~10 times needed). Finally, the resulting GO was dried at 60 °C in a vacuum oven for 48h.

Preparation of the GO dispersions: GO was exfoliated to give a brown dispersion of GO under ultrasonication[39,126,127,]. The resulting GO was negatively charged over a wide pH condition, as the GO sheet had chemical functional groups of carboxylic acids.

Experimental setup: Figure 7.1 presents a schematic of the experimental setup used. Before each irradiation stage precursor molecules were dissolved into the pristine GO dispersions. The resulting solution was subsequently placed into a quartz cell and then it was subjected to irradiation by a KrF excimer laser source emitting 20 ns pulses of 248 nm

at 1 Hz repetition rate. For uniform exposure of the whole irradiated volume, a top-hat beam profile was obtained using a beam homogenizer. Different combinations of laser powers (P) and the number of pulses (Np) were tested in an effort to optimize the photochemical functionalization processes. In a typical experiment, the sample was irradiated at a constant P with Np =1, 10, 100, 500 and 1000, corresponding to different photochemical reaction times.

Photoacylation of GO (GO-Cl): The acylation process took part into the quartz tube, exposed to laser beam, while the dispersion was under magnetic stirring. Specifically, GO sheets (6 mg), were dispersed in $SOCl_2$ (4 mL), through ultrasonication for 10 min and adding a small catalytic amount of N,N-dimethylformamide (DMF 0.2 mL). After 30 min of irradiation the dispersion was isolated by centrifugation and the black precipitate was washed with THF, in order to take off the excess of $SOCl_2$. The yielded GO-COCl was dried for 3h at 80 ^{o}C.

Photochemical synthesis of LGO-EDNB: The final step of the reaction, took also part into the quartz tube. In particular, GO-COCl was dispersed in THF (~2 mL) via ultrasonication for 10 min. Then, EDNB (6 mg) is added, as well as a few drops of triethylamine (Et_3N) (0.3 mL). After the addition of Et_3N the dispersion gets a pink hue. Following irradiation by pulsed laser for 30 min the dispersion darkens. The final LGO-EDNB is yielded by centrifugation (5 min at 4200 rpm), washed with MeOH and dried in a vacuum oven at 40 ^{o}C for 6 h. The total time for the photochemical synthesis of LGO-EDNB is ~2 h, while for that obtained via chemical synthesis is 4 days[28].

Characterization of GO derivatives: Fourier transform infrared (FT-IR) spectra were recorded on a BRUKER FTIR spectrometer IFS 66v/F (MIR). Raman spectroscopy was performed using a Nicolet Almega XR Raman spectrometer (Thermo Scientific) with a 473 nm blue laser as an excitation source. X-ray photoelectron spectroscopy (XPS) measurements were carried out in a Specs LHS-10 UltrahighVacuum (UHV) system. The

XPS spectra were recorded at room temperature using unmonochromatized Al Ka radiation under conditions optimized for the maximum signal (constant DE mode with a pass energy of 36 eV giving a full width at half maximum (FWHM) of 0.9 eV for the Au $4f_{7/2}$ peak). The analyzed area was an ellipsoid with dimensions 2.5 x 4.5 mm^2. The XPS core level spectra were analyzed using a fitting routine, which allows the decomposition of each spectrum into individual mixed Gaussian–Lorentzian components after a Shirley background subtraction. The attachment of EDNB moieties to GO was also confirmed by ^1H NMR spectroscopy. Figure 7.13 presents the ^1H NMR spectrum of LGO-EDNB displayed upfield signals at 9.06 and 8.92 ppm assigned to the aromatic protons ortho and meta to nitro groups, labeled ‘‘c’’ and ‘‘b’’, respectively. The aliphatic protons ‘‘a’’ gave signals at 4.00 ppm, associated with the alkyl -CH_2-CH_2- linking groups.NMR spectrum was carried out using a Bruker AMX-500 spectrometer. Electrochemical experiments were carried out by using a model PGSTAT302N (Autolab).

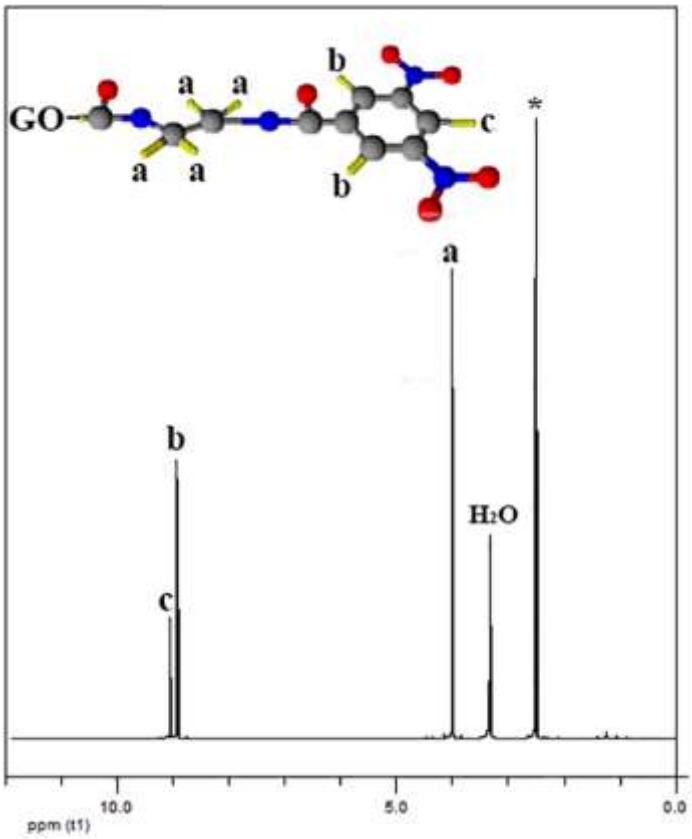

Figure 7.13: The ^{1}H NMR spectra in DMSO-d_6 solution of GO-EDNB. The solvent peak is denoted by an asterisk.

The experiments were performed with a conventional three electrode electrochemical cell. The three electrode system consisted of Ag/AgCl (SCE) as the reference electrode, Pt-disc as the working electrode and Pt-wire as the counter electrode. The chemical reagents used for those experiments were, Ferrocene (Aldrich, 98%), Tetra-butyl-ammonium hexa-fluoro-phosphate >99.0% (TBAPF6, Fluka, electrochemical analysis >99%) and acetonitrile (Acros Organics, extra dried and distilled >99.9%). The HOMO and LUMO levels were measured by the voltammographs from the onset potential of the reduction and oxidation process[108]. Therefore, we have endorsed the formula:

$$E_{HOMO} = -(E_{[onset,\ ox\ vs.\ Fc^{+}/Fc]}) + 5.1)\ (eV)$$

$$E_{LUMO} = -(E_{[onset,\ red\ vs.\ Fc^{+}/Fc]}) + 5.1)\ (eV)$$

A series of purification steps were subsequently performed, each of which comprised ultrasonication (10 min) and centrifugation (5 min at 4200 rpm) to yield the final LGO-EDNB solution used for the fabrication of OSCs. The purification process is important since it affects and determines the size and thickness range of the functionalized sheets (Figures 7.14a and 7.14b), which may be critical for the photovoltaic performance.

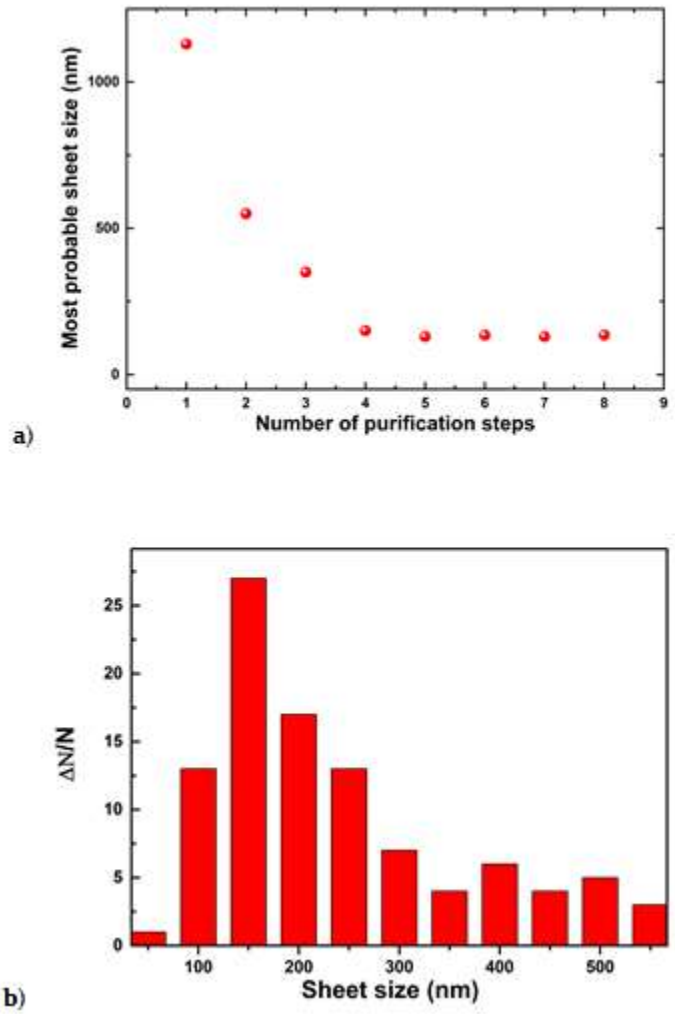

Figure 7.14: (a) Dependence of the most probable sheet size on the number of purification steps; (b) LGO-EDNB sheet size distribution following a series of five purification steps. Sheet sizes were determined using a number of TEM images.

For this purpose, following each step, the size evolution of the resulting LGO-EDNB flakes had been monitored using Transmission Electron (TEM) Microscopy. Figure 7.14a shows that the average sheet sizes were reduced upon increasing the number of purification steps. The photovoltaic performance results presented in the following correspond to the use of the LGO-EDNB solution obtained after 5 purification steps (Figure 7.14b). Further experiments are in progress to identify the optimum size that gives the best photovoltaic performance. After the purification process, the LGO-EDNB washed with MeOH and drying in a vacuum oven at 40 ^{o}C for 6h.

Preparation of Titanium suboxide (TiO_x) solution[128]: TiO_x solution preparation: Titanium(IV) isopropoxide ($Ti[OCH(CH_3)_2]_4$, 5 mL), 2-methoxyethanol ($CH_3OCH_2CH_2OH$, 20 mL) and ethanolamine ($H_2NCH_2CH_2OH$, 2 mL) were added to a three-necked flask in a nitrogen atmosphere. The solution was then stirred for 1 h at room temperature, followed by heating at 80 ^{o}C for 1 h and 120 ^{o}C for another 1 h. The solution was then cooled to room temperature and 10 mL of isopropanol (IPA) was added.

Device fabrication and measurements: PCDTBT polymer was purchased from Solaris Chem. Electron donor PCDTBT was dissolved in 1,2-dichlorobenzene:chlorobenzene (3:1) (o-DCB:CB) and stirred overnight at 80 ^{o}C to ensure the good dissolution of the polymer. Then, graphene based electron acceptor LGO-EDNB, after vacuum dried overnight, was mixed with PCDTBT with different blend ratios (respect to the polymer) and stirred for at least 2 h at 80 ^{o}C before used. The photovoltaic devices reported were fabricated on 20 mm by 15 mm indium–tin-oxide (ITO) glass substrates with a sheet resistance of ~10 Ω sq^{-1}. Patterned ITO-coated glass substrates were cleaned through a 3-step ultrasonication process (deionized water with 10% soap, acetone, IPA). As a hole transport layer, poly(ethylene- dioxythiophene) highly doped with poly(4-styrenesulfonate) (PEDOT:PSS), purchased from Heraeus, was spin-cast from an aqueous solution on the ITO substrate at 6000 rpm for 60 s with an average thickness of 30 nm and then annealed at 120 °C for 15 min. Photoactive layers with different blend ratios were subsequently deposited in ambient conditions by spin-coating PCDTBT:LGO-EDNB solution at 1000 rpm on top of PEDOT:PSS

layer until the thickness reaches approximately 80 nm, followed by drying at 60 ^{o}C for about 5 min under inert condition, to avoid the intermixing with the next deposited layer. Then, the electron extraction layers were coated by spin casting the solutions on top of the active layer. TiO_x interlayer was dissolved in methanol (1:200) and then spin-coated to a thickness of approximately 10 nm (6000 rpm, 40 s) in air[83]. The samples were heated at 80 ^{o}C for 1 min in air. Lastly, 100 nm of Al was deposited through a shadow mask by thermal evaporation on the devices. The area of each device was 4 mm^2, as determined by the overlap of the ITO and the evaporated Al. The performances of the devices were measured at room temperature with an Air Mass 1.5 Global (A.M. 1.5 G) solar simulator at an intensity of 100 mW cm^{-2} (1 sun irradiation). A reference monocrystalline silicon solar cell from Newport Corp. was used to calibrate the light intensity. All measurements were carried out in air immediately after device fabrication without encapsulation process.

7.4. Conclusion

In brief, we have demonstrated the successful synthesis of a novel graphene-based electron acceptor, through laser-induced covalent grafting of GO nanosheets with EDNB molecules. The LGO-EDNB derivative attained exhibited improved processability, physicochemical and electronic properties compared to the pristine GO nanosheets. More importantly, it is shown that our technique enables bandgap tunability of the LGO-EDNB acceptor, and thus its HOMO-LUMO levels can be tailored to perfect match the energy levels of the state-of-the art polymer donor used in OSCs. A property that paves the way for its application as efficient electron acceptor in OSCs, opening new avenues for the realization of all graphene based OSCs. The photochemical synthesis presented here is a universal, facile, catalyst-free, and can be performed at room temperature and can provide adequate control over the functional unit levels, which is not readily realized by existing methods. The combination of different irradiation parameters and precursor materials with various attaching molecules could yield a virtually unlimited number of graphene nanoconjugates, in terms of composition, electronic structure and electrochemical properties, making this method very

appropriate for the production of extraordinary types of nanomaterials that cannot be attained via traditional chemical routes. These conjugates can be obtained directly in solution, without the use of supplementary chemical reagents and thus they can be used for applications without further purification.

List of publications

1. Sygletou M., Tzourmpakis P., Petridis C., Konios D., Fotakis C., Kymakis E., Stratakis E., · "Laser induced assembly of plasmonic nanoparticles on two-dimensional nanosheets for organic photovoltaics", Journal of Materials Chemistry A, 4(3), 1020-1027, 2016

2. Sygletou M., Kakavelakis G., Paci B., Generosi A., Kymakis E., Stratakis E., "Enhanced Stability of Aluminum Nanoparticle-Doped Organic Solar Cells", ACS Applied Materials & Interfaces 7(32), 17756-17764, 2015

3. Minas M. Stylianakis, Maria Sygletou, Kyriaki Savva, George Kakavelakis, Emmanuel Kymakis* and Emmanuel Stratakis "Photochemical Synthesis of Solution-Processable Graphene Derivatives with Tunable Bandgaps for Organic Solar Cells", Advanced Optical Materials, 3(5), 2014

4. Petridis C., Konios D, Stylianakis M.M., Kakavelakis G., Sygletou M., Savva K., Tzourmpakis P., Krassas M., Vaenas N., Stratakis E. and Kymakis E., "Solution-Processed Reduced Graphene Oxide Electrodes for Organic Photovoltaics", accepted in Nanoscale Horiz, 2016

5. Konios D., Petridis C., Kakavelakis G., Sygletou M., Savva K., Kymakis M., Stratakis M., "Reduced Graphene Oxide Micromesh Electrodes for large area, flexible photovoltaic devices", Advanced Functional Materials, 2015

6. Pichaya Pattanasattayavong, Maria Sygletou, Emmanuel Kymakis, Emmanuel Stratakis, Feng Yan, Vasilis G. Gregoriou, Thomas D. Anthopoulos and Christos L. Chochos, “The role of the ethynylene bond on the optical and electronic properties of diketopyrrolopyrrole copolymers”, RSC Advances, 4, 58404, 2014

7. I.A. Sukhova, G.A. Shafeeva, V.V. Voronova, M. Sygletou, E. Stratakis, C. Fotakis “Generation of nanoparticles of bronze and brass by laser ablation in liquid”, Applied Surface Science, 302, 79-82, 2013

References

1 Q. Gan, F. J. Bartoli and Z. H. Kafafi, *Adv. Mater.*, 2013, **25**, 2385–2396.

2 E. Stratakis and E. Kymakis, *Mater. Today*, 2013, **16**, 133–146.

3 C. C. D. Wang, W. C. H. Choy, C. Duan, D. D. S. Fung, W. E. I. Sha, F.-X. Xie, F. Huang and Y. Cao, *J. Mater. Chem.*, 2012, **22**, 1206–1211.

4 L. Y. Lu, Z. Q. Luo, T. Xu and L. P. Yu, *Nano Lett.*, 2013, **13**, 59–64.

5 G. D. Spyropoulos, M. M. Stylianakis, E. Stratakis and E. Kymakis, *Appl. Phys. Lett.*, 2012, **100**, 213904.

6 X. Li, W. C. H. Choy, H. Lu, W. E. I. Sha and A. H. P. Ho, *Adv. Funct. Mater.*, 2013, **23**, 2728–2735.

7 S.-W. Baek, J. Noh, C.-H. Lee, B. Kim, M.-K. Seo and J.-Y. Lee, *Sci. Rep.*, 2013, **3**, 1726.

8 W. E. I. Sha, W. C. H. Choy, Y. G. Liu and W. Cho Chew, *Appl. Phys. Lett.*, 2011, **99**, 1–4.

9 X. Li, W. C. H. Choy, L. Huo, F. Xie, W. E. I. Sha, B. Ding, X. Guo, Y. Li, J. Hou, J. You and Y. Yang, *Adv. Mater.*, 2012, **24**, 3046–3052.

10 W. P. Liao, Y. H. Su, Y. K. Huang, C. S. Yeh, L. W. Huang and J. J. Wu, *ACS Appl. Mater. Interfaces*, 2014, **6**, 17993–18000.

11 W. C. H. Choy, *Chem. Commun.*, 2014, **50**, 11984–11993.

12 B. Paci, G. D. Spyropoulos, A. Generosi, D. Bailo, V. R. Albertini, E. Stratakis and E. Kymakis, *Adv. Funct. Mater.*, 2011, **21**, 3573–3582.

13 L. Huo, T. Liu, X. Sun, Y. Cai, A. J. Heeger and Y. Sun, *Adv. Mater.*, 2015, 1–7.

14 C.-C. Chen, W.-H. Chang, K. Yoshimura, K. Ohya, J. You, J. Gao, Z. Hong and Y. Yang, *Adv.*

Mater., 2014, **26**, 5670–5677.

15 M. O. Reese, A. M. Nardes, B. L. Rupert, R. E. Larsen, D. C. Olson, M. T. Lloyd, S. E. Shaheen, D. S. Ginley, G. Rumbles and N. Kopidakis, *Adv. Funct. Mater.*, 2010, **20**, 3476–3483.

16 M. O. Reese, A. J. Morfa, M. S. White, N. Kopidakis, S. E. Shaheen, G. Rumbles and D. S. Ginley, 2008, **92**, 746–752.

17 B. M. O. Reese, A. M. Nardes, B. L. Rupert, R. E. Larsen, D. C. Olson, M. T. Lloyd, S. E. Shaheen, D. S. Ginley, G. Rumbles and N. Kopidakis, 2010, 3476–3483.

18 B. Paci, A. Generosi, R. Albertini and G. D. Spyropoulos, 2012, 7452–7459.

19 B. Paci, D. Bailo, V. R. Albertini, J. Wright, C. Ferrero and G. D. Spyropoulos, 2013, 1–6.

20 G. Kakavelakis, D. Konios, E. Stratakis and E. Kymakis, *Chem. Mater.*, 2014, 141007170410009.

21 M. Krassas, G. Kakavelakis, M. M. Stylianakis, N. Vaenas, E. Stratakis and E. Kymakis, *RSC Adv.*, 2015, **5**, 71704–71708.

22 Y. Kubota, K. Watanabe, O. Tsuda and T. Taniguchi, *Science (80-.).*, 2007, **317**, 932–934.

23 C. R. Dean, a F. Young, I. Meric, C. Lee, L. Wang, S. Sorgenfrei, K. Watanabe, T. Taniguchi, P. Kim, K. L. Shepard and J. Hone, *Nat. Nanotechnol.*, 2010, **5**, 722–726.

24 Q. H. Wang, K. Kalantar-Zadeh, A. Kis, J. N. Coleman and M. S. Strano, *Nat. Nanotechnol.*, 2012, **7**, 699–712.

25 A. Splendiani, L. Sun, Y. Zhang, T. Li, J. Kim, C. Y. Chim, G. Galli and F. Wang, *Nano Lett.*, 2010, **10**, 1271–1275.

26 F. Bonaccorso, N. Balis, M. M. Stylianakis, M. Savarese, C. Adamo, M. Gemmi, V.

Pellegrini, E. Stratakis and E. Kymakis, *Adv. Funct. Mater.*, 2015, **25**, 3870–3880.

27 J. H. Seol, I. Jo, A. L. Moore, L. Lindsay, Z. H. Aitken, M. T. Pettes, X. Li, Z. Yao, R. Huang, D. Broido, N. Mingo, R. S. Ruoff and L. Shi, *Science (80-.).*, 2010, **328**, 213–216.

28 S. Stankovich, D. A. Dikin, G. H. B. Dommett, K. M. Kohlhaas, E. J. Zimney, E. A. Stach, R. D. Piner, S. T. Nguyen and R. S. Ruoff, *Nature*, 2006, **442**, 282–286.

29 M. M. Stylianakis, J. A. Mikroyannidis and E. Kymakis, *Sol. Energy Mater. Sol. Cells*, 2010, **94**, 267–274.

30 E. Kymakis and G. A. J. Amaratunga, *Appl. Phys. Lett.*, 2002, **80**, 112–114.

31 K. S. Subrahmanyam, P. Kumar, A. Nag and C. N. R. Rao, *Solid State Commun.*, 2010, **150**, 1774–1777.

32 P. KUMAR, K. S. SUBRAHMANYAM and C. N. R. RAO, *Int. J. Nanosci.*, 2011, **10**, 559–566.

33 E. Kymakis, K. Savva, M. M. Stylianakis, C. Fotakis and E. Stratakis, *Adv. Funct. Mater.*, 2013, **23**, 2742–2749.

34 U. Maitra, H. Matte, P. Kumar and C. N. R. Rao, *Chimia (Aarau).*, 2012, **66**, 941–948.

35 Y. L. Zhang, L. Guo, H. Xia, Q. D. Chen, J. Feng and H. B. Sun, *Adv. Opt. Mater.*, 2014, **2**, 10–28.

36 K. Savva, Y. H. Lin, C. Petridis, E. Kymakis, T. D. Anthopoulos and E. Stratakis, *J. Mater. Chem. C*, 2014, **2**, 5931–5937.

37 P. Kumar, B. Das, B. Chitara, K. S. Subrahmanyam, K. Gopalakrishnan, S. B. Krupanidhi and C. N. R. Rao, *Macromol. Chem. Phys.*, 2012, **213**, 1146–1163.

38 P. Kumar, K. S. Subrahmanyam and C. N. R. Rao, *Mater. Express*, 2011, **1**, 252–256.

39 Y. Zhang, L. Guo, S. Wei, Y. He, H. Xia, Q. Chen, H. B. Sun and F. S. Xiao, *Nano Today*,

2010, **5**, 15–20.

40 C. Petridis, Y. H. Lin, K. Savva, G. Eda, E. Kymakis, T. D. Anthopoulos and E. Stratakis, *Appl. Phys. Lett.*, 2013, **102**.

41 C. W. Tang, *Appl. Phys. Lett.*, 1986, **48**, 183–185.

42 G. Yu, J. Gao, J. C. Hummelen, F. Wudl and A. J. Heeger, *Science (80-.).*, 1995, **270**, 1789–1791.

43 E. M. Conwell and H. A. Mizes, *Phys. Rev. B*, 1995, **51**, 6953–6958.

44 R. N. Marks, J. J. M. Halls, D. D. C. Bradley, R. H. Friend and a B. Holmes, *J. Phys. Condens. Matter*, 1994, **6**, 1379.

45 T. Ameri, P. Khoram, J. Min and C. J. Brabec, *Adv. Mater.*, 2013, **25**, 4245–4266.

46 L. Lu, M. A. Kelly, W. You and L. Yu, *Nat. Photonics*, 2015, **9**, 491–500.

47 V. Shrotriya, E. H. E. Wu, G. Li, Y. Yao and Y. Yang, *Appl. Phys. Lett.*, 2006, **88**.

48 E. T. Yu and J. van de Lagemaat, *MRS Bull.*, 2011, **36**, 424–428.

49 H. A. Atwater and A. Polman, *Nat. Mater.*, 2010, **9**, 865–865.

50 S. Pillai and M. A. Green, *Sol. Energy Mater. Sol. Cells*, 2010, **94**, 1481–1486.

51 K. L. Kelly, E. Coronado, L. L. Zhao and G. C. Schatz, *J. Phys. Chem. B*, 2003, **107**, 668.

52 B. Paci, A. Generosi, D. Bailo, V. R. Albertini and R. De Bettignies, *Chem. Phys. Lett.*, 2010, **494**, 69–74.

53 A. Sperlich, H. Kraus, C. Deibel, H. Blok, J. Schmidt and V. Dyakonov, 2011, 13513–13518.

54 F. Deschler, A. De Sio, E. Von Hauff, P. Kutka, T. Sauermann, H. J. Egelhaaf, J. Hauch and E. Da Como, *Adv. Funct. Mater.*, 2012, **22**, 1461–1469.

55 M. J??rgensen, K. Norrman and F. C. Krebs, *Sol. Energy Mater. Sol. Cells*, 2008, **92**,

686–714.

56 J. H. Park, Y. T. Lim, O. O. Park and Y. C. Kim, 2003, 331–334.

57 Y. Feng, J. Cheng, L. Zhou, X. Zhou and H. Xiang, *Analyst*, 2012, **137**, 4885–4901.

58 J. R. Lakowicz, *Principles of Fluorescence Spectroscopy Principles of Fluorescence Spectroscopy*, 2006.

59 M. M. Stylianakis, G. D. Spyropoulos, E. Stratakis and E. Kymakis, *Carbon N. Y.*, 2012, **50**, 5554–5561.

60 I. Song, C. Park and H. C. Choi, *RSC Adv.*, 2015, **5**, 7495–7514.

61 H. Terrones, F. López-Urías and M. Terrones, *Sci. Rep.*, 2013, **3**, 1549.

62 Y. T. Lim, T.-W. Lee, H.-C. Lee and O. O. Park, *Synth. Met.*, 2002, **128**, 133–137.

63 J. H. Park, Y. T. Lim, O. O. Park, J. K. Kim, J. Yu and Y. C. Kim, 2004, 688–692.

64 E. Stratakis, M. Barberoglou, C. Fotakis, G. Viau, C. Garcia and G. a Shafeev, *Opt. Express*, 2009, **17**, 12650–12659.

65 I. A. Sukhov, G. A. Shafeev, V. V. Voronov, M. Sygletou, E. Stratakis and C. Fotakis, in *Applied Surface Science*, Elsevier, 2014, vol. 302, pp. 79–82.

66 E. Stratakis and G. a Shafeev, *Laser Ablation Liq. Princ. Appl. Prep. Nanomater.*, 2012, 815–853.

67 M. Dell'Aglio, R. Gaudiuso, O. De Pascale and A. De Giacomo, *Appl. Surf. Sci.*, 2015, **348**, 4–9.

68 A. D. Pomogailo and G. I. Dzhardimalieva, *Nanostructured materials preparation via condensation ways*, 2014.

69 H. Choi, S.-J. Ko, Y. Choi, P. Joo, T. Kim, B. R. Lee, J.-W. Jung, H. J. Choi, M. Cha, J.-R. Jeong, I.-W. Hwang, M. H. Song, B.-S. Kim and J. Y. Kim, *Nat. Photonics*, 2013, **7**, 732–

738.

70 G. Goncalves, P. A. A. P. Marques, C. M. Granadeiro, H. I. S. Nogueira, M. K. Singh and J. Grácio, *Chem. Mater.*, 2009, **21**, 4796–4802.

71 A. Y. Polyakov, L. Yadgarov, R. Popovitz-Biro, V. a V. a. Lebedev, I. Pinkas, R. Rosentsveig, Y. Feldman, A. E. Goldt, E. A. Goodilin and R. Tenne, *J. Phys. Chem. C*, 2014, 140106140624005.

72 J. Beheshtian, H. Soleymanabadi, A. A. Peyghan and Z. Bagheri, *Appl. Surf. Sci.*, 2013, **268**, 436–441.

73 X. Z. Zhou, X. Huang, X. Y. Qi, S. X. Wu, C. Xue, F. Y. C. Boey, Q. Y. Yan, P. Chen and H. Zhang, *J Phys Chem C*, 2009, **113**, 10842–10846.

74 X. Wang, L. Zhi and K. Müllen, *Nano Lett.*, 2008, **8**, 323–327.

75 H. C. Schniepp, J. L. Li, M. J. McAllister, H. Sai, M. Herrera-Alonson, D. H. Adamson, R. K. Prud'homme, R. Car, D. A. Seville and I. A. Aksay, *J. Phys. Chem. B*, 2006, **110**, 8535–8539.

76 V. C. Tung, M. J. Allen, Y. Yang and R. B. Kaner, *Nat. Nanotechnol.*, 2009, **4**, 25–29.

77 J. R. Lomeda, C. D. Doyle, D. V. Kosynkin, W. F. Hwang and J. M. Tour, *J. Am. Chem. Soc.*, 2008, **130**, 16201–16206.

78 S. Gilje, S. Han, M. Wang, K. L. Wang and R. B. Kaner, *Nano Lett.*, 2007, **7**, 3394–3398.

79 D. A. Dikin, S. Stankovich, E. J. Zimney, R. D. Piner, G. H. B. Dommett, G. Evmenenko, S. T. Nguyen and R. S. Ruoff, *Nature*, 2007, **448**, 457–460.

80 L. Guo, Y. L. Zhang, D. D. Han, H. B. Jiang, D. Wang, X. Bin Li, H. Xia, J. Feng, Q. D. Chen and H. B. Sun, *Adv. Opt. Mater.*, 2014, **2**, 120–125.

81 G. Kakavelakis, E. Stratakis and E. Kymakis, *RSC Adv.*, 2013, **3**, 16288.

82 G. Kakavelakis, E. Stratakis and E. Kymakis, *Chem. Commun. (Camb).*, 2014, **50**, 5285–7.

83 D. H. Wang, S. H. Im, H. K. Lee, O. O. Park and J. H. Park, *J. Phys. Chem. C*, 2009, **113**, 17268–17273.

84 B. Paci, A. Generosi, V. R. Albertini, P. Perfetti and R. De Bettignies, 2009, 19740–19747.

85 N. Grossiord, J. M. Kroon, R. Andriessen and P. W. M. Blom, *Org. Electron.*, 2012, **13**, 432–456.

86 A. Roldán, J. M. Ricart and F. Illas, *Theor. Chem. Acc.*, 2011, **128**, 675–681.

87 M. D. Malinsky, K. L. Kelly, G. C. Schatz and R. P. Van Duyne, *J. Am. Chem. Soc.*, 2001, 1471–1482.

88 F. Etzold, I. a. Howard, R. Mauer, M. Meister, T. D. Kim, K. S. Lee, N. S. Baek and F. Laquai, *J. Am. Chem. Soc.*, 2011, **133**, 9469–9479.

89 J. Ouyang, Q. Xu, C. W. Chu, Y. Yang, G. Li and J. Shinar, *Polymer (Guildf).*, 2004, **45**, 8443–8450.

90 M. Manceau, S. Chambon, A. Rivaton, J. L. Gardette, S. Guillerez and N. Lematre, *Sol. Energy Mater. Sol. Cells*, 2010, **94**, 1572–1577.

91 K.-J. Baeg, M. Binda, D. Natali, M. Caironi and Y.-Y. Noh, *Adv. Mater.*, 2013, **25**, 4267–95.

92 Y. Li, W. Song, C. Xie, D. Zeng, A. Wang and M. Hu, *Mater. Chem. Phys.*, 2006, **97**, 127–131.

93 T. Nishimura and V. Raman, 2014, 4710–4722.

94 A. Shahravan, T. Desai and T. Matsoukas, 2014, 2–7.

95 J. J. Mock, M. Barbic, D. R. Smith, D. A. Schultz and S. Schultz, *J. Chem. Phys.*, 2002, **116**, 6755–6759.

96 S. K. Mandal, R. K. Roy and A. K. Pal, *J. Phys. D-Appl. Phys.*, 2003, **36**, 261–265.

97 S. Reich, a. Ferrari, R. Arenal, a. Loiseau, I. Bello and J. Robertson, *Phys. Rev. B*, 2005, **71**, 1–12.

98 G. Kakavelakis, D. Konios, E. Stratakis and E. Kymakis, *Chem. Mater.*, 2014, **26**, 5988–5993.

99 M. M. Stylianakis, E. Stratakis, E. Koudoumas, E. Kymakis and S. H. Anastasiadis, *ACS Appl. Mater. Interfaces*, 2012, **4**, 4864–4870.

100 E. Stratakis, K. Savva, D. Konios, C. Petridis and E. Kymakis, *Nanoscale*, 2014, **6**, 6925–31.

101 M. M. Stylianakis, M. Sygletou, K. Savva, G. Kakavelakis, E. Kymakis and E. Stratakis, *Adv. Opt. Mater.*, 2015, **3**, 658–666.

102 D. Konios, C. Petridis, G. Kakavelakis, M. Sygletou, K. Savva, E. Stratakis and E. Kymakis, *Adv. Funct. Mater.*, 2015, **25**, 2213–2221.

103 Z. Liu, S. P. Lau and F. Yan, *Chem. Soc. Rev.*, 2015, **44**, 5638–79.

104 M. Shanmugam, T. Bansal, C. A. Durcan and B. Yu, *Appl. Phys. Lett.*, 2012, **100**, 1–5.

105 N. Balis, D. Konios, E. Stratakis and E. Kymakis, *ChemNanoMat*, 2015, **1**, 346–352.

106 Y. C. Chen, C. Y. Hsu, R. Y. Y. Lin, K. C. Ho and J. T. Lin, *ChemSusChem*, 2013, **6**, 20–35.

107 J. Kang, S. Tongay, J. Li and J. Wu, *J. Appl. Phys.*, 2013, **113**.

108 C. M. Cardona, W. Li, A. E. Kaifer, D. Stockdale and G. C. Bazan, *Adv. Mater.*, 2011, **23**, 2367–2371.

109 J. K. Wassei, K. C. Cha, V. C. Tung, Y. Yang and R. B. Kaner, *J. Mater. Chem.*, 2011, **21**,

3391.

110 A. Kasry, A. A. Ardakani, G. S. Tulevski, B. Menges, M. Copel and L. Vyklicky, *J. Phys. Chem. C*, 2012, **116**, 2858–2862.

111 V. Abdelsayed, S. Moussa, H. M. Hassan, H. S. Aluri, M. M. Collinson and M. S. El-Shall, *J. Phys. Chem. Lett.*, 2010, **1**, 2804–2809.

112 S. Stankovich, D. A. Dikin, R. D. Piner, K. A. Kohlhaas, A. Kleinhammes, Y. Jia, Y. Wu, S. T. Nguyen and R. S. Ruoff, *Carbon N. Y.*, 2007, **45**, 1558–1565.

113 R. Y. N. Gengler, D. S. Badali, D. Zhang, K. Dimos, K. Spyrou, D. Gournis and R. J. D. Miller, *Nat. Commun.*, 2013, **4**, 2560.

114 N. A. Kumar, H. Nolan, N. McEvoy, E. Rezvani, R. L. Doyle, M. E. G. Lyons and G. S. Duesberg, *J. Mater. Chem. A*, 2013, **1**, 4431.

115

116 A. K. Chakraborty, K. S. Coleman and V. R. Dhanak, *Nanotechnology*, 2009, **20**, 155704.

117 † Mikhail E Itkis Elena Bekyarova † Palanisamy Ramesh,† Claire Berger,‡ Michael Sprinkle,‡ and ‡ and Robert C Haddon* Walt A. de Heer †, *Jacs*, 2009, 1336–1337.

118 Y. Xu, B. Hua and G. Lu, *J. Am. Chem. Soc.*, 2008, **130**, 5856–5857.

119 L. Guo, R. Q. Shao, Y. L. Zhang, H. B. Jiang, X. Bin Li, S. Y. Xie, B. Bin Xu, Q. D. Chen, J. F. Song and H. B. Sun, *J. Phys. Chem. C*, 2012, **116**, 3594–3599.

120 V. Bavastrello, S. Carrara, M. K. Ram and C. Nicolini, *Langmuir*, 2004, **20**, 969–973.

121 Z. Luo, N. J. Pinto, Y. Davila and A. T. Charlie Johnson, *Appl. Phys. Lett.*, 2012, **100**.

122 M. C. Scharber, D. Mühlbacher, M. Koppe, P. Denk, C. Waldauf, A. J. Heeger and C. J. Brabec, *Adv. Mater.*, 2006, **18**, 789–794.

123 Z. Yin, S. Sun, T. Salim, S. Wu, X. Huang, Q. He, Y. M. Lam and H. Zhang, 2010, **4**, 5263–5268.

124 Z. Yin, S. Wu, X. Zhou, X. Huang, Q. Zhang, F. Boey and H. Zhang, *Small*, 2010, **6**, 307–312.

125 Q. Su, S. Pang, V. Alijani, C. Li, X. Feng and K. Müllen, *Adv. Mater.*, 2009, **21**, 3191–3195.

126 A. Ciesielski and P. Samorì, *Chem. Soc. Rev.*, 2014, **43**, 381–398.

127 Z. Y. Xia, S. Pezzini, E. Treossi, G. Giambastiani, F. Corticelli, V. Morandi, A. Zanelli, V. Bellani and V. Palermo, *Adv. Funct. Mater.*, 2013, **23**, 4684–4693.

128 Z. He, C. Zhong, S. Su, M. Xu, H. Wu and Y. Cao, *Nat Phot.*, 2012, **6**, 591–595.